CENTRO INTERNACIONAL DE ESTUDOS
DE DOUTORAMENTO E AVANZADOS
DA USC (CIEDUS)

TESIS DE DOCTORADO

Effect of oxygen vacancies on the structural and transport properties of $SrTiO_3$ thin films: experiments and ab-initio calculations

Lucía Iglesias Bernardo

ESCUELA DE DOCTORADO INTERNACIONAL

PROGRAMA DE DOCTORADO EN CIENCIA DE MATERIALES

SANTIAGO DE COMPOSTELA

2019

USC
UNIVERSIDADE
DE SANTIAGO
DE COMPOSTELA

DECLARACIÓN DEL AUTOR DE LA TESIS

Effect of oxygen vacancies on the structural and transport properties of $SrTiO_3$ thin films: experiments and ab-initio calculations

Dña. Lucía Iglesias Bernardo

Presento mi tesis, siguiendo el procedimiento adecuado al Reglamento, y declaro que:

1) *La tesis abarca los resultados de la elaboración de mi trabajo.*
2) *En su caso, en la tesis se hace referencia a las colaboraciones que tuvo este trabajo.*
3) *La tesis es la versión definitiva presentada para su defensa y coincide con la versión enviada en formato electrónico.*
4) *Confirmo que la tesis no incurre en ningún tipo de plagio de otros autores ni de trabajos presentados por mí para la obtención de otros títulos.*

En Santiago de Compostela, 10 de julio de 2019

Fdo

USC
UNIVERSIDADE
DE SANTIAGO
DE COMPOSTELA

AUTORIZACIÓN DEL DIRECTOR / TUTOR DE LA TESIS

Effect of oxygen vacancies on the structural and transport properties of $SrTiO_3$ thin films: experiments and ab-initio calculations

D. José Francisco Rivadulla Fernández
D. Víctor Pardo Castro

INFORMA/N:

Que la presente tesis, corresponde con el trabajo realizado por Dña. Lucía Iglesias, bajo mi dirección, y autorizo su presentación, considerando que reúne los requisitos exigidos en el Reglamento de Estudios de Doctorado de la USC, y que como director de ésta no incurre en las causas de abstención establecidas en Ley 40/2015.

En Santiago de Compostela, 10 de julio de 2019

Fdo: José Francisco Rivadulla Fernández

Fdo: Víctor Pardo Castro

USC
UNIVERSIDADE
DE SANTIAGO
DE COMPOSTELA

Acknowledgements

Una parte del viaje es el final y esta tesis significa el final de un viaje que emprendí hace poco más de 4 años. Desde luego el viaje no ha sido fácil, plagado de retos, ilusiones y aspiraciones, y por qué no decirlo, de algunos fracasos, desilusiones y mucho trabajo duro. Ha sido un viaje en el que he reído y llorado, pero sobre todo en el que he aprendido y madurado. En estas pocas líneas pretendo expresar mi agradecimiento a todas las personas que de una forma u otra me han ayudado a finalizar este viaje.

Indudablemente el primero de la lista es uno de mis directores de tesis, Francisco Rivadulla. No tengo palabras suficientes para expresar todo lo que agradezco su guía, entusiasmo y perserverancia, sin los cuales estoy segura de que habría sido muy difícil completar esta tesis. En él he encontrado un amigo más que un jefe, que me ha apoyado y ayudado cuando los ánimos flaqueaban. Espero haber estado a la altura y haber cumplido al menos algunas de sus expectativas. Quiero agradecer también especialmente a mi otro director de tesis, Víctor Pardo. Su guía y paciencia para enseñar a alguien marcadamente experimental a introducirse en el mundo teórico es para enmarcar.

Agradezco también enormemente el apoyo de mis compañeros de laboratorio durante estos años, empezando por Eric, quien ha sido uno de los mejores apoyos en toda esta etapa, transmitiéndome siempre su tenacidad y pasión por la ciencia. Jose, por enseñarme a decir ”pode ser” y ”depende”. Carolina, por haber escuchado mis quejas en la parte final de esta tesis y Daniela, con la que sin duda he compartido grandes momentos. Y a Víctor, que aunque con los colores tiene un gusto du-

doso, siempre se ha ofrecido para echarme una mano con todos los problemitas informáticos que he tenido. También quiero agradecer a Álex, Elías, David, Carlos, Bea y Tinh. Quiero hacer también especial mención a Irene y Araceli, con las que he tenido el placer de colaborar. Ha sido un privilegio compartir estos años con todos ellos, sin duda han sido mi segunda familia durante este tiempo y sin su apoyo habría sido un viaje mucho más difícil de completar. De aquí me llevo un puñado de amigos, que espero conservar por mucho tiempo.

I would also like to thank Silvia Picozzi, who was responsible for my stay in her group in Chieti, Italy. I have been fortunate to share three months with her, and she is undoubtedly one of those people who marks you due to her enthusiasm, patience and closeness. I also want to extend my thanks to my office mates, Hrishit and Huimin, who greatly helped me during my days in Chieti. E anche ai miei coinquilini (e amici) durante il soggiorno, Federica, Angelina e Ana, mi sono divertito molto con loro.

A mi padre, sin la humildad y la perserverancia que me inculcó desde pequeña estoy segura que no podría haber llegado hasta aquí. Allá donde estés espero que estés orgulloso de mí... A mi madre y a mi hermano, gracias por estar ahí para apoyarme siempre, sin los valores que me habeis transmitido no podría haber llegado a ser quien soy. También quería agradecer a mis amigas, Laura, Sheila y Gala, por compartir momentos y risas desde siempre, sois de lo mejor. También a Nuria que ha compartido esta aventura conmigo en Santiago, y a Fernando, él también ha compartido una parte muy importante de este viaje y ha sabido escucharme y aconsejarme siempre acertadamente.

Muchas gracias a todos, pero sobre todo al que no está... Quiero dedicarle esta tesis a mi padre.

Contents

Acknowledgements **7**

Aim of the Thesis **13**

1 Introduction **17**
1.1 $LaAlO_3/SrTiO_3$ interface 18
1.1.1 The polar catastrophe scenario 19
1.1.2 The oxygen vacancies scenario 23
1.1.3 Cation intermixing at the LAO/STO interface . 26
1.2 Strain and defect engineering of transition metal oxides 28
1.3 Structure and properties of $SrTiO_3$ 33

2 Experimental techniques **39**
2.1 Pulsed Laser Deposition 39
2.2 X-Ray Diffraction and Reflectivity 42
2.3 Atomic Force Microscopy 48
2.3.1 Electrostatic Force Microscopy and Kelvin Probe Microscopy 51
2.4 Electrical transport measurements 54
2.4.1 Electrical resistivity 55
2.4.2 Hall effect measurements 56
2.4.3 Seebeck effect measurements 58

3 Computational Modelling **61**
3.1 Density Functional Theory (DFT) 62

3.1.1 Brief history 62
3.1.2 Khon-Sham approach 64
3.2 The Exchange-Correlation Functional 67
3.2.1 Generalized Gradient Approximation (GGA) . 67
3.3 Wien2k and VASP Packages 68
3.4 Electrical polarization 70

4 Thermodynamics of oxygen vacancy formation 73
4.1 Sample growth and characterization 75
4.1.1 Preparation of the substrates 75
4.1.2 PLD deposition and structural characterization 77
4.2 Creation and annihilation of oxygen vacancies 84
4.3 Enthalpy of formation of oxygen vacancies 89
4.4 Summary 92

5 Controlled movement of oxygen vacancies 93
5.1 KPFM versus EFM 95
5.2 Mobility of vacancies under an external electric field . 96
5.3 Room temperature diffusion coefficient of oxygen vacancies 100
5.4 Summary 110

6 Octahedral rotations and ferroelectric-like response 113
6.1 Strain-dependence of octahedral rotation pattern 115
6.1.1 Origin of the distortions: ab-initio calculations 120
6.2 Ferroelectric-like response 123
6.2.1 Cooperative octahedral rotations and polarization: ab-initio calculations 125
6.2.2 Oxygen vacancy influence on the polarization: ab-initio calculations 136
6.3 Summary 141

7 Transport properties of strained $SrTiO_3$ thin films 143
7.1 Out-of-plane magnetoresistance 144
7.2 Temperature dependence of the electrical resistivity: effect of strain and defects 152

7.3 Summary 170

Concluding remarks and outlook **173**

Summary in Spanish/Resumen en Castellano **177**

List of publications **189**

List of oral presentations **191**

USC
UNIVERSIDADE
DE SANTIAGO
DE COMPOSTELA

Aim of the Thesis

Many of the most relevant technological advances of the past decades have been closely related to the progress made in the fields of Materials Science and Condensed Matter Physics. In particular, the second half of the 20th century was characterized by an explosion of new materials and new ways of adjusting their properties, i.e. functional materials design. The rapid progress of electronics during this period involved the mutual reinforcement between materials research and their practical application in areas as diverse as engineering, medicine, construction or information technology, creating a multidisciplinary scientific community.

The driving force behind many of the most impressive advances we have experienced in recent decades is the ability to control on demand the electronic properties of a material. For instance, the devices based on semiconductor interfaces (mostly composed by silicon) can be controlled by an electric field, exposure to light, pressure, or heat. Literally, billions of these devices are incorporated in consumer electronics indispensable in our daily life, such as cars, laptops, mobile phones, televisions, etc.

However, the astonishing revolution of the past century in the area of electronics has created a need for better technologies as well as the miniaturization of the devices. In this regard, oxides interfaces could become a key ingredient for new concepts of electronics devices, exhibiting a wide range of phenomena such as magnetism, superconductivity, ionic conduction or ferroelectricity.

Among the oxides family, the oxoperovskites are particularly inter-

esting because they exhibit an extraordinary number of physical properties: optical, magnetic, energy harvesting applications, etc. This diversity emanates from their high flexibility to accept cation substitution and the possibility, even more appealing, to control the occupancy of the anion (oxygen) site in these oxides. In the next few years we will probably see the development of new methods to control the occupation of the anionic sublattice (the oxide-ions in the case of oxides), which will open unforeseen possibilities to tailor and improve the functionalities of these materials.

In this regard, strontium titanate ($SrTiO_3$) is a paradigmatic example within the oxides perovskite family. In its bulk form, it is a quantum paraelectric insulator, with a wide band gap of 3.2 eV, diamagnetic and with a high dielectric constant. $SrTiO_3$ is also used as a functional material in diverse applications such as solar cells, gas sensors or resistive switching memories. Moreover, the excellent properties of $SrTiO_3$ makes it widely used as the preferred substrate in the deposition of numerous oxides, and it is a fundamental partner of $LaAlO_3$ and other oxides in the famous 2-dimensional electron gas interface. Consequently, $SrTiO_3$ is probably one of the most suitable materials for understanding the nature of effects related with oxygen vacancies or strain.

The **main aim** of this Thesis is to study the effect of oxygen vacancies on the structural and transport properties of STO thin films under the influence of epitaxial strain. With the results, we also want to contribute to the discussion about the role of oxygen vacancies in the observed phenomenology of $LaAlO_3/SrTiO_3$ interface, as well as in other heterostructures involving STO as a substrate.

In addition, a novel approach will be used in this Thesis, combining experimental and theoretical studies to investigate and understand the underlying mechanisms that link oxygen vacancies and the properties of these materials.

The possibility to manipulate the oxygen vacancy concentration at will by means of an external stimulus will be addressed, determining the strain dependence of the mobility and diffusion coefficient of oxygen vacancies at room temperature. In addition, the potential use of STO on future resistive switching memories was discussed, analysing the main

control parameters in the production and stabilization of these devices.

Also the strain dependence of the octahedral rotations within the thin films will be determined, studying the influence of defects from a theoretical point of view. Moreover, a complete theoretical study about the appearance of ferroelectricity in STO thin films was addressed, examining the influence of octahedral configurations, defects and strain.

Lastly, the magneto-transport properties of the strained STO thin films will be examined with especial emphasis on the discussion about the existence of Kondo effect and the emergence of a magnetic order at low temperature due to the presence of oxygen vacancies.

USC
UNIVERSIDADE
DE SANTIAGO
DE COMPOSTELA

1. Introduction

Life need not be easy, provided only that it is not empty.

Lise Meitner, Austrian-Swedish physicist who worked on radioactivity and Nuclear Physics.

Herbert Kroemer started his Nobel lecture in 2000 claiming that, ”Often, it may be said that the interface is the device” [1]. With this precept, he was referring to the surprising success of devices based on thin semiconductor films for photonic and electronic applications, which started more than 40 years ago. Many of them, such as transistors, solar cells or lasers take advantage of the interfacial phenomena. Thus, the introduction of interfaces into semiconductor structures gave rise to numerous devices of immense utility and interesting physical properties.

Analogously, the introduction of active interfaces into oxide structures is expected to generate a new technological revolution in the coming years; the interfaces between complex oxides are currently in the spotlight of intense research in Condensed Matter Physics.

A wide range of phenomena is exhibited by these interfaces such as magnetism, superconductivity, ionic conduction or ferroelectricity, which can find direct application for instance, in batteries, fuel cells, diverse information storage technologies, etc [2].

In the past decades, the development of powerful deposition techniques such as pulsed laser deposition, sputtering or molecular-beam epitaxy have allowed the growth of well-defined interfaces of these complex oxides. This atomic-scale engineering opens a world of possibilities to explore and make use of the fundamental properties of such interfaces, with new and more fascinating properties awaiting to be discovered and studied.

1.1 $LaAlO_3/SrTiO_3$ interface

The electrical conductivity at the (001) interface between lanthanum aluminate ($LaAlO_3$, LAO) and strontium titanate ($SrTiO_3$, STO) was first discovered by Ohtomo and Hwang in 2004 [3]. Despite both materials being electrical insulators with wide band gaps (5.6 and 3.2 eV, respectively), a two-dimensional electron gas (2DEG) of a few unit cells was found at their interface. In addition, the 2DEG exhibits a high carrier mobility at low temperatures, exceeding 10.000 cm^2/Vs [3].

This unexpected finding received a lot of attention, stimulating an intense research to understand the fundamental mechanism underlying and led to the emergence of a completely new field called oxide interfaces [4, 5]. This field explores the possibility of oxide-based electronics as an alternative to conventional semiconductor technology based on silicon [6].

As a consequence of this extensive research, new exciting interfacial properties were revealed at the LAO/STO (001) interface, such as magnetoresistance [7], superconductivity [8] and ferromagnetism [9], most of them absent in their bulk constituents. Nevertheless, very specific conditions are required to make the 2DEG emerge at the interface between these two insulators. For instance, the LAO/STO interface presents a critical thickness of the LAO layer, above which an abrupt transition from insulator to metallic-like character is produced [10]. It was also found that such 2DEG is very sensitive to STO surface termination, only being observed when LAO is grown on TiO_2-terminated (n-type interface) but not for SrO-terminated (p-type interface) STO

substrates, suggesting that the details of the interface do matter [3]. Also the growth conditions of the LAO layer are crucial; the conduction appears only when the thin film is grown at low oxygen pressures ($P \leq 10^{-2}$ mbar) [11–13].

The properties of this interface are well characterized and studied, but the exact mechanism to explain the phenomena is still debated and researchers continue to investigate this system. Three main scenarios have been proposed for describing the metallic conduction at the LAO /STO interface: **i)** An electronic reconstruction to cancel the electric field built up at a polar TiO_2-LaO interface (the so-called polar catastrophe scenario); **ii)** the presence of charged oxygen vacancies at either STO or/and LAO; and **iii)** an ionic reconstruction in the form of cation intermixing. Only the first scenario is related with intrinsic properties of the system, whereas the other two are linked with extrinsic effects (vacancies). The consequences of each of these three hypotheses are explained in more detail in the Sections below.

1.1.1 The polar catastrophe scenario

Two years after the discovery of the 2DEG at the LAO/STO interface, Nakagawa *et al.* [14] proposed the polar catastrophe model to explain this behaviour. This model establishes that an electronic reconstruction occurs in response to the polar discontinuity formed at the atomically abrupt interface between the polar $(La^{3+}O^{2-})^{+1}/(Al^{3+}O_2^{2-})^{-1}$ ionic layers of (001) $LaAlO_3$ and the neutral $(Sr^{2+}O^{2-})^{0}/(Ti^{4+}O_2^{2-})^{0}$ ionic layers of (001) $SrTiO_3$.

This results in a valence discontinuity across the interface as shown in Fig. 1.1 a), and builds up an electric potential (V), which diverges as the LAO thickness increases. Consequently, an spontaneous electronic reconstruction is produced in response to this instability, transferring half an electron per two-dimensional unit cell from the LaO^{+1} layer to the TiO_2^0 sublayer [15]. The overall structure remains neutral, with the $Ti^{3.5+}$ ion at the interface layer and the potential no longer diverges (see Fig. 1.1 b). As a result of free electrons occupying Ti $3d_{xy}$ orbitals in the STO layer, the interface becomes conducting and a high mobility

2DEG is established at the unit cells closer to the interface.

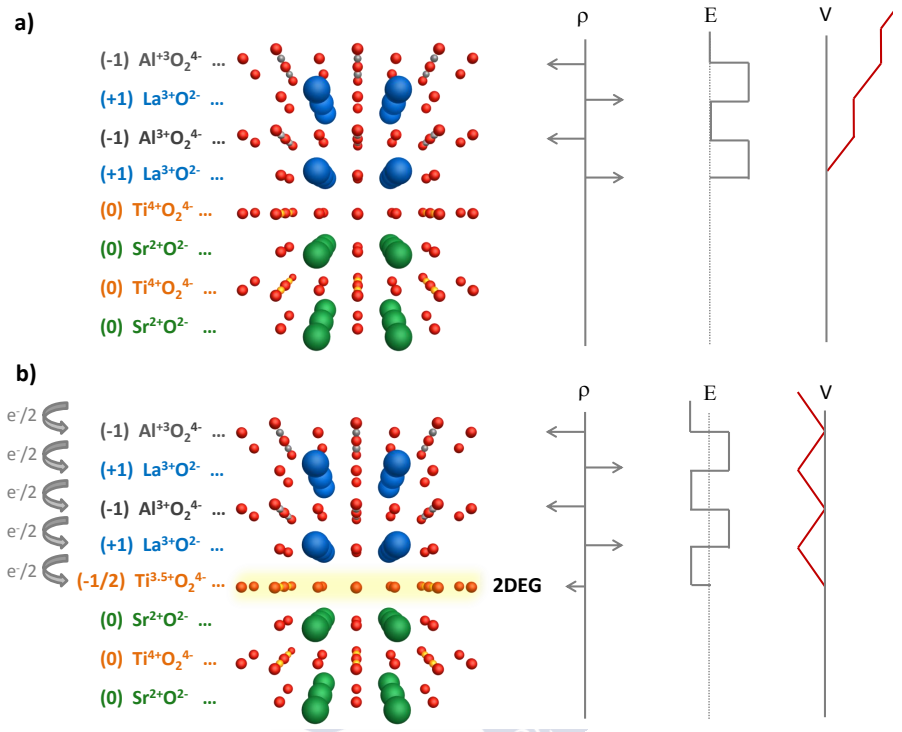

Figure 1.1: Schematic illustration of the polar catastrophe scenario in an AlO_2/LaO/TiO_2 interface. a) Before the electronic reconstruction. The polar layers of LAO grown on non-polar STO substrate produce a negative electric field (E), leading to an electric potential (V), which diverges with sufficient LAO thickness. b) After the reconstruction. The voltage divergence is avoided through the transfer of half an electron per unit cell to the TiO_2 layer. Thus, E oscillates around 0 and the electric potential remains finite. ρ represents the net charges at each layer. Grey, blue, orange, green and red spheres refer to the Al^{3+}, La^{3+}, $Ti^{3.5+/4+}$, Sr^{2+} and O^{2-} atoms, respectively.

The excess of charge incorporated to the interface corresponds to an expected carrier density around 3.5×10^{14} cm^{-2}, which is one order of magnitude above the experimental values reported by various groups ($\sim10^{13}$ cm^{-2}) [16, 17]. Several explanations have been proposed for

this "missing charge" problem, among which the localization of part of the conduction electrons could be the most plausible. In this sense, DFT calculations by Popovic $et\ al.$ [16] revealed that some electrons are confined to a single interfacial layer and therefore, they are susceptible to Anderson localization due to disorder, whereas other electrons with small masses and extended over several layers are expected to contribute to electronic transport. Such disorder could result from structural distortions at the interface due to the strain that arises from the lattice mismatch between LAO and STO ($\approx$+2.9%) [18].

In 2006, Thiel et $al.$ [17] reported that a minimum thickness of 4 unit cells for the LAO layer is required for the formation of the 2DEG, and also first-principles calculations based on the polar catastrophe scenario confirms this critical thickness [19]. In fact, the existence of a critical LAO thickness as a pre-requisite for interfacial conductivity to emerge is the strongest argument in favour of the electronic reconstruction picture. However, the observation of the 2DEG in amorphous layers [20] as well as in other polar interfaces [21] cannot be explained correctly by this model.

Another important problem of the model is the extension of the 2DEG. Ab-initio calculations by Janicka $et\ al.$ [22] predicted that the 2DEG is confined in STO within $\approx$1 nm away from the interface. However, Basletic $et\ al.$ [23] mapped the spatial distribution of charge carriers in LAO/STO heterostructure using a conductive tip of atomic force microscopy. They found that the 2DEG is extended 500 μm to the STO side in samples grown by Pulsed Laser Deposition (PLD) at 10^{-5} mbar (Fig. 1.2 a), meanwhile the conducting depth decreases to 7 nm in interfaces annealed at 300 mbar of oxygen (Fig. 1.2 b).

Herranz $et\ al.$ [24] also deduced from the analysis of Shubnikov-Haas oscillations a thickness of $\approx$500 μm in LAO/STO samples grown by PLD at an oxygen pressure of 10^{-6} mbar. Meanwhile, Reyren $et\ al.$ [8] estimated the conducting thickness around 10 nm at low temperatures on samples deposited at an oxygen pressure of $\approx 10^{-5}$ mbar and post-annealed in 400 mbar. All these results point towards the importance of the growth and annealing conditions in LAO/STO interfaces, which suggest an important role of oxygen vacancies.

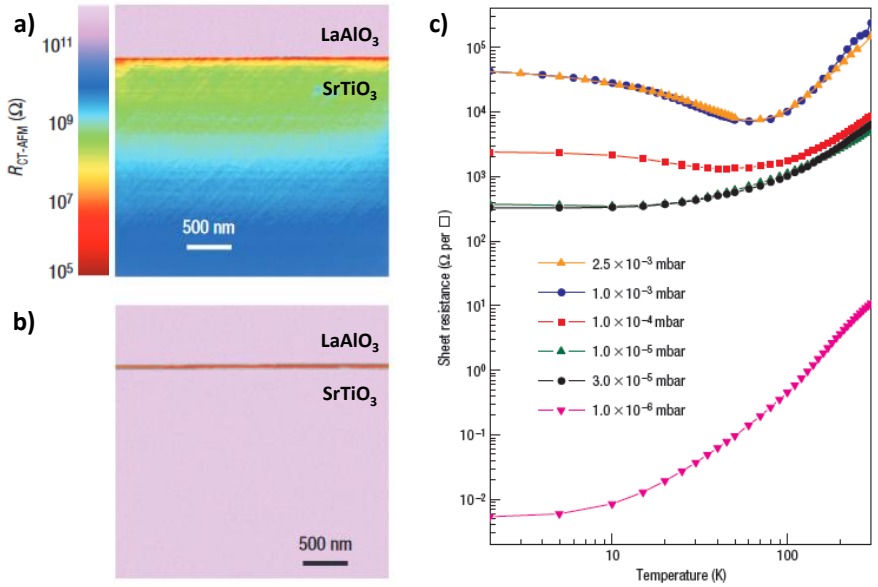

Figure 1.2: a) Map of electrical resistance across the LAO/STO interface for a sample deposited at an oxygen pressure of 1×10^{-5} mbar, and b) sample grown at 1×10^{-6} mbar with a post-annealed procedure at 300 mbar. Reprinted by permission from [23]. c) Temperature dependence of the sheet resistance for 6 samples grown under different oxygen atmosphere and no-annealed. Reprinted by permission from [7].

The LAO/STO interfaces in which the 2DEG is reported so far, have been grown on STO substrates under reducing conditions [8, 25, 26]. In this regard, Brinkman *et al.* [7] revealed a pronounced increase of the interface conductivity as the oxygen pressure of the growth of the LAO thin film decreases, as can be seen in Fig. 1.2 c).

On the other hand, G. Herranz et *al.* [27] demonstrated the formation of a 2DEG at interfaces involving (110) (non-polar) and (111) (polar) surfaces of STO interfaced with epitaxial layers of LAO and above the critical thickness. In the same paper, they also reported the conductivity at the interface between (110) STO substrate and amorphous LAO, STO and yttria-stabilized zirconia (YSZ), showing that epitaxial interfaces are not a pre-requisite for the formation of a 2DEG. This

along with the lack of polar discontinuity at the (110) interface, calls into question the polar catastrophe model and claims for an alternative explanation of the origin of this phenomenon.

Therefore, although some experimental and theoretical studies support the idea of the polar reconstruction scenario, other important issues are still unresolved.

1.1.2 The oxygen vacancies scenario

Soon after the polar catastrophe mechanism was proposed, several groups realized that the electronic properties of the interface are significantly affected by the presence of oxygen vacancies. Many experimental evidences suggest that the spontaneous formation of oxygen vacancies in STO during the typical conditions used to grow the LAO thin film play a fundamental role in the appearance and properties of the 2DEG.

Even though the current deposition methods provide an excellent control in the fabrication of the thin films and interfaces, there is always the possibility that defects, such as anionic or cationic vacancies, will be added to the crystal structure. Their role can be specially important in depositions that involve perovskites, in which the cation valence can change depending on the oxygen content of the sample.

In general, the growth of LAO layers is carried out at high temperatures and in a reducing oxygen pressure (i.e. P_{O_2}=10^{-4} – 10^{-2} mbar), conditions that are very suitable for creating oxygen vacancies in STO. For each ionized oxygen vacancy, two free electrons can be incorporated to the $3d$ conduction band of the STO, modifying the Ti^{4+}/Ti^{3+} valence, as is illustrated in Fig. 1.3 a). Since STO undergoes an insulator-to-metal transition at remarkably low charge carrier densities (1×10^{16} cm^{-3}), a slight deviation from stoichiometry of just one oxygen vacancy every 150 unit cells, is enough to make the oxide an electrical conductor. Therefore, a contribution from oxygen vacancies to the total carrier density cannot be excluded a priori.

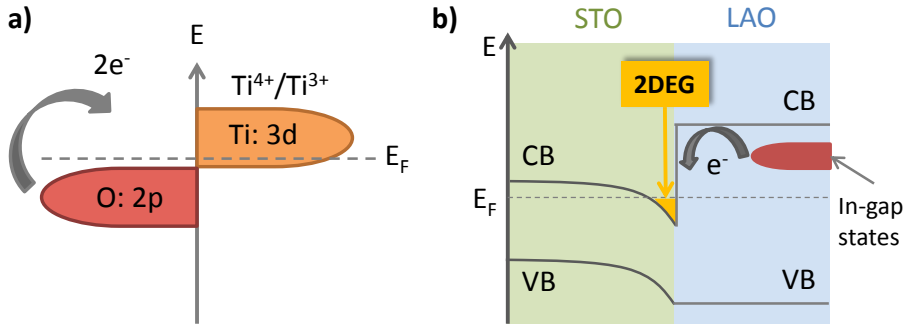

Figure 1.3: a) Schematic illustration of the ionization process of an oxygen vacancy. Every oxygen vacancy yields two electrons in the Ti-3d band of STO, which contributes to the conduction of the material. b) The creation of vacancies in STO produces the appearance of in-gap states close to the conduction band of STO, favouring the conduction at the interface.

In addition, post–annealing processes at high oxygen pressure could result insufficient to recover the oxygen stoichiometry. Numerous studies have examined the conditions of growth and post-annealing in an effort to understand the role of oxygen vacancies. Chen $et\ al.$ [20] reported that a post-annealing procedure removed the oxygen vacancies in the case of amorphous LAO overlayer, but some residual conductivity is preserved in the interfaces with crystalline LAO overlayer [11]. This reveals that oxygen vacancies are the dominant source of mobile carriers when LAO film is amorphous, but it seems that both oxygen vacancies and electronic reconstruction could contribute to the interface electron gas at the unannealed crystalline LAO/STO structure.

Dittman et $al.$ [13] also discussed about the role of the oxygen pressure used in the post-annealing process over the electronic properties of LAO/STO interface. They concluded that equilibrium defect formation is the dominant process for establishing the 2DEG properties, meanwhile growth dynamics plays a minor role in the typical growth regime of LAO/STO interfaces. Cavillieri $et\ al.$ [28] observed a conductive interface for 2-3 unit cells of LAO when the deposition is performed at low oxygen pressures. However, a post–annealing procedure at high

oxygen pressure completely suppressed the conductivity, confirming the oxygen vacancies as responsible for the metallic conduction.

Many theoretical studies also addressed this issue of oxygen vacancies at the LAO / STO interface, concluding that the presence of vacancies is essential for the formation of a 2DEG [29, 30].

All these evidences raised doubts about whether charge transfer across the interface is really responsible of the conducting interface and supports the possibility that the 2DEG resides solely in STO due to the presence of vacancies. In addition, the 2DEG observed at LAO/STO interface shows much similarity to those reported in other STO-based heterostructures (e.g. $LaTiO_3$/STO [31], $GdTiO_3$/STO [32] or $LaGaO_3$/STO [33]) and field–effect–transistor structures involving STO [34,35], which suggests that different forms of electronic confinement at the surface of STO would lead to essentially the same 2DEG.

In this context, Santander-Syro *et al.* [36] reported Angle-Resolved Photoemission Spectroscopy (ARPES) of the surface of STO crystals cleaved under high vacuum. They observed the emergence of a 2DEG at the bare surface of STO, suggesting the critical role of oxygen vacancies on this phenomenology.

In this sense, there are also studies that suggest that vacancies formed on the surface of the LAO could influence in the properties of LAO/STO interfaces. The electronic reconstruction scenario proposed by Nakawaka *et al.* [14] for n-type LAO/STO interface, demands the ionization of some of the oxygen atoms at the upper layer of AlO_2. DFT calculations performed by Li *et al.* [29] revealed that these oxygen vacancies may reduce the electrostatic energy in LAO, being energetically the most stable. In addition, the charge carriers release by the oxygen vacancies on the LAO surface would be transferred to the interface, creating in-gap states located just below the LAO conduction band, as is depicted in Fig. 1.3 b). The charge carriers donated by these in-gap states would be confined to the interface, forming a 2DEG.

Therefore, in view of the results of extensive research about the role of oxygen vacancies in either the $SrTiO_3$ substrate or the $LaAlO_3$ surface, it seems unavoidable to consider its effect for a proper understanding of the properties of the 2DEG at the (001) LAO/STO interface.

1.1.3 Cation intermixing at the LAO/STO interface

The third possible mechanism proposed to be responsible for the metallicity of the system involves an atomic reconstruction at the LAO/STO interface. This may be due to two reasons: i) an ionic reconstruction induced by the polar field of the interface, or ii) by the effect of the kinetic growth conditions during the deposition process (generally by PLD or sputtering).

Some polar surfaces present in nature show tendency for reconstruction, such as the ionic rock salts FeO (111) or NiO (111). The unreconstructed polar surfaces can be covered by hydroxyl groups (–OH) that avoid the reconstruction, but removing –OH destabilizes the surface and leads inevitably to the reconstruction [37]. Another famous example is the ZnO surface, which shows stability regardless of its polarity. In this case, the stability is attributed to the high degree of disorder at the surface [37].

Therefore, independently of the level of growth control attainable with modern deposition techniques, the growth of a polar material on non-polar substrates causes a discontinuity, which introduces a larger energy cost to form atomically abrupt heterointerfaces. Particularly in ionic oxides, the atomic reconstruction can often occur to avoid the build up of an electrical potential at a polar surface or interface, resulting in a rougher interface [38].

Nakagawa *et al.* [14] compared the roughness of n-type and p-type interfaces; they concluded that the n-type interface showed significantly more roughness induced by a compensation mechanism to avoid the polar discontinuity (see Fig. 1.4). Moreover, Qiao *et al.* [39] proved that an intermixed interface is thermodynamically more favourable than an abrupt interface.

In addition to the aforementioned interdiffusion of cations, numerous studies point to the existence of structural distortion of the unit cells around the interface, which would favour to the high mobility of the electrons [18, 40, 41].

On the other hand, Willmott *et al.* [42] also demonstrated that the n-type LAO/STO interface is not abrupt, and additionally they deter-

mined that Sr and La intermix at a greater depth than Ti and Al ions, resulting in the formation of metallic $La_{1-x}Sr_xTiO_3$. This along with structural distortions could explain the emergence of 2DEG at the interface based on structural considerations.

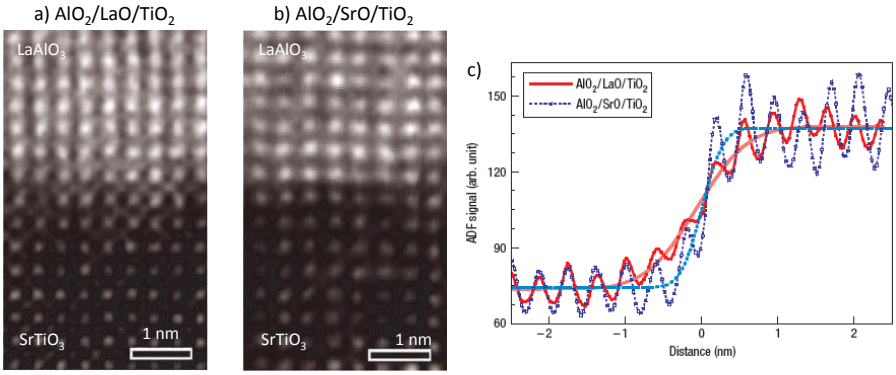

Figure 1.4: a) $LaAlO_3$ layers grown on TiO_2-terminated $SrTiO_3$ substrate forming the $AlO_2/LaO/TiO_2$ interface (n-type interface). b) $LaAlO_3$ grown on SrO-terminated $SrTiO_3$ forming the $AlO_2/SrO/TiO_2$ interface (p-type interface). c) Averaged line profiles across the interfaces of a, b. The extracted r.m.s roughness (σ) for the $AlO_2/LaO/TiO_2$ interface showed in a) is σ=1.90$\pm$0.11 u.c. and for the $AlO_2/SrO/TiO_2$ interface displayed in b is σ=0.77$\pm$0.13 u.c. Reprinted by permission from [14].

After years of theoretical and experimental efforts, there is still no consensus regarding the dominant mechanism responsible of the high-mobility 2DEG. Each of the three scenarios discussed above can explain particular experimental results, but a unified image is missing to describe the origin of the 2DEG and, above all, it is not clear if one or a combination of all the mechanisms can be the most adequate response to explain the experimental observations. In general, it has become accepted that the novel behaviour emerges as a result of a combination of the polar catastrophe and growth-induced defects, specifically oxygen vacancies. However, the complex interplay between these effects remains undetermined.

1.2 Strain and defect engineering of transition metal oxides

The (001) LAO/STO interface represents one of many cases where new functionalities can arise at oxide interfaces. But, where does this wide range of phenomena come from?

On the one hand, the fact that d-orbitals participate in the bonds between the transition metal and oxygen ions results in strong electron correlations within narrow bands with d-character [43]. This along with a large coupling between charge, spin and orbital degrees of freedom, are responsible for the variety of electronic and magnetic behaviour characteristic of these compounds, such as metal-insulator transition, superconductivity, ferroelectricity, multiferroicity, etc [44]. On the other hand, the crystal structure of complex oxides is very flexible in terms of composition. The latter is crucial for the development of novel materials and moreover provides a wide range of diverse oxide compounds that can be deposited on top of each other forming interesting interfaces.

Particularly appealing within them are the oxoperovskites of general formula ABO_3, in which the relatively free substitution of certain cations in the structure leads to a large variety of perovskite-type metal oxides. The cation substitutional routes are mainly three: i) replacement by another cation with the same valency; ii) by a combination of cations with a different valence, such that the net charge remains identical; or iii) substitution by a cation with different valence, which produces a reduction or oxidation of the second metal ion, to compensate the charge difference (e.g. $La^{2+}_{1-x}Sr^{2+}_{x}Ti^{3+}_{1-x}Ti^{4+}_{x}O_3$).

Furthermore, the possibility of controlling the occupancy of the anion site is equally appealing (in this case the oxide ion, O^{2-}), although much less explored.

Growing epitaxial thin films of an oxoperovskite on top of a substrate provides an opportunity to tailor and fine-tune the electron correlations through a strain-mediated control of the bond distances and angles, as well as the concentration and distribution profiles of defects

(i.e. cationic and/or anionic vacancies) within the lattice.

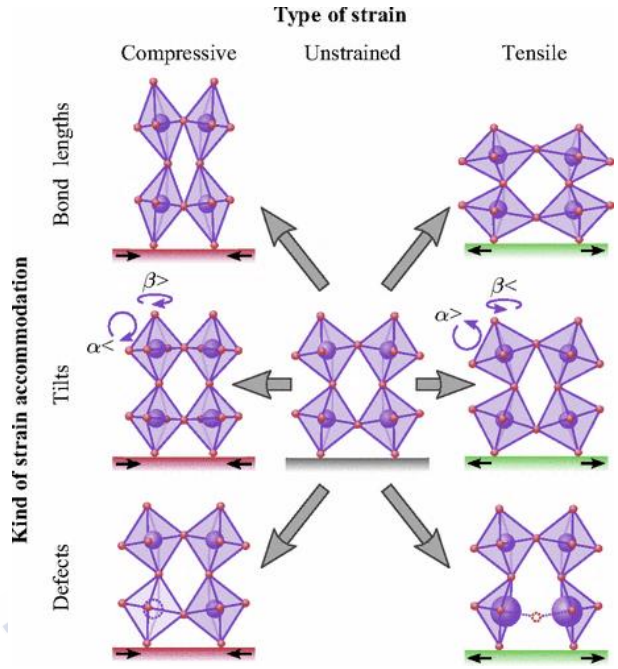

Figure 1.5: Sketch of possible mechanisms for epitaxial strain accommodation in oxoperovskites ABO_3: i) by bond-length changes (upper row); ii) by changes in octahedral tilts (α) and rotations (β) (central row); or iii) by point defect formation (lower row). The illustration shows the effects depending on the sign of strain: negative (compressive), no strain and positive (tensile) in left, central and right column, respectively. Cations at the A-site have been omitted for clarity. Reprinted by permission from [45].

When a film of an oxoperovskite is grown coherently on a substrate with a different lattice size, the internal stress due to the change in the in-plane lattice constant can be accommodated through three main mechanisms, which are depicted in Fig. 1.5. The first mechanism involves structural distortions through changes in the internal bond lengths, which can induce interesting phenomena such as the cooperative Jahn-Teller effect [46]. The second effect of the change in the lattice

parameter forced by coherent growth is a modification of the angle or rotation pattern and tilts of the oxygen octahedra [47], which in turn have been shown to influence numerous functional properties such as ferroelectricity [48] or magnetism [49].

The third mechanism involves the appearance of point defects in the form of cationic/anionic vacancies, interstitial atoms, substitutions, etc. It is very likely that both strain and point defects influence the molar volume and, consequently the Gibbs free energy, resulting in strain dependent defect formation energies. The nature of point defects strongly depends on the sign of strain. Thus, compressive strain normally tends to increase the concentration of cationic vacancies. This is a consequence of the charge balancing oxidation of cations with smaller ionic radii at higher oxidations states. On the other hand, tensile strain produces an increase of the volume, which promotes the formation of oxygen vacancies. The latter is a well-recognized way to accommodate large epitaxial strains in oxides, through donation of two electrons to the conduction band, which is of anti-bonding character to the B–O bond [50].

It has been demonstrated that strain is a powerful tool for manipulating the oxygen vacancy concentration driving changes in material's properties. For instance, Petrie $et\ al.$ [51] reported a transition from ferromagnetic metal to antiferromagnetic insulator in the strontium cobaltite ($SrCoO_x$), which is controlled through changes in oxygen content. Meanwhile, Becher $et\ al.$ [52] revealed a coupling between structural defects and electric polarization mediated via strain engineering.

Understanding the distinct mechanisms to accommodate the coherent epitaxy of the thin films requires the introduction of the concept of tolerance factor.

Goldshmidt tolerance factor (t) is extensively used to predict the degree and type of crystallographic distortions of perovskites, after accommodating different size cations. This parameter is a measure of the mismatch between the equilibrium (A-B) and (B-O) bond lengths for

ABO_3 perovskites [53]:

$$t = \frac{R_A + R_O}{\sqrt{2}(R_B + R_O)} \tag{1.1}$$

where R_A, R_B and R_O are the ionic radius of A, B and Oxygen atoms, respectively [54]. Thus, a tolerance factor $t = 1$ results in a cubic structure, whereas any deviation from 1 causes the formation of a perovskite with an structure of lower symmetry.

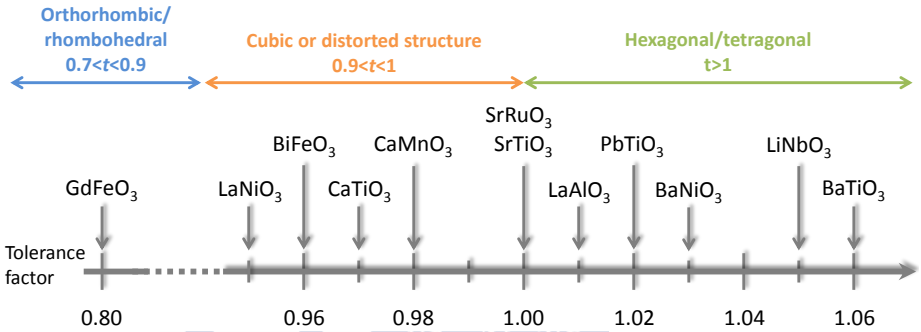

Figure 1.6: Goldshmidt tolerance factor of some important perovskites. Data extracted from [55]

A t<1 indicates either A ion is smaller than the size of the void or B ion is too large, resulting in the BO_6 rotation along (001), (111) or (110) axis to maximise atomic packing. This produces rhombohedral or orthorhombic symmetry, so that the symmetry of the crystal structure is lowered. Some examples of this type of perovskite are $GdFeO_3$ (t=0.80, orthorhombic) or $BiFeO_3$ (t=0.96, rhombohedral). On the contrary, t>1 is due to larger A size or smaller B ion, adopting a tetragonal or hexagonal structure, such as $BaTiO_3$ (t=1.06, tetragonal) (see Fig. 1.6).

On the other hand, the manipulation of octahedral rotations in perovskites is a well recognized strategy to modify their properties; small changes may cause a subtle effect on electronic and magnetic behaviours

through spin–orbit coupling [56, 57]. In this regard, either the selection of the substrate or the presence of defects can lead to a determined cooperative rotation of the BO_6 octahedra. The substrate, apart from imposing stress on the thin film due to the connectivity of the BO_6 between film and substrate, can transfer its own octahedral configuration across the heterointerface, imprinting it into the film [58].

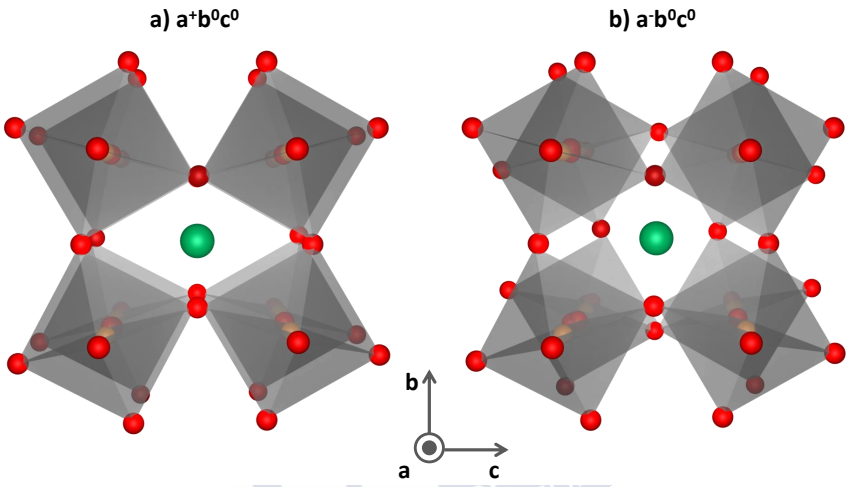

Figure 1.7: Schematic illustration of the in-phase (a) and out-of-phase (b) cooperative TiO_6 rotations along the a-axis in a perovskite structure.

Glazer introduced a notation to describe all the possible octahedral tilting distortions in perovskites [59]. This notation specifies the BO_6 tilts or rotations along each of the three pseudocubic axes (a (100), b (010) or c (001)). The letters also show whether the magnitude of the tilt is equal or different along the spatial directions. For example, $a^+a^+a^+$ indicates the same magnitude of rotation along the three axes whereas $a^+b^+c^+$ denotes different angle of rotation about each axis. Moreover, the superscript $+$ indicates that the rotations of neighbouring octahedra along the given axis occur in-phase (Fig. 1.7 a), whereas the out-of-phase rotation is denoted as $-$ (Fig. 1.7 b). The absence of tilting is expressed as 0. Using this notation, 23 different tilt systems describe all

the possible octahedral configurations in perovskites.

Understanding the effect of epitaxial growth of oxoperovskites inevitably implies the correct determination of the octahedral rotations within the thin films. This is especially important, since it could strongly affect the formation of ionic defects and their diffusion through the lattice, as well as the electronic transport properties of the films. For these reasons, this aspect will be studied in detail in this Thesis.

1.3 Structure and properties of $SrTiO_3$

Strontium titanate ($SrTiO_3$) is a quantum paraelectric insulator [60], whose great chemical stability, diamagnetism and high dielectric constant makes it one of the preferred templates for the growth of other oxoperovskite thin films, and it is the basic ingredient of the aforementioned (001) LAO/STO interface.

At room temperature, $SrTiO_3$ presents a cubic perovskite structure (space group $Pm3m$). Below 105 K, it undergoes a structural transition to a tetragonal structure (space group $I4/mcm$), which presents an out-of-phase rotation of the TiO_6 octahedra along the (001) axis ($a^0a^0c^-$).

The undistorted STO structure is sketched in Fig. 1.8. The Ti^{4+} ions are sixfold coordinated by oxygen O^{2-}, whereas each Sr^{2+} is surrounded by four TiO_6 octahedra (ninefold coordination to O^{2-} ions). Within the TiO_6 octahedra, the hybridization of the O-$2p$ states with the Ti-$3d$ states leads to a pronounced covalent bonding, meanwhile Sr^{2+} and O^{2-} ions present ionic bonding character. It is precisely this mixed covalent-ionic bonding properties that makes it a model electronic material.

STO is a good example of the richness in properties of the oxoperovskites [61–64]. These can be further enhanced through doping, presence of vacancies or the change in bond distances and angles produced by epitaxial strain. Thus, n-doping through replacement of Ti^{4+} by Nb^{5+} or La^{3+} by Sr^{2+}, transforms STO in a conducting system and gives rise to practical applications such as gas sensors [65], electrodes in solar cells [66] or dielectric in capacitors [67, 68].

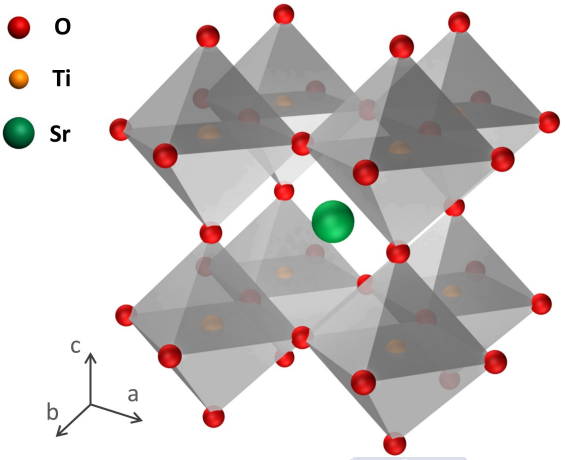

Figure 1.8: Schematic representation of the cubic undistorted $SrTiO_3$ structure (space group $Pm3m$). Each Ti atom (orange spheres) is bonded to six O atoms (red spheres), forming an corner-sharing octahedral structure. Each Sr atom (green sphere) is surrounded by four octahedra.

Nevertheless, oxygen vacancies ($V_{\ddot{O}}$) are probably the most likely to add new functionalities to STO. They are easily formed by processing STO in an oxygen-reducing atmosphere without any further cation substitution. Moreover, due to their donor character and the very large electron mobilities characteristic of δ-doped STO, even the slightest concentration of vacancies produces a measurable electrical conductivity. Actually, reduced STO was the first oxide reported to show superconductivity, with a maximum $T_c \approx$ 0.3 K for electron densities of $n \approx 10^{20} cm^{-3}$ [69]. However, incorporation of oxygen defects may be detrimental for some applications of this oxide; for instance, those with high-k requirements of dielectric insulating layers for carriers density modulation can be compromised.

Among the properties induced by oxygen vacancies, resistive switching is one of the most prominent [70–74]. The high mobility of oxygen vacancies in comparison with cation vacancies in STO can lead to an important oxide-ion conductivity at a not too high temperature. In addition, each $V_{\ddot{O}}$ is positively charged, which makes them sensitive to

being moved within the material by an electrical field. Thus, the movement of vacancies along filaments based on dislocations has already been reported [75] in single crystals as well as in thin films [76].

On the other hand, each vacancy donates its electrons to a band that is anti-bonding in character with respect to the Ti-O bond. This effect produces a chemical expansion around it, and therefore the distribution of vacancies is sensitive to local strain fields. In this regard, Sharma $et\ al.$ reported the movement of oxygen vacancies by means of the mechanical force exerted by an AFM tip in LAO/STO interfaces, taking advantage of the Vegard's effect [77].

Another property that attracts extensive interest for its potential applications is ferroelectricity. As an incipient ferroelectric, STO can undergo a ferroelectric transition by diverse methods such as doping [78, 79], electric field [80] or isotope substitution [81]. But even more important, Haeni et $al.$ [82] first demonstrated room-temperature ferroelectricity in STO by means of the application of strain. They found that STO thin films deposited under tensile strain present in-plane ferroelectric polarization at temperatures close to room temperature, whereas compressive strain only generates ferroelectricity at very low temperatures, and of a much smaller magnitude. The different ferroelectric phases stabilized on STO thin films by epitaxial strain are shown in the phase diagram of Fig. 1.9.

Later, Jang et $al.$ [83] examined the ferroelectricity in strain-free STO films and bulk crystals, determining that they are relaxor ferroelectrics, and the role of strain is to stabilize long-range correlation of pre-existing nanopolar regions within STO. These authors also point to the minimal presence of unintentional Sr deficiency in the samples as the origin of the nanopolar regions, emphasizing the delicate sensitivity of the STO to deviations in its stoichiometry.

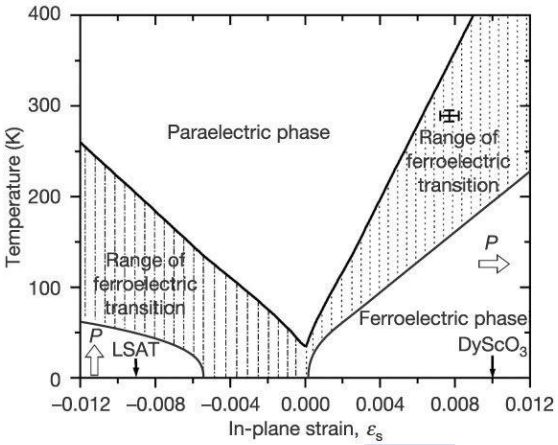

Figure 1.9: Phase diagram of ferroelectricity in STO thin films as a function of temperature and in-plane epitaxial stress. The arrows indicate the direction of the polarization for strained STO. Reprinted by permission from [82].

Thermoelectricity is another important property that was recently reported at doped $SrTiO_3$ thin films and interfaces. Although the thermoelectric conversion performance of STO still remains low because of its high thermal conductivity, the large Seebeck coefficient and electrical conductivity reported in lightly doped thin films makes it a firm candidate to be used in thermoelectric devices. Several strategies were explored to improve its thermoelectric properties, such as strain [84] or cationic doping [85].

The most promising approach involved the 2DEG formed at the STO surface and the possibility to be modulated by means of diverse techniques, improving considerably the thermoelectric efficiency of the material. In this regard, Ohta *et al.* [86] proposed the fabrication of STO superlattices, in which e-doped $SrTi_{0.8}Nb_{0.2}O_3$ layers are inserted between insulating STO thin films, as is illustrated in Fig. 1.10 a). Thus, a 2DEG with high carrier density ($\approx 10^{21} cm^{-3}$) is formed at the TiO_2/STO heterointerface. They reported an unusually large Seebeck coefficient (S), when the thickness of the conductive layers was less than 4 unit cells. The maximum value ($\approx 490\ \mu VK^{-1}$) is reached for 1

unit cell of the $SrTi_{0.8}Nb_{0.2}O_3$, which is approximately 4.4 times larger than the Seebeck coefficient reported in bulk for similar carrier densities.

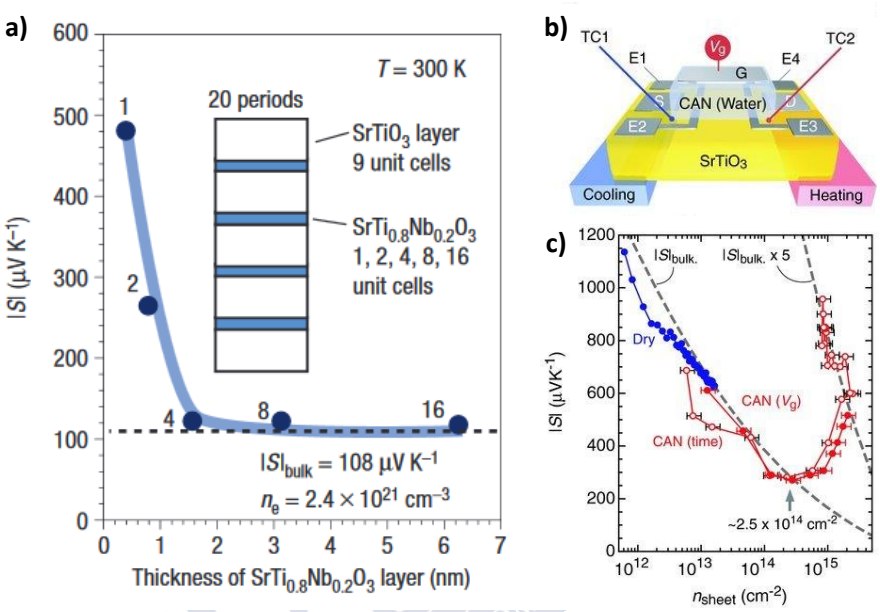

Figure 1.10: a) Seebeck coefficient at room temperature as a function of the thickness of the $SrTi_{0.8}Nb_{0.2}O_3$ layer for superlattices composed by STO/$SrTi_{0.8}Nb_{0.2}O_3$/STO. A sudden increase is produced when the thickness is smaller than 1.56 nm. Reprinted by permission from [86]. b) Sketch of the CAN-gated STO-based field effect transistor. c) Seebeck coefficient values of the 2DEG as a function of the charge carrier concentration (n_{sheet}), which is modulated by the gate voltage. Reprinted by permission from [87].

Years later, they also achieved a large enhancement of the Seebeck coefficient modulating the 2DEG formed in a field effect transistor device fabricated on an STO substrate and capped by nanoporous calcium aluminate (CAN), which served as a gate insulator (see Fig. 1.10 b). An electric field application provided an extremely thin 2DEG (≈2nm), which exhibits a large S≈950 μVK^{-1} for carrier densities of $\approx 10^{15}$ cm^{-2} (Fig. 1.10 c).

These results open the way to obtain efficient and environmentally-friendly high performance thermoelectric materials, which take advantage of the 2DEG formed at an oxide interface.

In the following pages, we will present the main results obtained during the development of this PhD Thesis to contribute to the current knowledge of the properties of STO. In particular, we will focus on the influence of strain as well as oxygen vacancies in some of the interesting functional properties exhibited by this material in the form of thin films. At the same time, we will aim to contribute to the discussion about the role of oxygen vacancies in all the phenomenology observed in the famous LAO/STO interface.

Thus, we will discuss the effect of epitaxial strain on the energy of formation of oxygen vacancies, as well as on its distribution and mobility at room temperature. Then, we will present a detailed discussion about the controlled movement of oxygen vacancies by means of large local electric fields induced by an AFM tip. Finally, the effect of vacancies on the ferroelectric and magnetotransport properties of STO thin films will be discussed in detail, from an experimental and theoretical point of view, through ab-initio calculations.

2. Experimental techniques

Nothing in life is to be feared, it is only to be understood.
Now is the time to understand more, so that we may fear less.

Marie Curie was the first woman to win a Nobel Prize and the first person to win the award twice. Nobel Prize in Physics in 1903 and Nobel Prize in Chemistry in 1911.

This Chapter presents the deposition technique used to grow the Nb:STO thin films as well as the characterization techniques used to verify the structural quality of the films. Finally, we also provide a description of the methods used to measure the Seebeck effect and the electric transport properties of the samples.

2.1 Pulsed Laser Deposition

Since the late 1980s, Pulsed Laser Deposition is an extensively used technique for the growth of complex oxide thin films. The technique's principle is very simple as is illustrated schematically in Fig. 2.1 b). A high-energy pulsed laser beam is focused on top of a stoichiometric solid target of the material to be deposited, creating an energetic plasma plume which is ejected from the target towards the substrate. The substrate is typically placed over the target and maintained at high

temperature (600-1000°C). Once the ejected material reaches the substrate, the atoms rearrange to adapt to the crystalline structure of the substrate underneath. The entire process is carried out in the presence of a background gas, normally oxygen, nitrogen or argon. Due to the plasma plume is highly focused towards the substrate, PLD is not well suited for large-scale film growth and one of its principal drawbacks is the uneven coverage over large substrates [38].

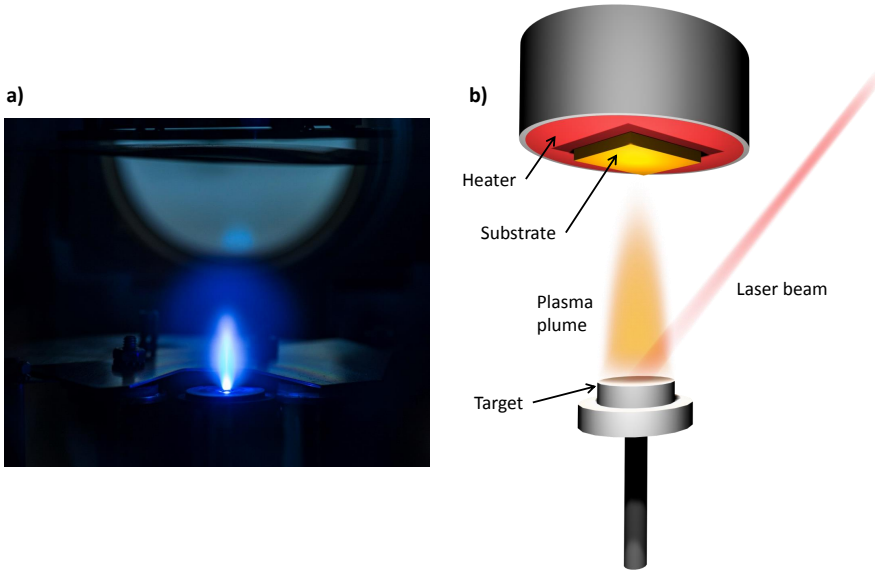

Figure 2.1: Pulsed Laser Deposition system. a) Picture of our PLD chamber in the precise moment when the laser beam hits the target, producing a high energetic plasma plume. b) Sketch describing the different elements of the PLD working process.

The growth of oxide thin films is normally performed under oxygen atmosphere at controlled pressure for two purposes: first, oxygen acts as a scattering center in the route of the atomic species ejected towards the substrate, and second, it provides the oxygen source necessary to achieve the film stoichiometry. Even so, oxygen content can also be modified after the deposition process inside the vacuum cham-

ber itself without extracting the sample, by using oxygen pressure and temperature different from the deposition conditions. Another option is to change the oxygen stoichiometry ex-situ by a subsequent post-annealing treatment at high temperature and a given oxygen pressure (this is the approach followed in this Thesis; more details are provided in Chapter 4).

One of the most important advantages of this technique, which makes it attractive for the growth of complex oxides, is the possibility of a stoichiometric transfer from the multi-cation targets to the substrate, and the capability to control the stoichiometry of the films modifying the oxygen pressure of the vacuum chamber. For this purpose, an accurate optimization of the deposition conditions of both, laser (pulse time, wavelength, repetition rate and laser fluence) and growth parameters (target-substrate distance, substrate temperature and background oxygen pressure) is required. Among these, laser energy and oxygen pressure are probably the key parameters to control the degree of scattering inside the PLD chamber and the ablation of the materials with different atomic weight. As we assume stoichiometric transfer and negligible evaporation from the film surface, only the cation stoichiometry (not the composition of the target) should be identical to that of the films. For many materials, this implies a very narrow window of parameters in which the coherent growth and correct stoichiometry of thin films are achieved.

For the growth of high quality epitaxial thin films with sharp interfaces, an atomically smooth and chemically homogeneous surface of the substrates are also crucial. If the termination layer is not uniquely defined, two types of interfaces can be formed, degrading the interfacial properties due to chemical and electronic inhomogeneities on a unit-cell scale.

Typically, the as-received commercial substrates have a chemically mixed surface, so that a previous chemical treatment is required to achieve atomically flat and chemically single-terminated surfaces. Although the procedure is different depending on the substrate, it is usually composed by a chemical etching and/or a thermal treatment [88]. In the case of this Thesis, all the substrates were treated to obtain a single-

step termination and ensure a coherent and epitaxial growth of the thin films (see Chapter 4 for further details).

2.2 X-Ray Diffraction and Reflectivity

X-Ray Diffraction (XRD) is a non-destructive technique which is commonly used to identify the structural properties of a crystalline solid, providing information about unit cell dimensions, orientation, etc. It is based on the interference between an incident X-Ray beam and a crystalline material, which is formed by periodic rows of atoms separated by a given distance (d-spacing). Since the radiation wavelength is comparable to the distance between crystallographic planes, the interference will be constructive when Bragg's Law is satisfied:

$$n\lambda = 2dsin\theta \tag{2.1}$$

where n is an integer, λ is the wavelength of the X-Rays, d_{hkl} is the interplanar distance for a given Miller index (hkl) and θ is the incident angle (see Fig. 2.2). For XRD measurements, both ω and θ angles have the same value, and remain coupled during the scan. Thus, the interplanar spacing can be obtained by scanning a range of θ and collecting the intensity of the diffracted beam at 2θ. For the simplest case of a cubic lattice, the lattice parameter (a) can be obtained from:

$$a = \frac{\lambda\sqrt{h^2 + k^2 + l^2}}{2sin\theta} \tag{2.2}$$

In this Thesis, X-Rays experiments were performed with the diffractometer Empyrean and X'Pert Pro from PANalytical, which has an incidence wavelength of λ ($K_{\alpha_1}^{Cu}$) = 1.540598 Å. In this equipment is possible to adjust independently the four angles depicted in Fig. 2.2, i.e. ω, θ, ψ and ϕ. The optics and configuration will depend on the type of measurement to be performed.

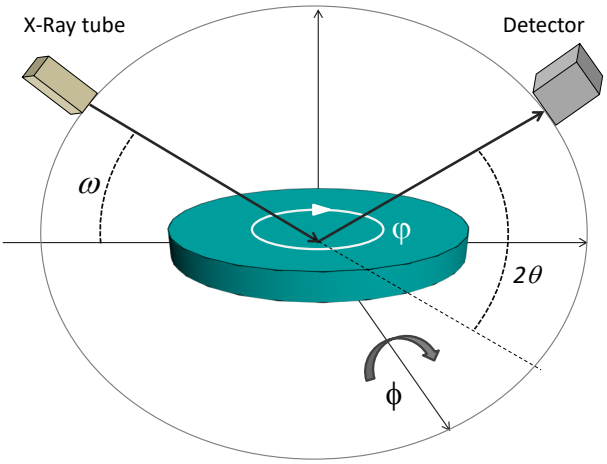

Figure 2.2: Illustration of the four angles (ω, θ, ψ and ϕ) that can be varied independently in relation to the film in the PANAlytical diffractometer used in this Thesis. In this example, ω and θ have the same value corresponding to the symmetric reflection used in the XRD measurement.

Epitaxy is refereed to the template growth of a single crystal film on top of a crystalline substrate. The epitaxial film will have structural coherence, crystallographic orientation and lattice matching to the substrate. The continuation of the substrate structure will be associated with the incorporation of strain into the layer when the unit cells of the film and the substrate are distinct. The strain introduced in the film by the substrate is defined by:

$$s(\%) = \frac{a_s - a_f}{a_f} \times 100 \tag{2.3}$$

where a_s and a_f are the lattice parameter of the substrate and the film in its bulk form, respectively. According to this, heteroepitaxial thin films can grow under compressive stress ($s<0$), tensile stress ($s>0$) or relaxed (s = 0) (see Fig. 2.3).

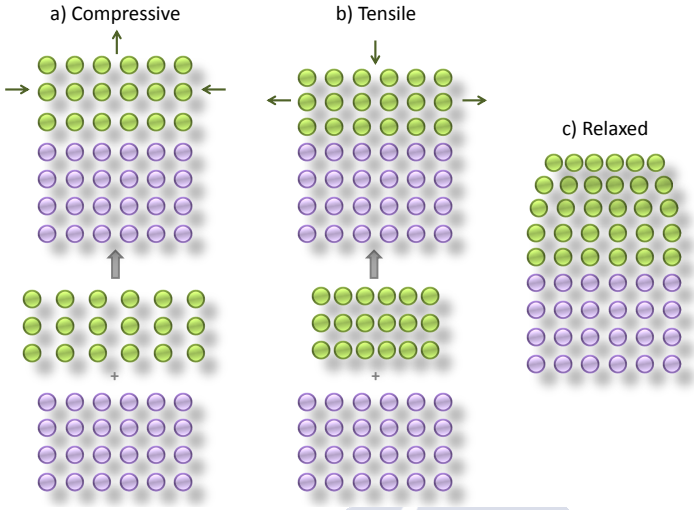

Figure 2.3: Schematic representation of different epitaxial strain accommodation in thin films: a) $a_s < a_f$ compressive strain, b) $a_s > a_f$ tensile strain and c) partially strained or relaxed thin film. Solid purple and green circles represent the lattice of the substrate and the film, respectively. The arrows in a) and b) indicate the direction of thin film deformation to adapt to the substrate in-plane lattice parameter. The deformation will be elastic if the thin film follows the Poisson's ratio.

The Poisson's ratio (ν) is a parameter that quantifies the relative changes of volume and shape of a system in response to an arbitrary mechanical stress, and it is defined by [89]:

$$\nu = -\frac{\epsilon_{xx}}{\epsilon_{zz}} \tag{2.4}$$

where ϵ_{xx} and ϵ_{zz} represent the strain in the transverse and longitudinal directions:

$$\epsilon_{xx} = -\frac{a_{film} - a_{bulk}}{a_{bulk}} \tag{2.5}$$

$$\epsilon_{zz} = -\frac{c_{film} - c_{bulk}}{c_{bulk}} \tag{2.6}$$

The subscripts *film* and *bulk* refer to the lattice parameters of the film and the bulk, respectively. Most materials expand in the out-of-plane direction when an in-plane compressive stress is applied, producing an elastic compensation of the unit cell dimension according to a positive Poisson's ratio. For epitaxial thin films with biaxial (symmetric) in-plane stress, it is defined an effective Poisson's ratio [90]:

$$\nu^* = -\frac{2\nu}{(1-\nu)} \tag{2.7}$$

Reciprocal Space Mapping (RSM). RSM is a high resolution X-Ray Diffraction method which provides a 2D image of the reciprocal space around a Bragg peak. It completely maps the Bragg's reflection under investigation, containing the peaks corresponding to the substrate and film and giving information about in-plane and out-of-plane lattice parameters (*a, c*) of both. The experimental strain of the thin films can also be calculated from the RSM data. Using an asymmetric Bragg reflection, series of 2θ scans for a fixed range of ω (incident angle) values are recorded. The reciprocal space vectors parallel (Q_x) and perpendicular (Q_z) to the surface are obtained from the relationship between incidence and exiting angles given by [91]:

$$Q_x = sin\theta sin(\theta - \omega) \tag{2.8}$$

$$Q_z = sin\theta cos(\theta - \omega) \tag{2.9}$$

The in-plane (*a,b*) and out-of-plane (c) lattice parameters can be calculated directly from the reciprocal space vectors for a cubic system:

$$c = \frac{\lambda\sqrt{h^2+k^2}}{2Q_x} \tag{2.10}$$

$$a = b = \frac{\lambda l}{2Q_z} \tag{2.11}$$

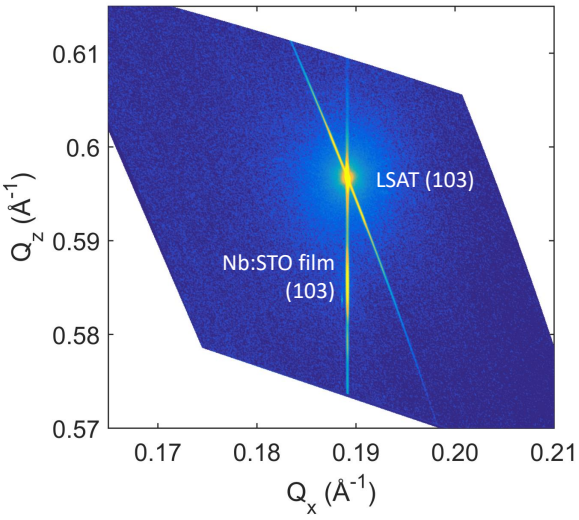

Figure 2.4: Example of RSM around the (103) reflection for a 19 nm-thick of $SrTiO_3$ film growth on a (001) LSAT substrate. The reciprocal space vectors can be transformed into lattice units using the equations 2.8 and 2.9. In this case the film is completely matched to the substrate, adopting the same in-plane lattice parameter (a).

Half-order Reflections. RSM can also provide information about the octahedral tilting on a perovskite by analysing the half-order reflections. In thin films, both growth conditions and the presence of defects can distort the bulk state of the film changing its crystallographic lattice through the rotations of the metal-oxygen BO_6 octahedra.

According to Glazer [59], half-order reflections are produced as a consequence of the existence of octahedral rotations (doubling of the unit cell), only if they are present throughout the thickness of the thin film. Therefore, by studying the presence or absence of characteristic reflections, the precise octahedral configuration of the film can be determined.

Type of tilt	Half-order reflection
a^+	(0,1/2,3/2) or (0,1/2,5/2)
b^+	(1/2,0,3/2) or (1/2,0,5/2)
c^+	(1/2,3/2,1) or (1/2,3/2,2)
a^-	(1/2,1/2,3/2) or (3/2,1/2,3/2)
b^-	(1/2,1/2,3/2) or (1/2,3/2,3/2)
c^-	(3/2,1/2,3/2) or (1/2,3/2,3/2)

Table 2.1: Half-order reflections corresponding with the different octahedral rotations. Extracted from reference [92].

The reflections are indexed with some *hkl* odd and even indices, and can be measured using a standard diffractometer simply doubling the pseudocubic unit cell $2a_{pc}$ x $2b_{pc}$ x $2c_{pc}$. The corresponding half-order reflections for the possible octahedral rotations (both in-phase (+) and out-of-phase(-)) are summarized in the 2.1.

X-Ray Reflectivity (XRR). Another useful technique to characterize thin films is the X-Ray reflectivity. Unlike X-Ray Diffraction, XRR does not measure the diffracted radiation but the reflected signal. Very small incident angles and a symmetric θ-2θ configuration are used.

Depending on the material density (the density difference with the substrate), X-Rays are completely reflected below a critical incidence angle (θ_c). Above θ_c, the incident X-Rays penetrate into the material, leading to interference phenomena and therefore, to the curve with the characteristic intensity oscillations (see Fig. 2.5). XRR allows the determination of surface and interface roughness and most importantly, the thickness of thin films and multilayers, which can be calculated from the period of the fringes [93].

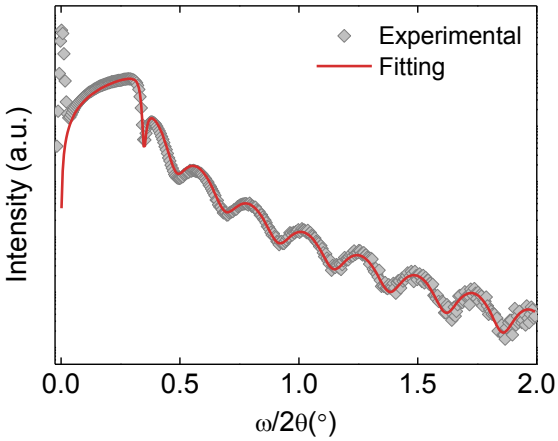

Figure 2.5: The experimental data correspond to a Nb:$SrTiO_3$ thin film deposited on a (001) LSAT substrate. The curve fitting using the X'Pert Reflectivity software provides the value of the density (ρ), thickness (t) and the surface roughness (R) of the film. For this particular sample, the adjusted values are ρ=5.1 g/cm^3, t=18.2 nm and R=0.3 nm.

2.3 Atomic Force Microscopy

Since the discovery in 1986 by Binning and Rohrer of the Atomic Force Microscopy (AFM) [94], this technique has become a powerful tool to characterize the thin film surfaces at the atomic level.

It consists in a small tip attached to a cantilever, which is focused by a laser (see Fig. 2.6). When the cantilever is displaced over the sample surface using a piezo-electric crystal, it experiences an interacting force between the tip and the surface atoms, which bends the cantilever. The deflection of the cantilever is registered by the laser, and its reflection is amplified and recorded using an array of photodiodes. The processed signal is transformed into a height profile. Nowadays, the best cantilevers are able to sense forces down to 1pN with a tip radius less than 1nm. As a consequence, the resolution is typically around 1-10 nm in-plane and 0.1-100 nm in the out-of-plane direction [95].

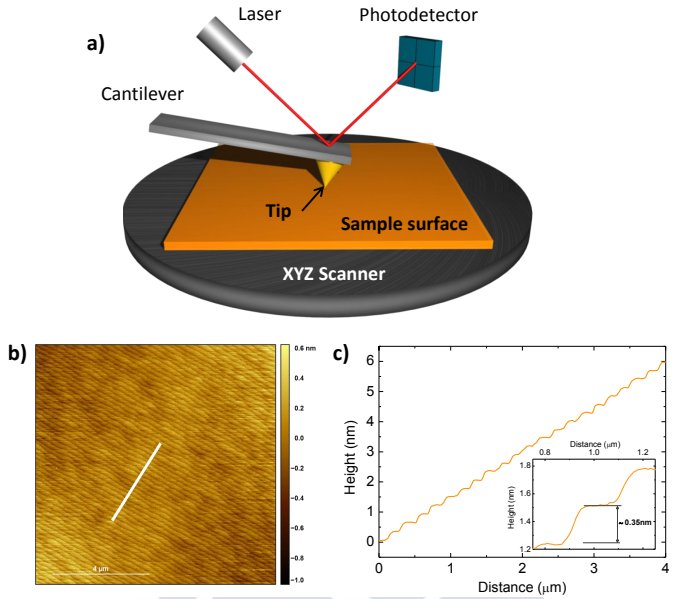

Figure 2.6: Atomic Force Microscopy. a) Scheme of AFM working operation, detailing the different elements of the system. b) An AFM topography image of the surface of $SrTiO_3$ thin film grown on (110) $DyScO_3$ substrate and c) the corresponding profile which shows the smooth terraces. The inset shows an enlargement of the height profile, in which the height difference between terraces is indicated.

Although other enhanced modes of AFM operation have been developed for specific purposes, all of them are based on three basic modes: non-contact, contact and tapping mode.

- **Contact mode**. It is the most common; the tip is in "close" contact with the sample surface and is dragged over it, keeping the deflection constant. The tip experiences a repulsive force, and both long- and short-range forces add to the image signal. In this static mode, the control parameters are the displacement and the constant force with which the cantilever pushes the sample surface (typically around tens of nN). Therefore, the choice of cantilever is crucial, it must be softer enough to prevent its breaking

and also the damage of the surface of the sample.

Under ambient conditions, most samples are covered by an adsorbed layer of water and nitrogen, which is 10-30 monolayers thick. When the tip scans the surface, a meniscus layer is formed. Additionally, many types of materials, including semiconductors and insulators, can trap electrostatic charge, which is dissipated and screened in liquid. This charge can increase the attractive forces between the tip and the sample surface, which can alter the sample surfaces and lead to an erroneous interpretation of the height profile.

- **Non-contact mode (NC-AFM)**. In order to avoid the problems associated to the presence of a meniscus, the scan of the surface can be performed in a non-contact mode. In this case, the tip scans the sample above the surface, without touching it, and uses the attractive inter-atomic forces (Van der Waals) between the tip and the sample to measure the surface topography. Due to the attractive forces from the sample being weaker compared to those in contact mode, the tip must vibrate close to its resonance frequency when it passes over a surface, and associate the changes in the cantilever's vibration to variations in height.

- **Tapping mode**. The tapping mode appears to overcome the operating problems of NC-AFM mode and other difficulties such as friction, adhesion or electrostatic forces. The operation of this mode is as follows: the tip slightly hits and lifts off from the sample surface on each oscillation, using high vibration frequency (50-500 kHz) and amplitude ($\sim$20 nm). Normally the selection of the optimal oscillation frequency is software-assisted and maintained constant at the lowest possible level. When the tip moves over a hill in the sample surface, the cantilever has less space to vibrate and the amplitude of oscillation decreases. In contrast, when the tip passes over a cavity, the cantilever amplitude increases.

2.3.1 Electrostatic Force Microscopy and Kelvin Probe Microscopy

The study of materials for electronic applications required the development of new AFM techniques, capable of mapping the electronic properties of materials. These AFM-based electronic techniques are mainly three: Electrostatic Force Microscopy (EFM), Kelvin Probe Force Microscopy (KPFM), and Piezoresponse Force Microscopy (PFM). Since only EFM and KPFM techniques have been used in this Thesis, this Section focuses on briefly explaining its main characteristics and differences.

- **EFM** is based on NC-AFM mode. A bias voltage is applied between the conductive tip and sample surface while the cantilever scans the surface of the sample (Fig. 2.7). The amplitude of the cantilever oscillation depends on the electrostatic force interaction between the AFM tip and the sample surface. The electrostatic forces are proportional to $1/r^2$, while Van der Waals forces are proportional to $1/r^6$. Therefore, Van der Waals forces are dominant when the tip-sample distance is short, but as the distance increases electrostatic forces become dominant.

  Normally, the image is taken using the two-pass method. In the first scan, the tip scans close to the surface where the Van der Waals forces are dominant for topography imaging. After that, the tip is lifted to reach the distance in which the electrostatic force is dominant, it is biased and scanned following the topography line acquired from the first scan, generating the EFM image.

  EFM collects the information about the electrostatic force between the dc biased conductive tip and the sample surface. A variation in this force results in a change of the cantilever resonant frequency, which is proportional to the force gradient:

$$\Delta\omega = \frac{\omega_0}{2k}\frac{dF(z)}{dz} \tag{2.12}$$

where k is the spring constant and w_0 is the resonance frequency of the cantilever. By adjusting the driving frequency w_p, the resonance is maintained. Then, the frequency shift Δw=w_p-w_0 is acquired as the EFM image.

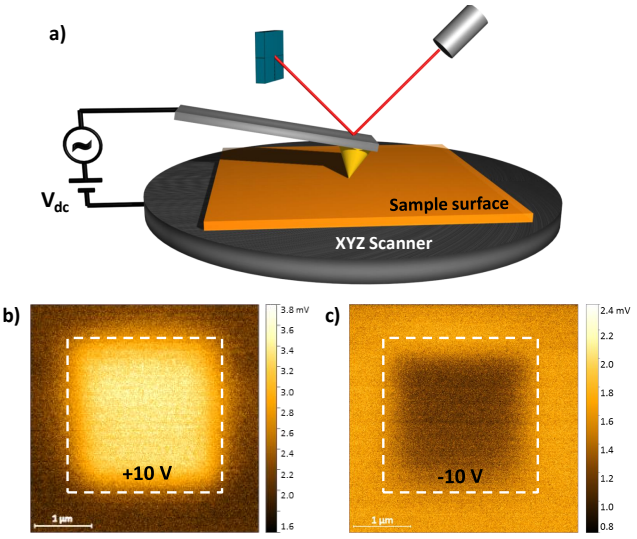

Figure 2.7: a) Scheme of the EFM method; the bias voltage is applied between the tip and the sample holder. b), c) Example of EFM images corresponding to a Nb:STO thin film grown on a (110) $GdScO_3$ substrate after recording the central square region marked with dashed lines with +10 V and -10 V, respectively.

- **KPFM**. The principal difference compared with EFM mode is that KPFM uses a compensation technique to allow quantitative measurements of the local surface potential (SP) (see Fig. 2.8), which can be related with the work function (WF) difference between the tip and sample. In this Thesis, EFM has been used in combination with the KPFM to avoid topographic artifacts when the spatial variation of the charge density in the films is determined.

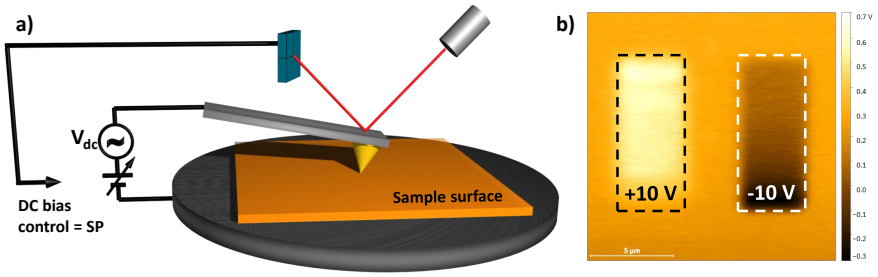

Figure 2.8: KPFM technique. DC bias is controlled by a feedback loop, which tries to nullify the measured force. The result is the surface potential of the sample with respect to that of the tip. b) Real KPFM image corresponding to a Nb:STO thin film grown on a (110) $DyScO_3$, in which a previous scan with -10 V and +10 V inside the marked zones was performed.

In the KPFM mode the cantilever is not driven mechanically when the image is acquired. Instead, the tip is biased directly using a sinusoidal signal with a *dc* offset. ΔV is the potential difference between V_{SP} and the voltage applied to the AFM tip (V_{tip}) as follows:

$$\Delta V = V_{tip} \pm V_{SP} = (V_{DC} \pm V_{SP}) + V_{AC} sin(\omega t) \qquad (2.13)$$

where V_{AC} is referred to the driving voltage. The electrostatic force between the tip and sample surface at potential V is given by:

$$F(z) = -\frac{1}{2}\frac{\partial C(z)}{\partial z}\Delta V^2 \qquad (2.14)$$

where C'(z) is the gradient of the capacitance between the tip and the sample, dependent on tip geometry, surface topography and tip-surface separation z.

The first harmonic of the force is expressed as follows:

$$F_{1w} = -\frac{\partial C(z)}{\partial z}(V_{DC} \pm V_{SP})V_{AC}sin(\omega t) \tag{2.15}$$

This term is nullified by supplying a bias feedback loop which continually adjusts the constant component of the tip bias (V_{DC}). The tip bias that cancels the electrostatic force is equal to the V_{SP}. Therefore, the final KPFM image is a 2D map of spatial variation of the SP, which is related to local differences in charge density distribution. This compensation technique attenuates all other responses from the measurement, losing all information outside the modulation frequency (e.g. the information provided by the second harmonic) [96–98].

2.4 Electrical transport measurements

The transport properties of the samples were measured using either the Van der Pauw method, or by patterning a conducting Hall bar on top of the thin films by optical lithography (see Fig. 2.9).

Hall bar configuration allows the measurement of multiple electric properties (resistivity, conventional and planar Hall effect, anisotropic magnetoresistance, etc), minimizing the leakage current and the undesired misalignment.

For the results presented in this Thesis, the length of the Hall bar channel is l = 650 μm and the width is ω = 100 μm. The fabrication process consists in 6 steps, combining standard photolithography and physical etching as is schematized in Fig. 2.9. At the beginning, the thin film covers the entire surface of the substrate. The first step is doing a lithography with a positive mask in order to protect the thin film under the desired Hall bar configuration (2.9 a) and b)). Once the Hall bar is covered by the photoresist, a wet acid or dry ion-etching is carried out, which removes the unwanted part of the thin film (2.9 c)). After that, a litt-off process is performed to eliminate the protective photoresist layer (2.9 d)). In the second step of lithography, a negative

mask is used, which covers only the channel region of the Hall bar, leaving the six pads (see 2.9 e)). Finally, 5nm of Cr and 50 nm of Pt are evaporated to create the ohmic contacts at the six contact pads. The electrical contacts are made by wire bonding with 30 μm Al wire (2.9 f).

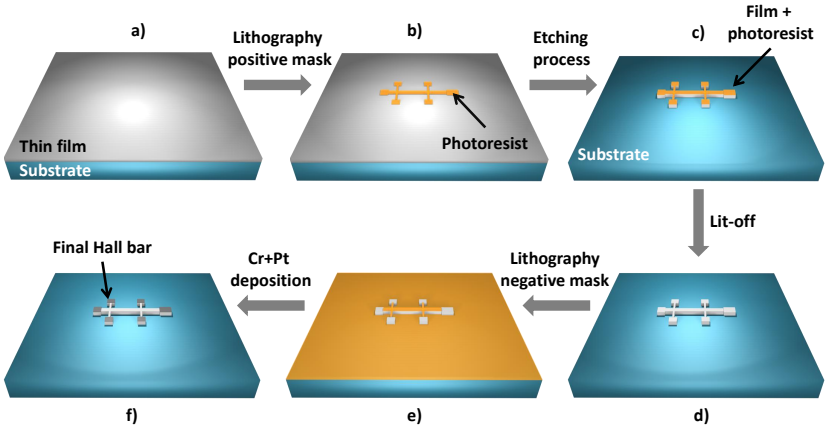

Figure 2.9: Scheme of the Hall bar fabrication. a) Thin film as-grown, b) lithography with positive mask, c) physical etching process, d) litt-off to remove the protective photoresist, e) second lithography step using a negative mask, and f) metal deposition on top of the six ends of the bar. Final Hall bar has 650 μm length and 100 μm width.

2.4.1 Electrical resistivity

Van der Pauw technique is a convenient method used to measure the electrical resistivity of uniform samples, such as thin films, because it does not require sample preparation [99]. The samples should have a flat shape and uniform thickness, without inhomogeneities and isotropic with respect to the electrical transport. For the measurements, four small ohmic contacts are placed at the corners of the film, as is depicted in Fig. 2.10 a). The area of the electrical contacts should be much smaller than the area of the surface of the sample and additionally, these must have symmetry at the boundaries of the sample to minimize errors.

While Hall bar configuration requires only one voltage reading, Van der Pauw geometry needs two. In practice, an electrical current is injected from one side of the sample (for instance, I_{12}) and the voltage is read at the opposite side (V_{34}). Consequently, the resistance can be determined using the Ohm's law. In our particular case, more accurate measurements were performed by repeating the same process through all four sides of the thin films, and then inverting the polarity of each measurement. Thus, an average resistance (R) is determined. In the case of square geometry using Van der Pauw measurement, the resistivity (ρ [($\Omega.cm$]) is given by:

$$\rho = \frac{\pi R t}{ln(2)} \tag{2.16}$$

where t is the thickness of thin film.

Similarly, for the measurement using the Hall bar configuration illustrated in Fig. 2.10 b), the current is injected between I_+ and I_- contacts and the voltage is read between D and E ones. Thus, using this configuration, ρ will be determined by the relation:

$$\rho = \frac{R t \omega}{L} \tag{2.17}$$

where ω and l are the width and length of the Hall bar, respectively.

2.4.2 Hall effect measurements

Hall effect is based on the physical principle of Lorentz force. When an electrical current is applied along a metal or semiconductor and perpendicularly to a magnetic field, the charge carriers inside the material experience a force acting normal to both directions, which changes their trajectories and produces a transverse voltage, the so-called Hall voltage (V_H) [100]. From this voltage, the charge carrier concentration (n) can be obtained as follows:

$$n = \frac{IB}{qtV_H} \tag{2.18}$$

Combining resistivity and charge carrier concentration, the mobility of charge carriers (μ) can be calculated using:

$$\mu = \frac{1}{\rho n e} \tag{2.19}$$

where e is the electron charge.

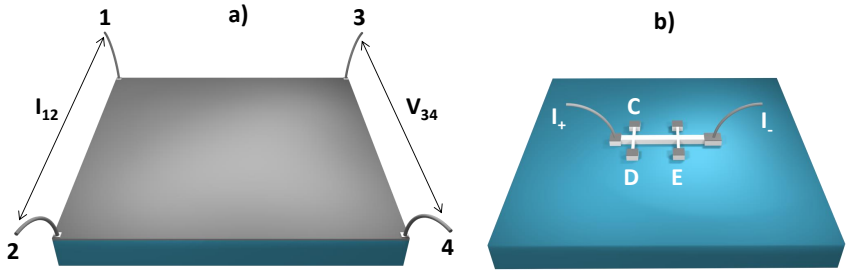

Figure 2.10: a) Sketch of Van der Pauw configuration for resistivity measurement in our samples. Indicating the four ohmic contacts placed at the corners of the sample. The current is injected between contacts 1 and 2 contacts, while the voltage is read in the opposite side from 3 and 4. b) Scheme of Hall bar configuration, in which is marked the current injection (I_+-I_-). The voltage is measured between D and E for electrical resistivity and between C and D for Hall measurements.

For the measurement of Hall effect using the Van der Pauw method, the electrical current is injected through contacts 1 and 4 and the voltage is measured between contacts 2 and 3. For each measurement, the voltage is measured for different values of current, maintaining the magnetic field constant. Additionally, two measurement are performed, either with positive and negative magnetic field. The same procedure is repeated for different values of magnetic field, in our case up to 1.2 T, with a step of 0.1 T (see Fig. 2.11). Two measurements are required, so that we repeat the same protocol by injecting the current (I_{23}) and reading the voltage (V_{14}) (see Fig. 2.10 a). Moreover, in order to cancel

the effect of magnetoresistance due to contact misalignment, the same protocol is done with ±B.

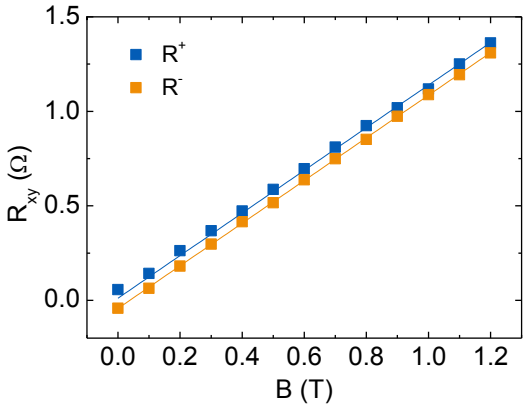

Figure 2.11: Twice measurements of Hall resistance (R_{xy}) for inverted magnetic field (B) using Van der Pauw configuration.

In Hall bar configuration, the measurement is performed in a single step, by injecting the electrical current between I_+ and I_- and measuring the voltage drops between C and D contacts. This measurement is repeated for different values of the magnetic field in a similar procedure to that measured by the Van der Pauw method.

2.4.3 Seebeck effect measurements

The Seebeck coefficient (S) is a material's property defined as the voltage induced in response to a temperature difference across the material. S depends on the carrier concentration, carrier effective mass, and temperature [101]. In bulk materials, it is normally measured by using a pair of fixed thermocouples, to determine the thermal gradient (ΔT) created by a resistor and at the same time, the thermoelectric voltage (ΔV) [102–104]. However, thermoelectric thin films are too thin to

be measured by this traditional method and therefore, several alternative ways have been developed in the literature since the appearance of these materials [105].

In this Thesis, we have followed a steady-state methodology previously development in the group [106], in which three Pt resistors deposited by optical lithography are used to create and measure the thermal gradient. One of the resistors (heater), which is electrically isolated from the film, heats up the sample by Joule effect when a current flows between its ends. The other two resistors act as local thermometers (T_1 and T_2), measuring the thermal gradient created in the film (see Fig. 2.12 a). They must be previously calibrated in the whole temperature range using a very slow temperature ramp, to assign a certain value of the resistance of each thermometer to the base temperature (T_{base}).

Furthermore, two additional contacts are necessary to obtain the thermoelectric voltage ($V_{Seebeck}$). During the measurement, a series of thermal gradients are generated and recorded at the same time that the Seebeck voltage (see Fig. 2.12 b). Each temperature gradient must be sufficiently stable across the sample before measuring electrical voltage. S can be determined from the linear relation between the temperature gradient and Seebeck voltage as follows:

$$S = \frac{\Delta V}{\Delta T} \tag{2.20}$$

where ΔV is the Seebeck voltage increment and ΔT is the small thermal gradient created in each case (see Fig. 2.12 c).

For Seebeck measurement in presence of a magnetic field, the homemade set-up illustrated in Fig. 2.12 a) has been implemented in a Superconducting Quantum Interference Device (SQUID) of Quantum Design, that allows the application of a magnetic field up to 9T.

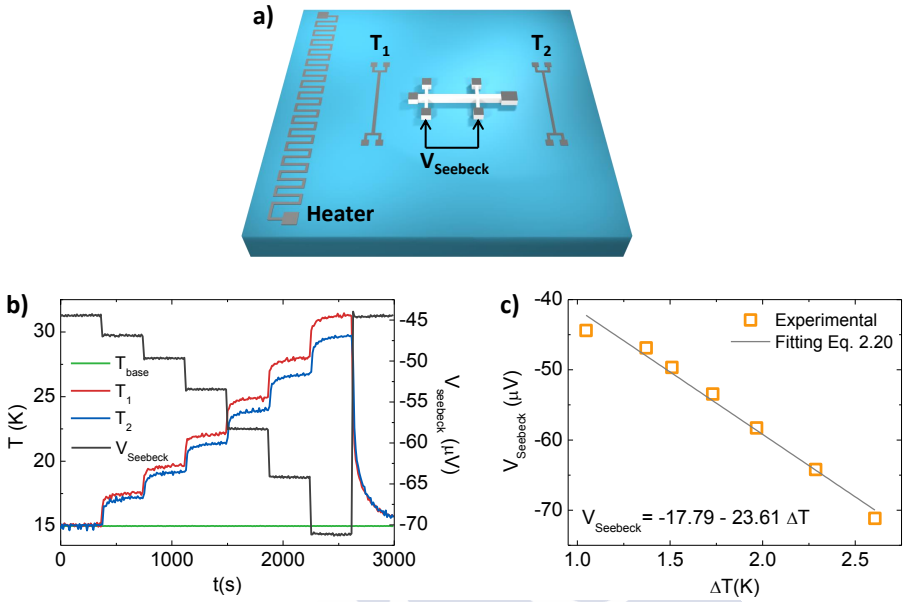

Figure 2.12: a) Seebeck configuration used in this Thesis. The heater uniformly heats up the thin film with the shape of hall bar, in which is measured the Seebeck voltage. Two thermometers are placed close the Hall bar to calibrate the temperature gradient created in the sample. b) Representation of the temperatures of the local thermometers (T_1 and T_2, red and blue lines, respectively), which measure the gradient created by the heater in the sample surface, and the base temperature over the time (T_{base}, green line). The representation also shows the values of $V_{Seebeck}$ over the same time scale, which are measured while the thermal gradient is created. c) Linear representation of the Seebeck voltage as a function of the thermal gradient. Solid grey line represents the fitting according to Eq. 2.20.

3. Computational Modelling

> Courage is like — it's a habitus, a habit, a virtue: you get it by courageous acts. It's like you learn to swim by swimming. You learn courage by encouraging.
>
> *Marie M. Daly, American biochemist. First Black American woman in the United States to earn a Ph.D. in Chemistry.*

Nowadays, computational modelling has become a powerful tool to gather information about the nature of materials and therefore, an essential part of modern materials science. It has helped the researchers to gain understanding and provides them a complementary view to explain a multitude of experimental findings and even new material properties. In this Chapter, it will present a brief general description on the historical development of Density Functional Theory (DFT) and the different attempts for dealing with the Schrödinger equation. The exchange functional and software packages that were used in the theoretical part of this PhD Thesis are also discussed. Lastly, we will describe how to calculate the spontaneous electrical polarization using DFT methods.

3.1 Density Functional Theory (DFT)

3.1.1 Brief history

More than half a century ago that Walter Kohn laid the foundations of the current DFT in his two famous papers in collaboration with P. Hohenberg [107] and L. J. Sham [108]. Since then, DFT is among the most popular and cited methods in physical sciences, twelve papers related to it are included among the 100 most cited of all time, 2 of them among the top 10.

It is routinely used to calculated the band structure of solids in physics and other multitude of properties, such as superconductivity, relativistic effects, magnetic properties, etc. DFT is based on a quite rigid conceptual framework but its versatility comes from the generality of its fundamental concepts and the flexibility to implement them.

The Schödinger equation describes how a physical system, meaning a group of particles with its positions and moments, will evolve over time, and it is assumed that the solution provides a full description of the system. Consequently, one could imagine that by solving this equation would get the microscopic properties that reflect all the relevant macroscopic properties of a material. Unfortunately, the Shrödinger equation gives exact solutions only for nuclei with one electron and, for the rest of materials will end up inevitably with an unmanageable equation. The wavefunction of a multi-electronic system is a Hilbert space vector, which depends on $3N$ variables. As soon as the number of electrons increases, it becomes incalculable and even impossible to store its value. DFT overcame these problems by following more rudimentary approaches and using the electronic density (a scalar dependent of 3 variables) as a fundamental variable, which determines all the properties of the ground state.

The starting point of the DFT method is the time-independent Schrödinger equation:

$$i\hbar\frac{d\Psi(r_i;t)}{dt} = \hat{H}\Psi(r_i;t) \tag{3.1}$$

where $\hat{H}$ is the Hamiltonian and $\Psi(r_i;t)$ is the many-body wavefunction, which is a function of position of electrons, spin of electrons and time in the system, and $\hbar$ is the reduced Planck's constant. Thus, the Hamiltonian for the system composed by electrons and nuclei can be written as

$$\begin{aligned}\hat{H} = &-\sum_{I}\frac{\hbar^2}{2M_I}\nabla_I^2+\frac{1}{2}\sum_{I\neq k}\frac{Z_I Z_J e^2}{\mid R_I - R_J \mid} - \frac{\hbar^2}{2m_e}\sum_{i}\nabla_i^2 \\ &+\frac{1}{2}\sum_{i\neq j}\frac{e^2}{\mid r_i - r_j \mid} - \sum_{i,I}\frac{Z_I e^2}{\mid r_i - R_I \mid}\end{aligned} \tag{3.2}$$

where m_e is the electron mass and M_I is nuclei mass with charge Z_I. The indices i, j run over the electrons and I, J run over nuclei. The first and third terms are the kinetic energy operator for nuclei and electrons, respectively. The second, fourth and fifth terms describe the Coulomb interaction between nuclei and other nuclei, electrons and other electrons, and nuclei and electrons, respectively. Due to the large number of coupled degrees of freedom involved in this equation, the task of obtaining the ground state for many-body systems becomes impossible in practice. Thus, there are several models and approaches that try to simplify the problem to make it manageable.

The first one is the so-called the Born-Oppenheimer or adiabatic approximation (1927) [109], which approximates the nuclei to be static in the Hamiltonian. This is justified due to the larger mass and lower velocity of the nuclei respect to electrons. Under this approximation, it is possible reformulate the Hamiltonian and decouple the dynamics of electrons and nuclei, vanishing the first term and reducing the second term to a constant. The Born-Oppenheimer approximation is the starting point for DFT methods, and although it simplifies the problem considerably, it is still too far to be solvable.

The next approach was developed by Thomas [110] and Fermi [111] in 1927. In the original Thomas-Fermi method, the kinetic energy of the electrons system is approximated as an explicit functional of the density, idealizing them as non-interacting electrons in a homoge-

neous gas with density equal to the local density at any given point, and neglecting exchange and correlation among electrons. This approach illustrates the way density functional theory works today, although it is a very crude approximation that cannot even predict the existence of chemical bond.

Another historically important strategy was the Hartree-Fock method [112], which is commonly used in Quantum Chemistry but it is not scaling appropriately for multi-electronic systems, as all the methods based on wavefunction solutions. It assumes that the multi-electron wavefunction can be approximated by a single Slater determinant, which is an antisymmetric combination of one wavefunction per electron (or spin-orbitals) taking into account the Pauli exclusion principle. Although the accuracy required at present in the description of nuclei, atoms and molecules cannot be reached by the Hartree-Fock method, it is still widely used as the starting point of several more elaborate methods, even for periodic systems.

3.1.2 Khon-Sham approach

In 1964, Hohenberg and Kohn [107] presented the statements which make the current DFT method possible. Basically, the idea is to substitute the initial many-body system by a non-interacting fictitious system where each electron is separately subjected to an effective potential but still sharing the electronic density of the global many-body problem. The two theorems were postulated as follows [113]:

Theorem 1: *For any system of interacting particles in an external potential $V_{ext}(\mathbf{r})$, the potential $V_{ext}(\mathbf{r})$ is determined uniquely, except for a constant, by the ground state particle density $n_0(\mathbf{r})$.*

Theorem 2: *A universal functional for the energy E[n] in terms of the density n($\mathbf{r}$) can be defined, valid for any external potential $V_{ext}(\mathbf{r})$. For any particular $V_{ext}(\mathbf{r})$, the exact ground state energy of the system is the global minimum value of this functional, and the density n($\mathbf{r}$) that minimizes the functional is the exact $n_0(\mathbf{r})$ ground state density.*

Therefore, these two theorems demonstrate that the ground state density can be determined from the minimization of an energy functional for any particular $V_{ext}(\mathbf{r})$, being able to extract all the properties of the system.

While Hohenberg-Kohn theorems proved that it is possible to calculate the properties of the system by using the ground state density, they did not provide a way of finding it. A route for that was the formulated by Kohn and Sham [108] almost exactly a year after the Hohenberg-Kohn theorems were published. The approach is to replace all electrons in the system with a system of non-interacting electrons, with the same electron density as the real system of interacting electrons, assuming that the ground state density of the original interacting system is equal to that of some chosen non-interacting system. To recover the many-body phenomena an exchange-correlation (XC) term is introduced, which contains all the missing many-particle effects.

The auxiliary independent-particle system is defined by the auxiliary Hamiltonian (H_{KS}):

$$\hat{H}_{KS} = -\frac{1}{2}\nabla^2 + V_{eff}(\vec{r}) \tag{3.3}$$

where V_{eff} is the effective potential. The ground state is calculated by solving the Schrödinger equation for a system with N independent electrons given by

$$\left(-\frac{1}{2}\nabla^2 + V_{eff}(\vec{r})\right)\varphi_i(\vec{r}) = \varepsilon_i\varphi_i(\vec{r}) \tag{3.4}$$

where ε_i is the orbital energy of the corresponding Kohn-Sham orbital $\varphi_i(\vec{r})$. These are the so-called Kohn-Sham equations, and from the N orbitals $\varphi_i(\vec{r})$ the density matrix of the auxiliary system can be constructed as follows

$$\rho(\vec{r}) = \sum_{i=1}^{N} \mid \varphi_i(\vec{r}) \mid^2 \tag{3.5}$$

This approach leads to a self-consistent solution of the orbitals and electron density. In this way, at the beginning a trial electron density is introduced into the equations in order to obtain the wave functions of a single electron, which is then reintroduced into the equation to calculate the electron density. If the electron density is the same as the density we started with, then the ground state electron density is found, and the process finishes. If not, the electron density must be updated, continuing the process until a self-consistent solution that satisfies the convergence criterion is reached, as is illustrated in Fig. 3.1.

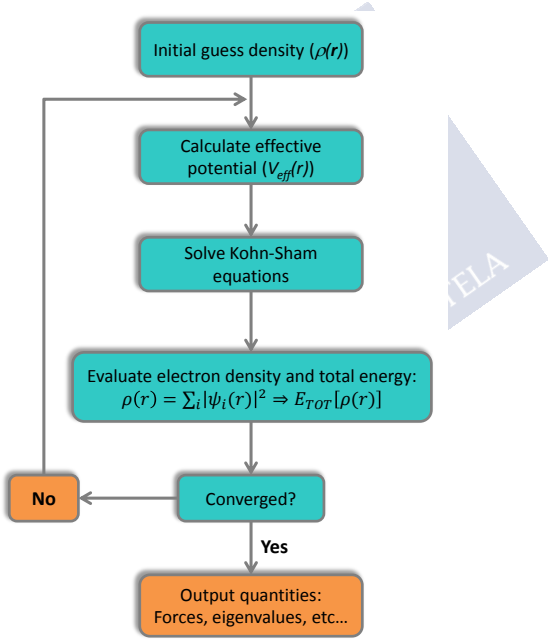

Figure 3.1: Flow chart of a typical DFT loop. First, an initial electron density is assumed, which is used to calculate the effective potential $V_{eff}(r)$. Then, Khom-Sham equations are solved, and subsequently it is evaluated $\rho(r)$ and E_{TOT}. If the convergence criterion is not satisfied, the loop starts over with the last $\rho(r)$. Once the convergence criterion is satisfied, the loop ends and all sorts of properties can be calculated based on the ground state electron density. Scheme adapted from ref. [113].

Kohn-Sham equations cannot be solved exactly unless the exchange-correlation functional is determined, for which unfortunately there is no established way to proceed. Therefore, except for the homogeneous free electron gas, it should be approximated.

3.2 The Exchange-Correlation Functional

The choice of an exchange-correlation functional is crucial but not a trivial issue, since there is not any universal DFT approach, and it depends strongly on the particular system and the property to be sought. The most commonly used functional approximations are Local Density Approximation (LDA) [108], Generalized Gradient Approximation (GGA) [114], Hubbard-corrected approximation (LDA+U or GGA+U) [115] and Hybrid Functional (HF) [116]. Focusing on this Thesis, we chose the Generalized Gradient Approximation (GGA) functional with the Perdew-Burke-Ernzerhof (PBE) [117] and PBEsol [118] approximations to perform DFT calculations, which will be briefly discussed below.

3.2.1 Generalized Gradient Approximation (GGA)

This exchange-correlation energy functional was proposed as a natural improvement beyond the LDA, which is only based on the local density at a given point. As its own name indicates, the GGA energy functional can be expanded in terms of the density and its gradients:

$$E_{XC}^{GGA}[\rho] = \int \epsilon_{XC}^{GGA}(\rho, \nabla_\rho)\rho(\vec{r})d\vec{r} \tag{3.6}$$

Compared to LDA, GGA significantly improves the lattice parameter determination and other properties related to crystal lattice constants of most transition metals systems and consequently, it is normally used to calculate their electronic structure. However, GGA tends to overcorrect LDA results in ionic crystals, in which LDA fits better to the experimental results.

A well-known problem is that both GGA and LDA usually underestimates the electronic band gap. One attempt to solve this issue is by introducing the Hubbard term (U) in a strongly correlated system, which adds the effect of Coulomb interaction between electrons into the localized orbitals. Another possibility is by using Hybrid functionals, in which fraction of the LDA or GGA exchange is replaced by a fraction of exact exchange energy functional. Although this approach considerably improves the band gap determination of the most semiconductor and insulator materials, its implementation is computationally expensive and not satisfactory in all cases.

Within the GGA approximation, there are several ways to incorporate the density gradient. One of those methods is the one proposed by Perdew-Burke-Ernzerhof [117], which is the most commonly used in Solid State calculations today due to its computational efficiency, numerical accuracy, and reliability. This is the main functional we have utilized in this Thesis, although in certain parts (especially in the calculations related to ferroelectricity and strain) the PBEsol functional [118] has also been used. The latter is a functional specifically proposed for solids, improving some disadvantages of the GGA-PBE but without requiring a lot of additional calculation time.

3.3 Wien2k and VASP Packages

There are several software packages which allow to perform electronic structure calculations of solids by DFT method. In this Thesis, we used Wien2k [119] and VASP (Vienna Ab initio Simulation Package) [120]. These are packages normally used to calculate quantum mechanical properties on periodic solids, and are very accurate for performing electronic calculations in crystals.

The two packages compute an approximate solution to the many-body Schrödinger equation, solving the Kohn-Sham equations within the DFT method. They are based on the augmented plane-wave method plus local orbitals (APW+lo) and projector augmented-wave (PAW), respectively. They include different exchange-correlation potentials such

as LDA and various GGA approximations (PBE, Perdew-Wang, PBEsol, Wu-Cohen,..).

- **APW+lo: Augmented plane-wave plus local orbitals.**

  APW method is a variational expansion approach which solves the equations of DFT by approximating solutions as a finite linear combination of basis functions. For such solutions, it is used the called muffin-tin approximation, which separates the unit cell into two parts: the muffin-tin spheres centered at the atomic sites and the remaining interstitial region (Fig. 3.2). Muffin-tin radii (R_{mt}) must be chosen carefully depending on the atomic size and the spheres can not overlap each other. Different basis are used in the two regions: linear combinations of atomic-like functions inside the spheres, and a plane wave expansion in the interstitial part. The main problem with the APW method is that the basis set is energy-dependent (within the muffin-tin spheres) and in addition, it turns out to be a slow and unpractical method.

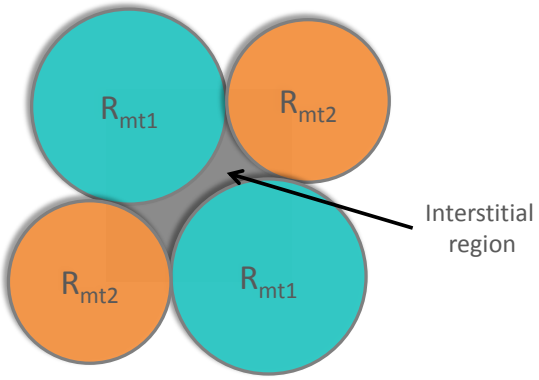

Figure 3.2: Representation of how the unit cell is divided in the muffin-tin approximation for a case with two atoms and different muffin-tin radii. It is also indicated the remaining interstitial region between the non-overlapping spheres.

To improve it, the APW+lo method (based on APW method) was

recently proposed by Sjöstedt [121]. By adding a local orbital in the basis set, this method makes the calculations faster and more efficient and above all, solves the energy-dependent problem of the APW method. The parameter $R_{mt}K_{max}$=*6-9* controls the size of the plane-wave basis, and is defined as the product of the plane-wave cut-off and the smallest muffin-tin radii [122, 123].

- **PAW: Projector augmented-wave.**

  Another method to model the core electrons makes use of pseudo-potentials. It is the so-called Projector Augmented-Wave (PAW), which expresses the single particle all-electron Kohn-Sham wave functions. PAW does this by writing the all-electron wave function as a sum of a few other functions, each of which can be expressed in a natural way in a basis. The pseudo-potential can be constructed to be weak and smooth, solving the Kohn-Sham equations in solids directly by using the Fourier space [124].

3.4 Electrical polarization

A workhorse throughout the history of electrical polarization has been how to define it in a crystalline solid. The problem was not solved until 25 years ago with the introduction of the so-called Modern Theory of Polarization by Vanderbilt and King-Smith [125, 126]. That was when researchers realized that one should work with changes in polarization instead of absolute values. The changes in polarization are well-defined and can also be compared with the experimental measurements.

There are two principal ways to estimate the spontaneous polarization in a crystalline solid: by using the Born Effective Charges, (Z^*) or by performing Berry Phase calculation, which entails more difficulty but provides more accurate results.

- **The Born effective charge (BEC)** is a tensorial quantity which evidences the coupling between lattice displacements and electrostatic fields. It differs from the nominal charge because it takes into account that when an ion of lattice is moved, the electrons

redistribute as well. In most materials, nominal and BEC have the same sign but different magnitudes and the difference can become large. Therefore, BEC is useful because it indicates how the ions respond to external electric fields and it can be determined theoretically using perturbation theory. BEC is defined through:

$$Z^*_{ij} = \frac{V}{e}\frac{\delta P_i}{\delta d_j} \tag{3.7}$$

where P_i is the change in the polarization induced by the periodic displacement d_j in the direction *i*, that in addition can also cause a polarization change in the direction *j*. The unit cell volume is denoted by *V*. By summing the polarization over the contributions of the displacements of all sub-lattices, the total polarization of the system can be obtained:

$$\delta P_i = \frac{e}{V} Z^*_{ij} \delta d_j \tag{3.8}$$

- **Berry phase method.** Another way to calculate the spontaneous polarization is by using the Berry phase formalism [127]. Basically, the Berry phase concept describes how if you add all the curvatures of an object and then deform it, the total curvature will remain the same. In the modern magnetism, this concept plays an important role to understand a broad range of phenomena such as the spin-orbit coupling, the quantum Hall effect or the anomalous Hall effect, and it is also useful to calculate the electrical polarization.

  The Berry phase approach consists of determining the change in polarization between a paraelectric initial structure (high symmetry) of reference, and a final ferroelectric structure (low symmetry), both with the same volume. An adiabatic path should be built between them, moving carefully the ionic positions along the polarization branch of the lattice. Various calculations are necessary following the deformation path between the high and low symmetry structures to ensure unequivocally that it remains on the same

branch during the adiabatic path (Fig. 3.3). To perform that, the system should be insulating, and with the same number of bands occupied at every point in k-space. The relaxed ionic positions and self-consistent charge density will be used as an input of the calculation [128].

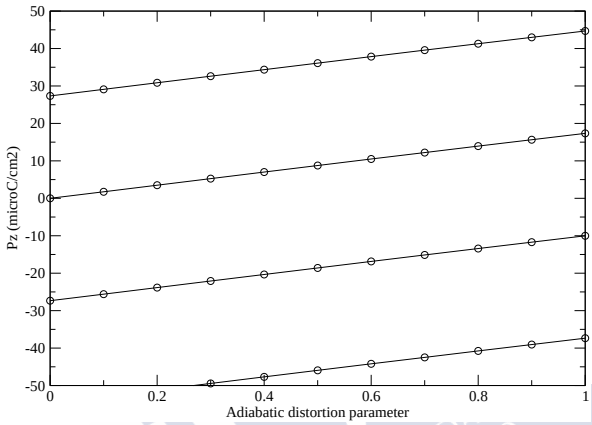

Figure 3.3: Calculated out-of-plane polarization as a function of the adiabatic distortion parameter for STO system starting from the high symmetry paraelectric structure, *I4mmm*, to the polar structure, *I4mm*. Unfilled dots are calculated points and solid lines are a guide to the eye, showing the continuous path along the branches of the polarization lattice.

4. Thermodynamics of oxygen vacancy formation

> I hadn't been aware that there were doors closed to me until I started knocking on them.
>
> *Gertrude B. Elion, American biochemist and pharmacologist, who won the Nobel prize in Physiology and Medicine in 1988.*

The mechanisms to accommodate the lattice mismatch between an epitaxial film and a substrate has drawn attention for more than 50 years [129–133] as it strongly influences the morphology and properties of the films [45, 134]. A common way to adapt the mismatch in ABO_3 perovskite-based heterostructures is primarily through changes in the lattice constants (volume effects or octahedral tilts) [135]. These mechanisms will be studied in depth in Chapter 6. However, point defect formation is also a likely strain-relaxation mechanism to be considered [50]. In this regard, the oxygen pressure during the deposition of metal oxides (for instance, by PLD technique) plays a major role in the mechanism that controls epitaxial relaxation [136].

For instance, to achieve fully oxygenated thin films, a high oxygen pressure is required. Nevertheless, some oxides need a low oxygen pressure during deposition to guarantee a low valence state of the cations. Thus, the competition between crystalline perfection and stoichiometry

is a usual problem when high quality heterostructures and superlattices are grown. As a consequence, one of the great challenges to be solved in PLD deposition is to achieve stoichiometric deposition for dissimilar material heterostructures. The solution could be the correct adjustment of the parameters in the subsequent post-annealing protocols (mainly temperature and oxygen pressure), ensuring the correct reoxygenation of the thin films and substrates as well [137].

Focusing on the particular case of STO, which is probably the most commonly used substrate in oxides growth, the formation and annihilation of anionic vacancies are relatively easy. Typical conditions of thin film deposition often involve high temperatures and low oxygen pressures, which greatly favour the reduction of STO [138–140]. Moreover, the extra charge releases by $V_{\ddot{O}}$ to non-bonding orbitals of the perovskite, produces a significant expansion of the unit cell and even helps to relax epitaxial stress for films grown under large strains [141]. Such vacancies produce both oxygen-ion conduction and electronic conduction [142]. Although ionic conductivity could be considered in potential applications such as electrolytes in solid-oxide fuel cells [143], oxygen-separation membranes or resistive switching devices [51], the incorporation of oxygen defects could be detrimental for some applications that require of dielectric insulating layers, for instance capacitors [67] or ferroelectric-based devices [83]. In this regard, it has become very important to understand the role of strain in the formation and stabilization of oxygen vacancies in this material [144, 145].

In this Chapter we will present a thermodynamic study of the process of oxygen vacancy formation in electron-doped STO thin films subjected to different degrees of epitaxial strain. For that, firstly we explain in detail the deposition conditions and the subsequent structural characterization of the films to ensure the correct growth (mainly the stoichiometry, epitaxial and good crystalline quality). Then, we will analyse the conditions to form and annihilate $V_{\ddot{O}}$, as well as the amount of charge contributed by each vacancy to the conduction band of STO. Finally, we will obtain the enthalpy of formation of $V_{\ddot{O}}$ as a function of both compressive and tensile strain.

4.1 Sample growth and characterization

4.1.1 Preparation of the substrates

The large number of substrates with different lattice parameters that are commercially available nowadays allows the study of the properties of thin films subjected to a large range of epitaxial strains. Taking advantage of this, we grew $SrTiO_3$ thin films on top of substrates with different lattice parameters and structures, changing the epitaxial stress in the interval from -2.91% ($LaAlO_3$) to +2.14% ($KTaO_3$). Fig. 4.1 shows the substrates used in this work and the corresponding pseudocubic lattice parameters, indicating the theoretical strain imposed on the films. The substrates highlighted in orange are those with orthorhombic distorted structure, the rest have cubic lattices, except LAO, which posses a rhombohedral distortion.

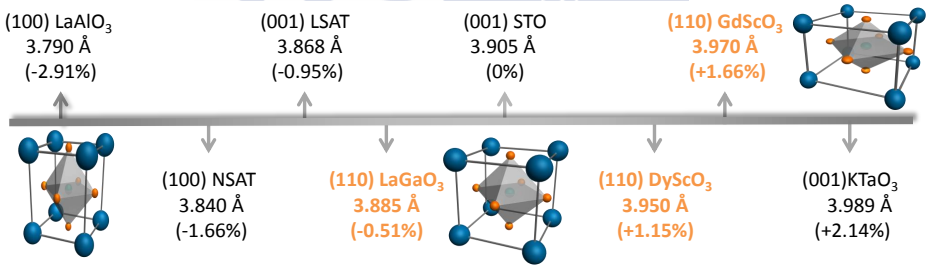

Figure 4.1: List of substrates used to grow Nb-doped STO thin films in this Thesis. The crystallographic orientation, pseudocubic lattice parameter (a_{pc}) and theoretical strain are indicated in each case. Theoretical strain is calculated respect to the lattice parameter of cubic $SrTiO_3$ ($a = b = c = 3.905$ Å), according to Eq. 2.3. Orthorhombic substrates are highlighted in orange.

As we briefly mentioned in Chapter 2, the preparation of substrate surfaces before the deposition is of vital importance in the subsequent properties of the films. A special effort has been invested in developing a method to treat cubic STO, the most widely used single-crystalline substrate.

In this Thesis, STO substrates were treated with deionized water at 70°C followed by an immersion in aqua regia (HCl-HNO_3 3:1) to eliminate the SrO layer. Finally, a thermal annealing at 1000°C is performed in air for 30 min, to recrystallize the surface [146]. The result is a flat and homogeneous TiO_2-terminated surface, as it can be seen in Fig. 4.2 b).

The other substrates only require a thermal treatment, varying the temperature and time in each case, to achieve flat and good crystalline surfaces. For instance, LSAT and NSAT substrates were treated at 1300°C during 3 hours while $LaAlO_3$, $LaGaO_3$ and $KTaO_3$ substrates were annealed the same time at 1000°C (Fig. 4.2 a). Rare-earth scandates ($DyScO_3$ (DSO) and $GdScO_3$ (GSO)) were subjected to thermal treatments at 1000°C during 2 hours to achieve the surface reconstruction (see Fig. 4.2 c)).

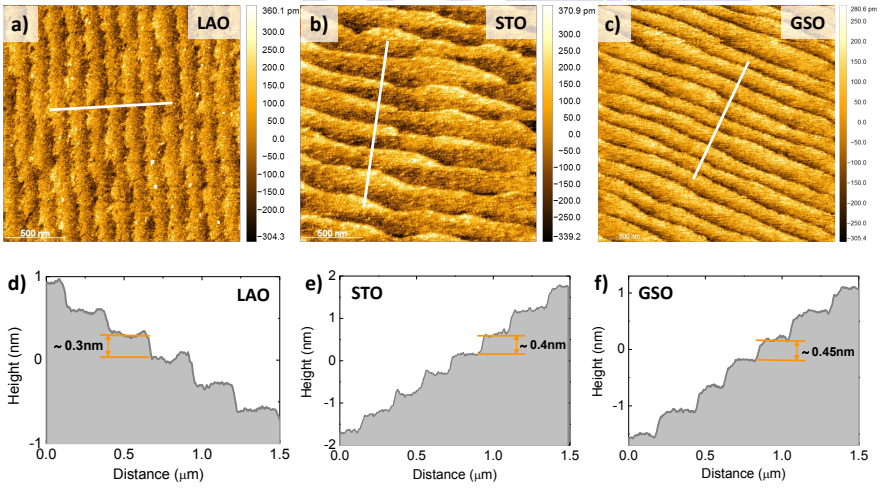

Figure 4.2: AFM topographic images (2 x 2 μm^2) of different substrates after being treated to achieve an atomically flat step terrace surface: a) LAO (100), b) STO (001) and GSO (110) substrates. The respective profiles along the white lines are shown below, d-f), showing in each case the height difference between the terraces.

After the treatments, the surface morphology of the films presents regular arrays of atomically flat terraces independently of the lattice parameter. The height difference between the terraces ranging from 0.30 to 0.45 nm, which is close to the dimensions of the unit cell of the substrates in each case (Fig. 4.2).

4.1.2 PLD deposition and structural characterization

The films were grown by PLD under previously optimized conditions [106]. The optimization required a very fine tuning of the laser energy, substrate temperature, and background oxygen pressure to minimize the presence of cationic vacancies and to achieve the correct stoichiometry of the films. An excimer KrF laser with a wavelength of λ=248 nm, laser fluence of $\approx$0.9 J/cm^2 and repetition rate of 5 Hz was used for the deposition. The substrate was kept at 800°C and an oxygen pressure of 100 mTorr was maintained during the deposition and subsequent cooling down at 5°C/min until room temperature.

Sets of films under different degrees of strain were deposited under the same deposition conditions, side-by-side in the same batch, to ensure similar thickness and stoichiometry of the films. The nominal Nb concentration was kept constant at $\approx 2\%$ to guarantee the electrical conductivity of the films.

Also the film thicknesses were maintained constant at $\approx$17-19 nm in most of the experiments, except of those performed in Chapter 7 in which we deposited a thicker film of $\approx$ 35 nm on LAO substrate, as will be discussed.

After the deposition, the structural properties of all the films were carefully verify through X-Ray reflectivity and diffraction. According to XRD around (002) Bragg peak, the films are perfectly *c-axis* oriented (Fig. 4.3). Furthermore, Laue oscillations can be seen, which demonstrate the existence of a crystalline coherence along the full thickness of the films irrespectively from the sign and magnitude of the lattice mismatch with the substrate.

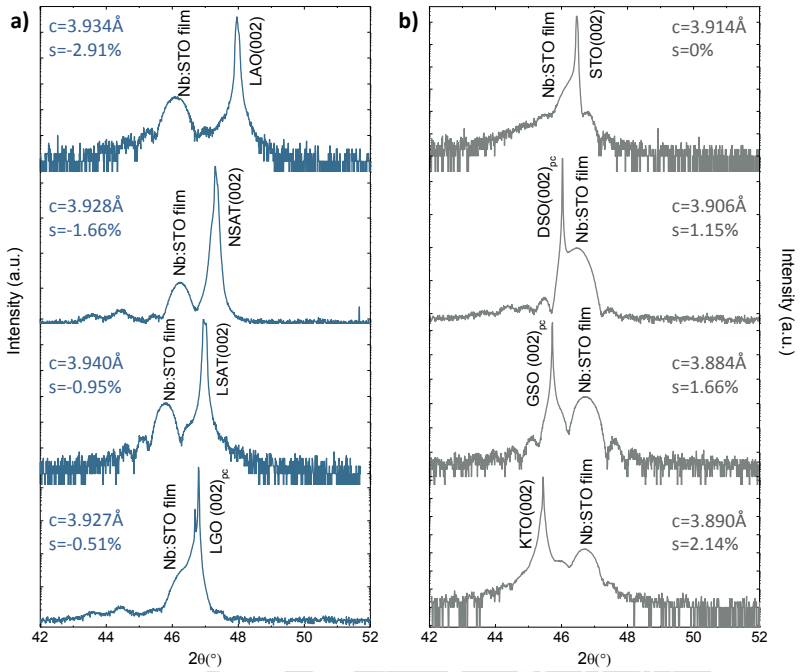

Figure 4.3: Summary of XRD measurements around the (002) pseudocubic-reflection for thin films grown under a) compressive strain and b) tensile strain. The *c-axis* value determined from the data is shown in each panel.

High-resolution RSM around the asymmetric $(103)_{pc}$ reflection indicate a good epitaxial matching of the films, except for those grown on LAO and NSAT substrates. These are the substrates that induce the highest degree of compressive strain and therefore, the films grow already partially relaxed as can be seen in the Fig. 4.4 a) and b). In the rest of the cases, the films are coherently and fully strained on the substrate, showing a perfect vertical alignment between the in-plane reciprocal lattice vectors of the films and the respective substrates independently of the structure of the substrate (cubic or orthorhombic). From these data, we can extract the values of the a and c lattice parameters in each case to compare them with the value obtained from the XRD measurements. Also the experimental strain can be determined in the case of

the relaxed films. Theoretical and experimental values obtained from the measurements are summarized in Table 4.1.

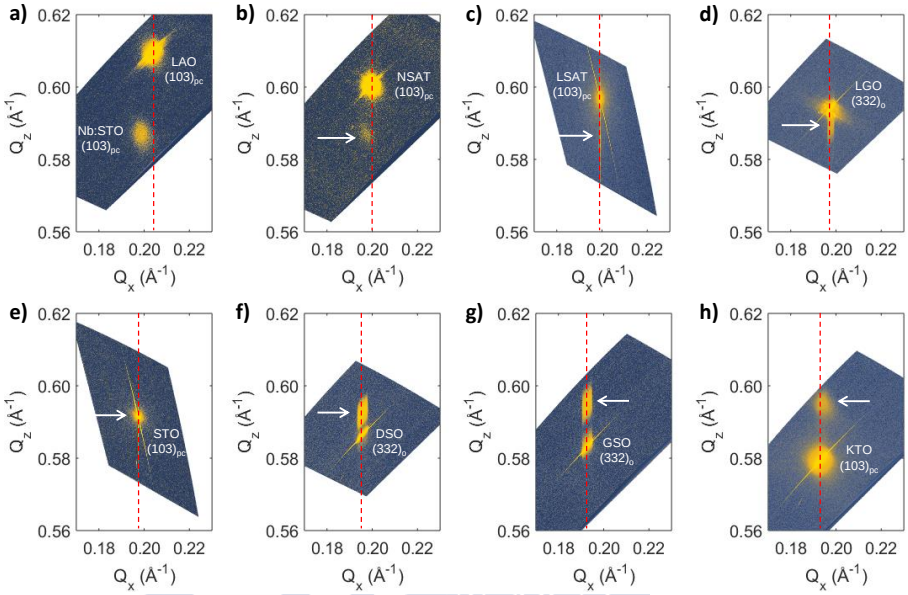

Figure 4.4: High-resolution RSM around $(103)_{pc}$ asymmetric reflection of STO deposited on (110) LAO (a), (100) NSAT (b), (001) LSAT (c), (001) STO (e) and (001) KTO (h) substrates, and $(332)_o$ reflection for (110) LGO (d), (110) DSO (f) and (110) GSO (g) substrates. The white arrow marks the reflection $(103)_{pc}$ for the film of Nb:STO in each case.

From these data, the change of volume with strain was calculated and shown in Fig. 4.5 for the as-grown Nb:STO films. By comparing the experimental results with the theoretical volume according to the Poisson's ratio of bulk STO (ν = 0.23 [90]), a progressive deviation from the theoretical prediction is appreciated as tensile strain increases. Nevertheless, experimental values are in agreement with the Poisson's ratio for compressive samples. Note that films grown on LAO and NSAT substrates are relaxed and therefore, its cell volume is much larger than expected in an epitaxial film. Despite this, the creation of defects occurs in such a way that the experimental volume and strain fit

Substrate	Acronym	a (Å)	b (Å)	c (Å)	a_{pc} (Å)	s (%)	a_{exp} (Å)	c_{exp} (Å)	s_{exp} (%)
$LaAlO_3$	LAO	3.790	3.790	3.790	3.790	-2.91	3.860	3.934	-1.15
$(NdAlO_3)_{0.39}$–$(SrAl_{0.5}Ta_{0.5}O_3)_{0.61}$	NSAT	3.840	3.840	3.840	3.840	-1.66	3.870	3.928	-0.90
$(LaAlO_3)_{0.29}$–$(SrAl_{0.5}Ta_{0.5}O_3)_{0.71}$	LSAT	3.890	3.890	3.890	3.890	-0.95	3.868	3.940	-0.95
$LaGaO_3$	LGO	5.523	5.491	7.773	3.885	-0.51	3.885	3.927	-0.51
$SrTiO_3$	STO	3.905	3.905	3.905	3.905	0	3.905	3.914	0
$DyScO_3$	DSO	5.540	5.710	7.890	3.950	+1.15	3.950	3.906	+1.15
$GdScO_3$	GSO	5.450	5.750	7.930	3.970	+1.66	3.970	3.884	+1.66
$KTaO_3$	KTO	3.989	9.989	3.989	3.989	+2.14	3.989	3.890	+2.15

Table 4.1: Summary of the principal structural parameters of all the substrates used in this Thesis. Bulk lattice parameters (a, b, c) and in-plane a_{pc} pseudocubic lattice parameters for each substrate. The nominal strain (s) imposed by each substrate in the STO thin films calculated according to Eq. 2.3 (a_f = 3.905 Å) is also indicated. Experimental data extracted from XRD and RSM are also shown (a_{exp}, c_{exp}, s_{exp}).

to the Poisson's ratio, meaning an elastic deformation of the material. To remove a cationic vacancy is favoured in this case due to volume arguments, as an attempt to contract the structure and to accommodate the large in-plane compressive strain.

Meanwhile, on the tensile side, the volume of the unit cell is slightly higher than expected from the Poisson's ratio (about $\approx 1\%$), suggesting the formation of oxygen vacancies as the predominant mechanism to relax the stress. This forces the reduction of Ti^{4+} to Ti^{3+} and leads to changes in ionic radius, which manifests macroscopically in the extra expansion of unit cell volume. These relaxation mechanisms based on a simple chemical expansion model are common in perovskite-type structures [45, 51, 147].

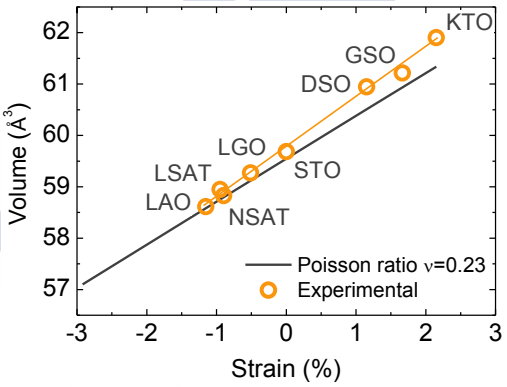

Figure 4.5: a) Evolution of the unit cell volume with experimental strain for all samples grown in this work (orange unfilled dots). The solid black line indicates the theoretical volume of the stoichiometric unit cell considering a Poisson's ratio of $\nu = 0.23$. Orange solid line is a guide to the eye.

Further insight into the microstructure and crystalline quality of the films can be provided by High Angle Annular Dark Field-Scanning Transmission Electron Microscopy (HAAD-STEM). This analysis was carried out in an FEI Titan 60-300 operated at 300kV and equipped with a high brightness Schottky field emission gun, a CETCOR probe aberration corrector form CEOS to achieve a spatial resolution better

than 1 Åin STEM mode, and a Gatan Imaging Filter 866 ERS for spectroscopic analysis. The specimens analysed correspond to lamellae extracted from the samples by focused ion beam (FIB) milling in a FEI Helios Nanolab 600 a 5 kV ion beam. The measurements were performed for two samples, one subjected to compressive (on LAO) and another to tensile stress (on DSO). The images are shown in Fig. 4.6 and corroborate the results obtained in RSM measurements. The sample grown on DSO presents an excellent crystalline quality and a sharp interface between the film and the substrate (Fig. 4.6 a). Nevertheless, the image of the film grown on LAO (Fig. 4.6 b), although it also shows a good crystalline quality along the film thickness, reveals the formation of defects close to the interface, which could be produced to accommodate the large epitaxial stress (s=-2.91%) imposed by the substrate.

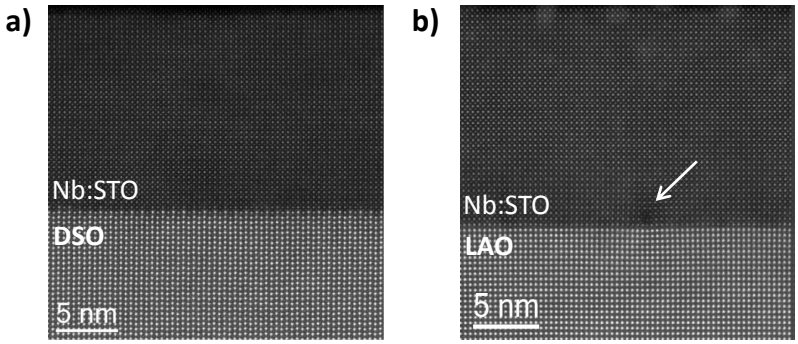

Figure 4.6: HAADF-STEM image of the as-grown Nb:STO thin films deposited on DSO (a) and LAO (e) substrates. White arrow indicates the presence of defects close to the interface in image b).

Furthermore, Geometrical Phase Analysis (GPA) can provide the evolution of the in-plane and out-of-plane lattice parameter along the film thickness, unlike X-ray diffraction which gives an average of the lattice parameter for the whole film. GPA analysis confirms that the film on DSO presents a homogeneous in-plane distortion throughout the films, whereas the film on LAO shows different in-plane distortion in the film than in the substrate (see Fig. 4.7).

In the case of the sample grown on a DSO substrate (Fig. 4.7 a, b), the profile of GPA analysis confirms that the out-of-plane negative distortion (ϵ_{zz}) in response to the tensile in-plane strain (ϵ_{xx}) is homogeneous throughout the films and in complete agreement with the coherent growth observed in RSM data . For example, for the STO film deposited on DSO, the c axis parameter of the film contracts $\approx$1.1% with respect to the substrate, while ϵ_{xx} does not exhibit any variation from the substrate to the film (Fig. 4.7 c). However, in the film deposited on LAO, both ϵ_{zz} and ϵ_{xx} show variation between the film and the substrate, demonstrating that the film was already partially relaxed (Fig. 4.7 d, e, f)).

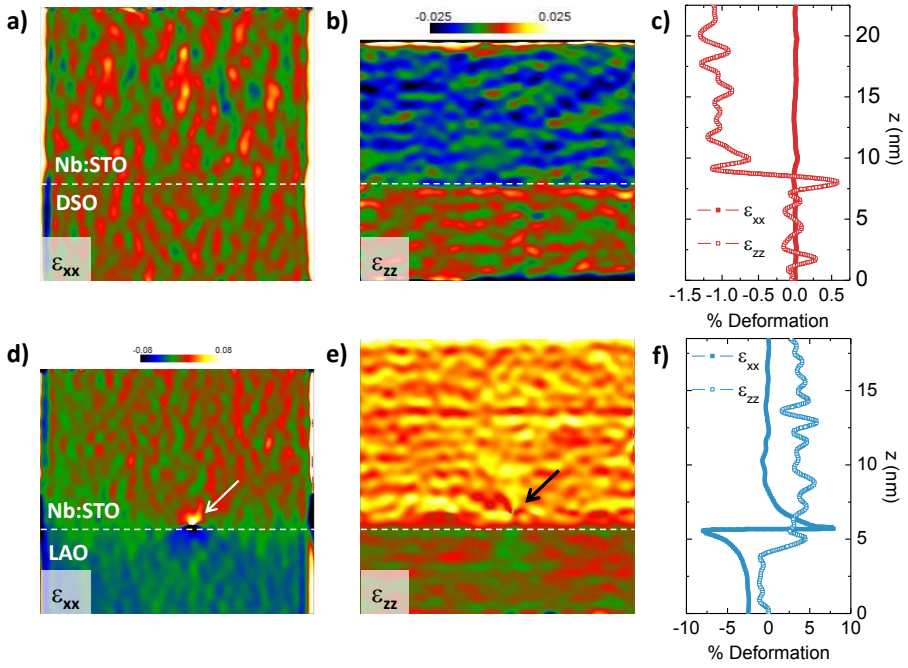

Figure 4.7: GPA analysis corresponds to Fig. 4.7, showing the in-plane (ϵ_{xx}) and out-of-plane (ϵ_{zz}) contraction/elongation along with the corresponding line profiles with respect to the substrate for the films grown on DSO (a,b, c) and on LAO (d, e, f), respectively.

As mentioned before, the formation of oxygen vacancies produces an increase of the unit cell volume due to the higher atomic radius of Ti^{3+} compared to Ti^{4+}, a higher vacancy concentration in reduced samples could affect the lattice parameters of the thin films. However, XRD measurements of the samples as-grown at 100 mTorr and after an annealing process at 1 x 10^{-6} Torr show the negligible effect on the lattice parameters, as can be seen for instance in one of the films grown on a LAO substrate (Fig. 4.8 c).

Therefore, we conclude that the main responsible for structural relaxation are the presence of strontium vacancies (V_{Sr}). This is consistent with the observations reported by other authors [106, 148, 149].

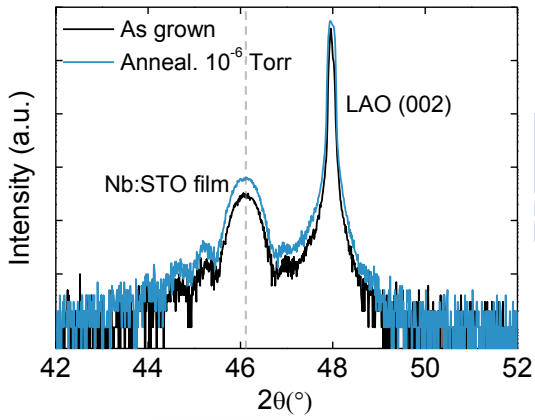

Figure 4.8: c) XRD θ-2θ scan of the sample grown on LAO as-grown at 100 mTorr and after the annealing process at 1×10^{-6} Torr, showing the negligible effect on the lattice parameters.

4.2 Creation and annihilation of oxygen vacancies

As discussed before, nominally undoped $SrTiO_3$ single crystals show a small concentration of acceptor impurities (Sr^{2+} vacancies) [144], which can trap the electrons donated by $V_{\ddot{O}}$ to the conduction band

of the oxide. To avoid this effect, we have doped the films with a 2% of Nb^{5+}. The doping introduces a small density of free electrons to compensate the unintentional presence of cationic vacancies. So that, even small changes in the $V_{\ddot{O}}$ concentration due to the different post-annealing processes will produce a measurable change in the conductivity and carrier concentration of the thin films.

During the PLD deposition at low oxygen pressures, the formation of oxygen vacancies in STO thin films occurs as Schottky defects. A V_{Sr} is formed at the same time as an oxygen vacancy to maintain the neutrality of charge:

$$Sr_{Sr}^{x} + O_{O}^{x} \leftrightharpoons V_{Sr} + V_{\ddot{O}} + SrO \tag{4.1}$$

Alternatively, $V_{\ddot{O}}$ can be introduced into a stoichiometric film by a post-annealing process in a reduced environment, in where the predominant mechanism is the loss of oxygen from the lattice to the atmosphere and a change in the oxidation of Ti:

$$SrTiO_3\ (s) \leftrightharpoons SrTiO_{3-x}(s) + \frac{x}{2}O_2(g)\uparrow \tag{4.2}$$

Although $V_{\ddot{O}}$ in e-doped STO are not stoichiometric vacancies, their concentration is not too large and the crystal can be still considered nearly stoichiometric. Assuming this, a simple mass action law can be applied to the reaction 4.2 and formulate the following equilibrium for the material at low oxygen pressures:

$$O^{2-} \leftrightharpoons \frac{1}{2}O_2 + V_{\ddot{O}} + 2e^{-} \tag{4.3}$$

where O^{2-} represents the concentration of oxygen ions at their STO lattice sites. Denoting the concentration of defects by angular brackets ('[]'), the equilibrium constant can be defined as:

$$K = \frac{[V_{\ddot{O}}]\, n_e^2 P_{O_2}^{1/2}}{\left[O_{\ddot{O}}^{x}\right]} \tag{4.4}$$

As the effect of acceptor vacancies (V_{Sr}) is compensated by Nb^{5+} donors originally present in the sample, the reduction reaction (Eq. 4.3) will produce a change in the carrier density that can be measured by Hall effect experiments.

Assuming that $[O_{\ddot{O}}^{x}]$ is constant and that each oxygen vacancy contributes two electrons to the conduction band of the material (n_e=2[$V_{\ddot{O}}$]), then the eq. 4.4 can be expressed as:

$$K = \frac{n_e^3}{2} P_{O_2}^{1/2} \tag{4.5}$$

Solving the Eq. 4.5, we obtain [150, 151]:

$$\log n_e \propto -\frac{1}{6} \log P_{O_2} \tag{4.6}$$

According to this equation, the logarithmic representation of the charge carrier concentration measured by Hall effect (after each post-annealing) versus the oxygen pressure should give a slope of -1/6 as long as oxygen vacancies are doubly ionized.

A controlled amount of oxygen vacancies was introduced in the films by post-annealing process at different temperatures (either 800°C or 600°C) and successive lower oxygen pressures in order to study the thermodynamics of an oxygen vacancy formation. In each post-annealing, the samples were left with the background oxygen pressure during 2 hours to reach equilibrium, and then rapidly quenched to room temperature at a cooling rate of $\approx$ 100°C/min approximately, to maintain the concentration of vacancies constant during the cooling.

The results are shown in Fig. 4.9 a) for samples annealed at either 800°C and 600°C. At high temperature, there is a very good agreement with the expectations for doubly ionized vacancies (solid orange line). Note that if there was an extrinsic source of oxygen vacancies, for example from acceptor impurities or an excess of TiO_2, Eq. 4.3 will not be the main source determining the concentration of vacancies, changing the slope of this representation. For instance, for single-ionized vacancies, the slope of the logarithmic representation of *n* versus PO_2

will change from 1/6 to 1/4. This behavior has been frequently seen by other authors at intermediate oxygen pressures [150]. In Fig. 4.9 a), the expected slope of -1/4 for singly ionized vacancies is also indicated, which clearly does not fit our experimental data independently of the temperature.

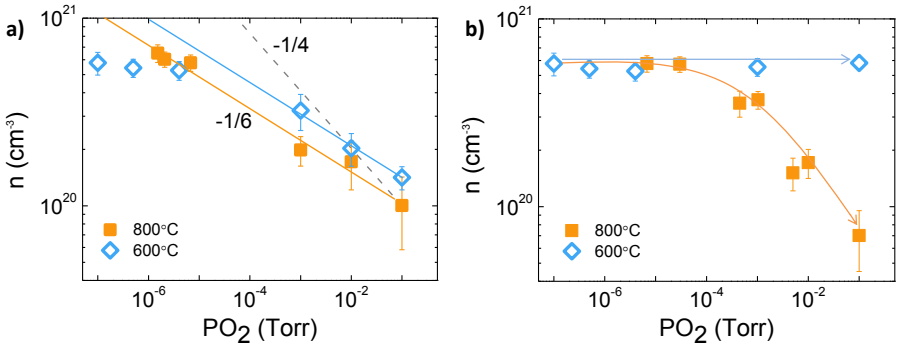

Figure 4.9: a) Variation of the charge carrier concentration as a function of the post-annealing oxygen pressure for the Nb:STO thin film on LSAT substrate. The same experiments were performed at 800°C (orange squares) and 600°C (open blue diamonds). Solid orange and blue lines represent the behaviour for the slope of -1/6 corresponding with doubly ionized oxygen vacancies (eq. 4.6), while black dashed line indicates the slope of -1/4 for single ionized vacancies. b) Re-oxygenation process of the previously reduced samples at higher oxygen pressure. Solid lines are guides to the eye.

At very low oxygen pressures ($< 10^{-6}$ Torr) the charge density saturates for both temperatures, indicating a limit in the $V_{\ddot{O}}$ formation by this procedure. This can occur for two principal reasons: the time to reach the thermodynamic equilibrium is insufficient or the combination between temperature and very low oxygen pressure is not enough to activate the formation of vacancies. The first option does not seem to be the cause, as two hours should be sufficient to reach thermal stability. Therefore, higher temperature or lower oxygen pressure are required to increase further the density of $V_{\ddot{O}}$.

The films were re-annealed at higher oxygen pressures, following

the same protocol as before. While the samples completely recover the initial state performing the re-oxygenation at 800°C and higher oxygen pressures (orange dots in Fig. 4.9 b)), the same does not occur when the samples are re-annealed at 600°C or lower temperatures. Actually, the charge carrier density remains constant at 600°C irrespectively of the oxygen pressure used. This result is of vital importance to understand the reduction/oxidation mechanism of STO, both in the form of thin film and single crystal (substrate). It demonstrates that the temperature is a critical factor in the creation/annihilation of $V_{\ddot{O}}$ in STO thin films and STO-based heterostructures in general. For instance, in the literature, LAO/STO interfaces are usually grow at low oxygen pressure and then, a subsequent re-annealing at high oxygen pressure and a temperature around 500°C is performed with the aim to fully reoxygenate the film [8, 26]. In view of our results, this temperature would not be enough to reoxygenate the samples completely.

Thus, the temperature is a fundamental factor in the synthesis and post-annealing protocols, and therefore it should be considered carefully when understanding their effects in terms of oxygen stoichiometry in complex oxides in general.

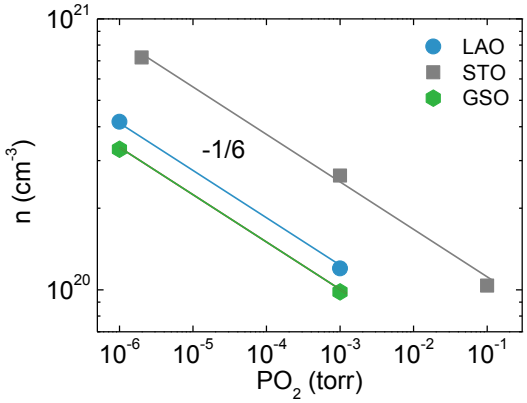

Figure 4.10: a) Variation of the charge carrier density for samples grown on different substrates (LAO, STO and DSO) and annealed at 800°C under low oxygen pressures.

Although the previous thermodynamic analysis was shown using the Nb:STO thin film grown on LSAT substrate, similar experiments were carried out in the other samples with different degrees of strain. As it is illustrated in the Fig. 4.10 a), a slope with value -1/6 was determined irrespectively of the substrate, indicating that $V_{\ddot{O}}$ are doubly ionized in Nb:STO thin films independently of the applied strain.

4.3 Enthalpy of formation of oxygen vacancies

Another important parameter to understand the formation of oxygen vacancies in complex oxides is the energetic cost of creating a vacancy, i.e. the enthalpy of formation (ΔH). Given that STO is one of the most used substrates in the growth of oxides and the strain could be a key parameter for controlling the formation and annihilation of vacancies, it is surprising that the dependence of ΔH has not already been determined experimentally. Theoretical calculations of ΔH dependence with strain have been reported, but there are not many experimental studies performed in this regard.

To gain insight about it, the same mass action law used above can be taken as starting point (Eq. 4.3). This thermodynamic equilibrium constant is related to the Gibbs free energy (ΔG) of the crystal, which in turn depends on ΔH and entropy (ΔS) of formation of oxygen vacancies as follows:

$$\Delta G = \Delta H - T\Delta S \tag{4.7}$$

Then, the equilibrium constant for Eq. 4.3 can be expressed as:

$$K = K_0 e^{-\Delta H/k_B T} \tag{4.8}$$

where k_B represents the Boltzmann constant and K_0 is a constant. Here we assumed that ΔS is only related to the increasing possibilities

of configurational arrangements, which could be supposed as temperature independent (only depends on the number of vacancies to sites). Then ΔH can be connected with the carrier density using equation (4.5), leading to:

$$\frac{n^3}{2} P_{O_2}^{1/2} = K_0 e^{-\Delta H/k_B T} \tag{4.9}$$

and therefore, *n* is given by:

$$\log n = K_0' - \frac{1}{6} \log P_{O_2} - \frac{\Delta H}{3\kappa T} \tag{4.10}$$

Then, if we consider the equation at constant pressure:

$$\log n = K_0'' - \frac{\Delta H}{3\kappa T} \tag{4.11}$$

The formation enthalpy of an oxygen vacancy can be determined from the slope of an isobaric plot of log n versus the inverse of the annealing temperature.

The approach in this case is to perform different annealing processes at constant oxygen pressure and increasing temperatures for all the samples under different degrees of strain. The results are shown in Fig. 4.11 a) for three films, grown on LSAT (s(%)=-0.95)), STO (s(%)=0.0) and DSO (s(%)=+1.15).

The fits are very good, with a linear dependence showing the validity of the approximations to reach equation 4.11. The value of ΔH determined for the unstrained sample is ≈0.51 eV, and decreases about 23% for both tensile and compressive strain. This indicates a very similar effect on the reduction of the formation enthalpy of $V_{\ddot{O}}$ in e-doped STO thin films for both compressive and tensile epitaxial stress, suggesting a common mechanism independently of the sign of strain.

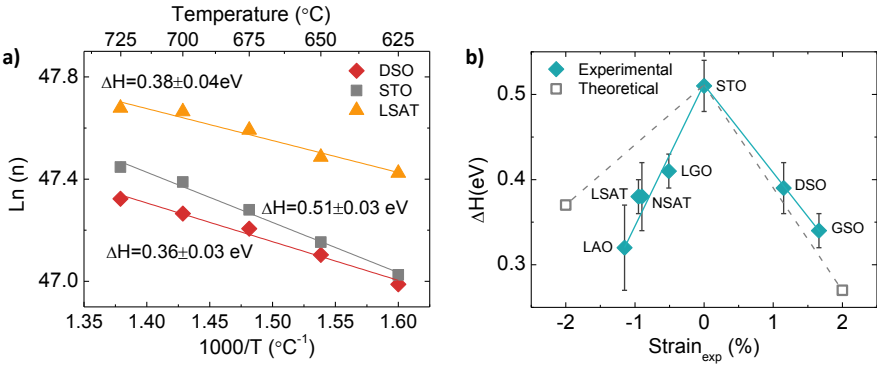

Figure 4.11: a) Logarithm of charge carrier concentration as a function of annealing temperature at fixed oxygen pressure (1 mTorr) for the samples grown on DSO, STO and LSAT substrates. b) Formation enthalpy of oxygen vacancies depending on the experimental strain. Open squares are the theoretical points according to reference [152].

Our results are completely in agreement with the ab-initio calculations performed by Choi *et al.* [152] (see Fig. 4.11 b), which pointed to a decrease of the band-gap energy when the magnitude of strain increases (independently of its sign) as the main responsible of this behaviour. These authors also affirm that oxygen vacancies are preferentially formed at the region where strain accumulates (interfaces and grain boundaries). Similarly, Berger *et al.* [141] also determined that biaxial strain could narrow the STO band gap significantly. Therefore, the observations of Fig. 4.11 support the scenario of the band gap reduction by means of strain proposed by several authors.

On the other hand, some reports support a lowering of the $V_{\ddot{O}}$ formation energy under tensile strain in other perovskite oxides, such as $CaMnO_3$ [45, 153], $PbTiO_3$ [132], $BaTiO_3$ [154] or $SrCoO_{3-\delta}$ [51] due to chemical expansion effect. However, the same chemical expansion mechanism should in principle disfavour anionic vacancy formation under compressive stress. In this case, several calculations have been published in the last few years, but the results are diverse for different oxides [147]: in $CaMnO_3$, the calculated effect of a moderate compressive stress is almost negligible [45,153], while a considerable increase of $V_{\ddot{O}}$ formation is observed in $PbTiO_3$ [132], $BaTiO_3$ [154] or $SrCoO_{3-\delta}$ [51].

4.4 Summary

It has been shown in this Chapter that high quality strained Nb:STO thin films can be achieved by Pulsed Laser Deposition irrespectively of the applied degree of strain, either positive and negative. Furthermore, the previous optimization of PLD deposition conditions resulted in nearly stoichiometric films with a minimized concentration of defects, which are in good agreement with the elastic deformation predicted by the Poisson's ratio.

The thermodynamics of oxygen vacancy formation have been studied, yielding that each oxygen vacancy donates two electrons to the STO conduction band, independently of the sign and the degree of strain. Moreover, the conditions used in the post-annealing protocols to modify the oxygen vacancy concentration in the thin films have shown that the temperature is a critical parameter in the subsequent formation and annihilation of $V_{\ddot{O}}$. This reveals that the synthesis and post-annealing protocols should be carefully selected to achieve fully oxygen stoichiometric films not only in the case of STO but, more generally, in the growth of oxide heterostructures.

Lastly, the formation enthalpy of oxygen vacancies in the films was determined depending upon the strain using a simple mass action law analysis. Either compressive and tensile strain produce a decrease in the formation energy, which points out for a common mechanism probably related with a reduction in the band gap of the films. This result is completely consistent with the calculations reported by Choi *et al* [152].

5. Controlled movement of oxygen vacancies

> Science, for me, gives a partial explanation for life. In so far as it goes, it is based on fact, experience and experiment.
>
> *Rosalind Franklin, English Chemist who contributed to the discovery of the DNA structure.*

The ability to manipulate the concentration of anions rather than metal cations in complex oxides can facilitate creating new functionalities in classical materials. For instance, the design of ionic-based memories has attracted a lot of interest in recent years [155, 156], especially those based on resistive switching mechanism, in which redox reactions and nano-ionic transport processes play a key role [157]. Consequently, the possibility to control at will not only the amount of oxygen vacancies, but also their distribution and movement inside the material, is essential for the design of new ionic-based devices. However, the difficulty in activating oxygen at reduced temperatures hinders the deliberate control of the vacancies.

Any substantial change in the concentration of anions produces a change in the stoichiometry, which in turn must be compensated by a variation in the valence of the cation sublattice. In many cases, this is reflected in a variation of the electronic conductivity, which could be

the basis for the resistive switching mechanism. The memories based on this mechanism can switch between at least two different resistance states, one of high resistance (HRS) and other of low resistance (LRS). The two different states could be induced by an external stimulus, for instance an external electric field, whose polarity controls the reduction or oxidation of the cation [158].

Flexoelectricity is another property of certain materials which can provide an alternative strategy to control its functionality. It is related with the coupling between polarization and strain gradient. Catalan et $al.$ [159] demonstrated that the stress gradient generated by an AFM tip can mechanically switch the polarization at the nanoscale in a $BaTiO_3$ films. In a similar approach, Sharma et $al.$ [77] were able to modulate the electrical conductivity of the 2D electron at the $LaAlO_3/SrTiO_3$ interface, opening a door towards mechanically operated transistors. An more recently, also Kalinin et al. [160] discussed the electrical and mechanical manipulation of the local $V_{\ddot{O}}$ distribution in unstrained STO thin films using a biased AFM tip.

In view of the results reported previously, STO is a promising candidate for this type of applications due to the possibility to easily tune the oxygen content and the migration of the vacancies within the material, being able to define even multi-stable states. For this reason, it is important to gain a deep understanding of the oxygen vacancy diffusion under external stimuli and also explore the possibility to tune it through strain-engineering. Furthermore, the study of diffusion is not only useful for ReRAM memories, but also for extending it to other types of technologies, such as Li-ion batteries [161], oxygen gas sensors [162] or photovoltaics [163].

As we have demonstrated in the previous Chapter, the concentration of $V_{\ddot{O}}$ can be easily changed in the thin films. The next challenge should be the control of the local distribution of these vacancies within the material using an external stimulus. Therefore, this Chapter will be focussed on the manipulation of oxygen vacancies in Nb:STO thin films using an external electric field produced by a biased AFM tip. We will determine the mobility and the diffusion coefficient of the vacancies at room temperature as a function of the degree of epitaxial strain. After-

wards, the possibility to use the Nb:STO thin films on future resistive switching memories (ReRAM) will be addressed, examining the main control parameters in the production and stabilization of these devices, such as tip bias, pulse time, temperature and reversibility.

5.1 KPFM versus EFM

The thin films were characterized combining Electrostatic Force Microscopy (EFM), and Kelvin Probe Force Microscopy (KPFM). KPFM often shows artifacts in the measurement due to its high sensitivity to the tip-sample distance and the presence of surface charges [97]. EFM does not depend so critically as KPFM on the tip-sample distance; therefore, it is more reliable in experiments that require measuring over long times, in which a small variation of the tip-sample distance can produce a long variation on the measured value of the surface potential (SP).

The determination of the absolute value of the surface potential by KPFM is a difficult issue. It is necessary to know the work function of the AFM tip, for which a calibration of the tip in a sample with a well-known work function is required [164]. This analysis is delicate and far from being the main objective of this Chapter of the Thesis. Accordingly, here we only perform a semi-quantitative analysis of the results, comparing relative SP differences between regions of the samples, or temporal variations of the EFM or KPFM signals.

The experiments were performed independently using two different AFM setups: a Park Systems NX10, and a Keysight 5500. Furthermore, in order to suppress possible effects derived from charge injection [165] (formation of protons/hydroxyl radicals [166] or electrochemical processes [167]), the measurements were carried out under ambient and low humidity conditions (6-7% RH), for comparison. For the electrical record of the samples a Pt/Ir-coated metallic tip with force constant of 3 N/m was used in KPFM and EFM modes. While KPFM is performed in single scan using tapping mode to acquire the topography, the record was performed in contact mode to ensure a continuous electrical contact between the tip and the sample (contact force = 90 nN). A single-pass

out of resonance KPFM was employed, speeding up our data acquisition and avoiding crosstalk between first and second resonance mode. Moreover, to minimize artifacts and offsets from the measurement conditions, all measurements were performed with the exact same type of probe, AC bias magnitude, frequency, tip-sample distance, and scanning/recording rate for KPFM/EFM and topography acquisition.

5.2 Mobility of vacancies under an external electric field

The thin films used in this Chapter are the ones characterized at the beginning of Chapter 4. Before the experiments, the surface topography of the samples must be carefully examined to verify the correct growth of the films, as a rough surface could determine very much the oxygen exchange with the atmosphere and the diffusion of the vacancies.

Figure 5.1 shows the results for two of the films grown on STO (0% strain) (a) and GSO (≈1.66%) (b) and the corresponding profiles (c,d). The line scan of the topography exhibits smooth surfaces and regular terraces with step height of ≈0.2 nm, consistent with a layer-by-layer growth, which reproduces the single-terminated surface of the substrates. These results demonstrate that the films present similar surface morphology independently of the sign of strain.

The electric-field-dependent vacancy mobility was carefully investigated as a function of strain in this Section. This important parameter gives an idea of how difficult it is to move an oxygen vacancy at room temperature in $SrTiO_3$. The mobility is also an important parameter in many applications, like resistive switching devices, in which it is crucial to determine the threshold voltage necessary to drag $V_{\ddot{O}}$ across the thin film.

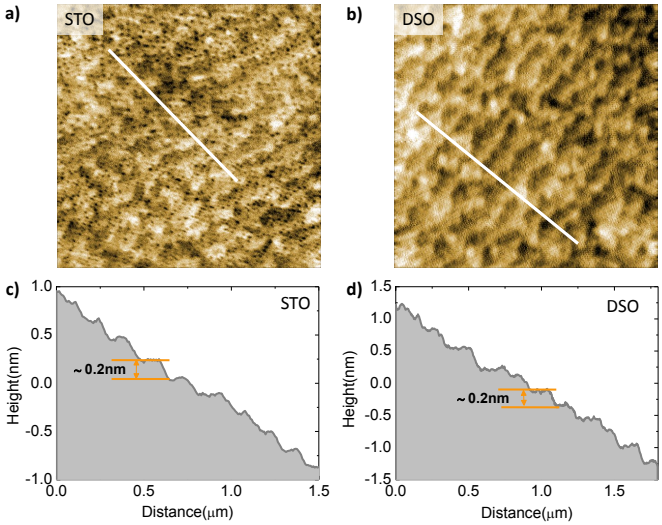

Figure 5.1: AFM images of the surface topography for Nb:STO thin films grown on STO (a) and DSO (b) substrates. The respective profiles along the white lines are represented below (c,d).

In order to quantify the effect of epitaxial strain on the $V_{\ddot{O}}$ mobility, a region of the surface of each sample was first poled with negative/positive AFM tip bias in contact mode, and then the same area was mapped by KPFM scanning at zero DC bias. An scheme of this approach is depicted in Fig. 5.2 a, b). Given the nanoscale dimensions of the tip radius (<25 nm), the electric field generated by the AFM tip bias (∼6 MV/m) is highly localized and it is sufficiently strong to modify the initial homogeneous distribution of positively charged $V_{\ddot{O}}$ of the thin films.

A negative (positive) tip bias attracts (repeals) the positively charged oxygen vacancies, increasing (decreasing) the local work function. As a consequence the SP is lower (higher) compared with the average background potential of the sample. Then, depending on the electric field direction, the accumulation (depletion) of $V_{\ddot{O}}$ will produce a localized decrease (increase) of the local SP [168]. A schematic illustration of the electric field direction depending on the tip bias, and the corresponding

movement of the oxygen vacancies away/near of the sample surface can be seen in Fig. 5.2 c, d).

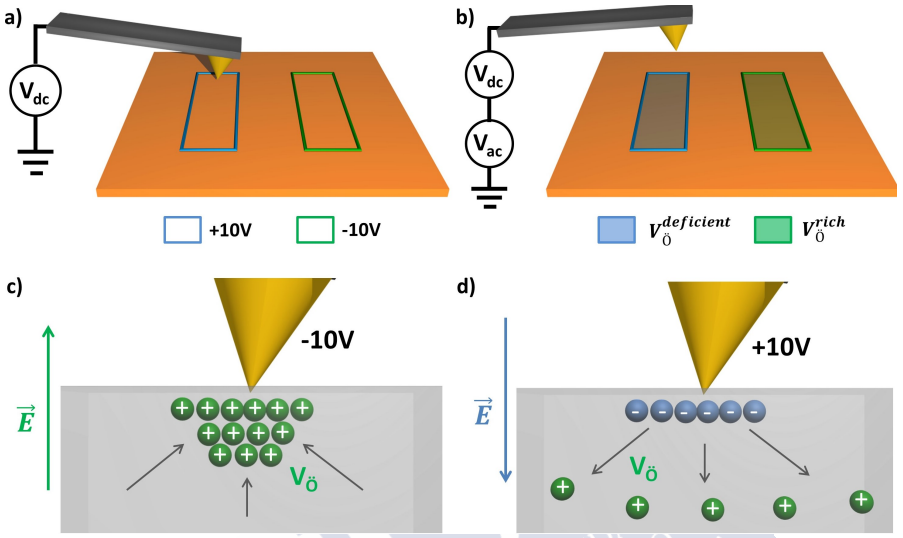

Figure 5.2: Scheme of the approach followed in this Section to study the room temperature diffusion of $V_{Ö}$ in STO. a) A negative/positive voltage is applied to the sample surface, b) generating depletion/accumulation regions of oxygen vacancies. c, d) Detailed sketches specifying the direction of the electric field and the movement of $V_{Ö}$ depending on the sign of the applied voltage.

Following the procedure explained above, four samples with different degrees of strain were recorded with positive and negative voltages ($\pm$10 V). The enriched or depleted zones produce a clear contrast in the KPFM signal independently of the sample (Fig. 5.3). From these results, we are able to compare the relative change of the surface potential between the two well-differentiated areas. This difference expressed in percentage with respect to the film grown on STO is denoted as ΔSP, and its strain-dependence can be seen in Fig. 5.4 a). ΔSP varies substantially with strain, increasing up to $\approx$40% for the most stressed films, either compressive (on LSAT) or tensile (GSO), with respect to the unstrained film. Therefore, epitaxial strain influences very much the $V_{Ö}$

mobility, being 40-50% easier to drag or repel the vacancies in the most stressed films. It is important to remark that these experiments provide information about the drift mobility, i.e. the movement of oxygen vacancies across the film exclusively under the influence of an electric field. This is not the free diffusion of $V_{\ddot{O}}$, which must be obtained from measurements in absence of an applied tip bias, as will be done in the next Section.

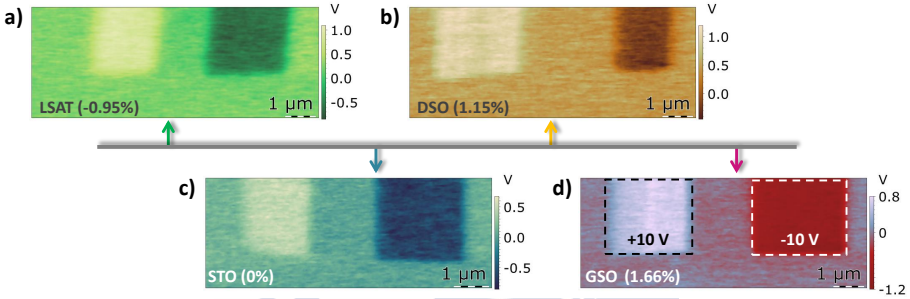

Figure 5.3: SP characterization for the thin films grown on LSAT a), DSO b), STO c) and GSO d). In image d), the voltages applied on the surfaces of the samples are indicated. The degree of strain in each film is also shown.

It is worth mentioning that significant differences in the SP background of the unpolarized regions are evident in Fig. 5.3, which depend on the magnitude of the strain. This can be related to a different initial concentration of $V_{\ddot{O}}$ in the as-grown films, also reflected in the different initial electrical conductivity of the samples [169]. All the as-grown films present very large electrical resistance, being only possible to determine the carrier density for the films on LSAT, LGO and STO. In order to compare the charge density with respect to the degree of strain, an annealing process at 10^{-6} Torr was necessary to achieve a measurable carrier density produced by the formation of oxygen vacancies. The charge carrier concentration, n, determined by Hall measurements, versus the experimental strain is plotted in Fig. 5.4 b). Although n presents a value in the same order for all the samples ($\approx 10^{20}$ cm^{-3}), it reaches the maximum value for less stressed samples, i.e. those grown on STO

and LSAT. Considering the nominal charge contributed by the 2% Nb-doping, $n \approx 3.27 \text{x} 10^{20}$ cm^{-3} (indicated on Fig. 5.4 b)), this shows that samples with more defects (more degree of either positive or negative strain) exhibit a carrier density similar to the expected nominal value. This indicates that more stressed samples exhibit a higher concentration of defects (V_{Sr}) which trap the extra charge donated by the oxygen vacancies created in the post-annealing process.

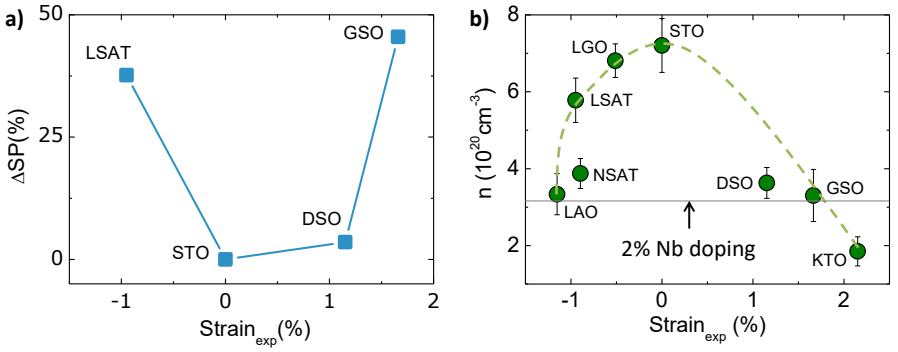

Figure 5.4: a) Evolution of ΔSP as a function of epitaxial strain. ΔSP is defined as the difference between the minimum/maximum in the SP signal of the $V_{\ddot{O}}$ accumulation/depletion regions. b) Charge carrier density as a function of experimental strain for some of the samples studied in this Thesis. The dashed line is a guide to the eye.

5.3 Room temperature diffusion coefficient of oxygen vacancies

As mentioned before, the understanding of the $V_{\ddot{O}}$ diffusion can be particularly interesting for many applications, including solid oxide-fuel cells, catalysts, resistive switching memory devices and photo-electrochemistry. For many of these applications, the knowledge of the room temperature diffusion coefficient is crucial.

In order to determine the diffusion coefficient of the strained thin

films, the experimental approach is similar to the one used in the previous Section: First, a rectangular area (3×8 μm) of the sample surface is poled with a positive voltage (+10V) and on the right side, another rectangle with the same dimensions is recorded with a negative voltage (-10V). The positive/negative tip bias disturbs $V_{\ddot{O}}$ distribution of the whole STO thickness under the poled area. Then, the electric field is set at 0 V, allowing the free relaxation of vacancies at room temperature across the thin film. The time-dependence of the EFM signal is registered during one day, taking an image every 30 minutes. Essentially, the EFM signal will decrease over time, describing how the concentration of vacancies approaches the equilibrium state. As the sample is recorded with positive and negative voltages, the diffusion is studied for both the accumulation and the depletion of $V_{\ddot{O}}$ (positive/negative concentration gradient).

Theoretically, oxygen vacancies could diffuse along and perpendicular to the film surface; hence the effect of surface mobility should also be considered apart from diffusion into the film bulk. However, a careful analysis of the profiles extracted from the time-dependence of the EFM images, shows that the border of the poled regions remains well defined over time (Fig. 5.5 a)).

For quantifying the broadening, the EFM profiles were fitted to a Gaussian function, extracting the full width at half maximum (FWHM) at different times and comparing it with the voltage amplitude in the central part of the recorded part; Figures 5.5 b) and c), respectively. From these results, we can conclude that the lateral diffusion would not perturb the EFM signal and the FWMH variation over time is negligible compared with the rapid decrease in amplitude even at short times, justifying the assumption that on average, the diffusion occurs mainly along the thickness of the films.

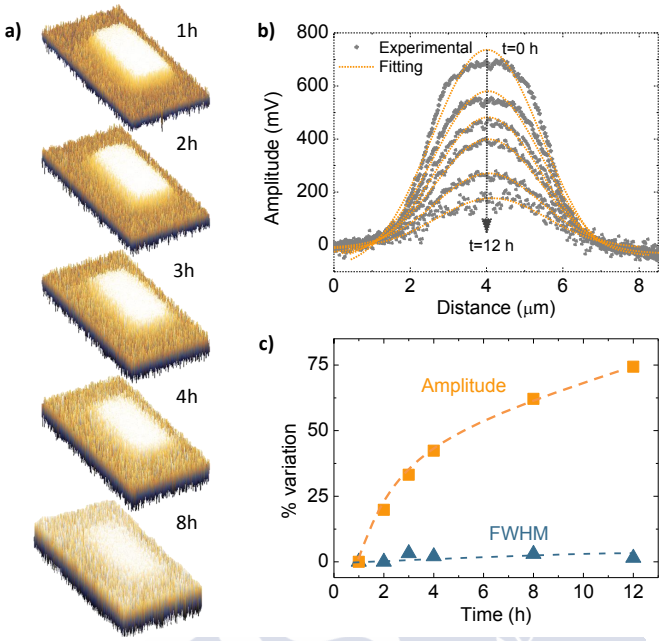

Figure 5.5: a) 3D plot of the evolution of EFM signal during 8 hours. The size of the area poled is 3×8 μm. b) Time dependence of EFM profiles over 12 hours, extracted from the images. Orange solid lines are Gaussian fittings in each case. c) Amplitude and FWHM variation versus time, obtained from the fittings.

Under these conditions, the second Fick's law in its one dimensional form can be used to follow the $V_{\ddot{O}}$ redistribution and to determine their diffusion coefficient:

$$\frac{\partial[V_{\ddot{O}}]}{\partial t} = D\frac{\partial^2[V_{\ddot{O}}]}{\partial^2 z^2} \tag{5.1}$$

where D is the diffusion coefficient. This law describes how the oxygen vacancies spread over time from a region of higher concentration towards a region of lower concentration, in order to recover the initial homogenous distribution.

Solving the above equation by the method of separation of variables or by the Laplace transformation, the solution becomes [170, 171]:

$$[V_{\ddot{O}}](t) = 1 - \frac{8}{\pi^2}\sum_{n=0}^{\infty}\frac{1}{(2n+1)^2}exp\left\{\frac{-D(2n+1)^2\pi^2 t}{l^2}\right\} \quad (5.2)$$

The corresponding solution for Eq. 5.2 at very long times (t→∞) is:

$$\Delta V_{\ddot{O}}(t) = \frac{[V_{\ddot{O}}](t) - [V_{\ddot{O}}(\infty)]}{[V_{\ddot{O}}](0) - [V_{\ddot{O}}(\infty)]} = \frac{8}{\pi^2}e^{\frac{-\pi^2 Dt}{l^2}} \quad (5.3)$$

where $[V_{\ddot{O}}](t)$ denotes the average vacancy concentration in the sample surface at any given time *t*, $[V_{\ddot{O}}](\infty)$ refers to the time required for the vacancy concentration within the enriched/depleted areas to recover equilibrium with the average concentration of the sample surface and $[V_{\ddot{O}}](0)$ represents the initial $V_{\ddot{O}}$ concentration immediately after recording with positive/negative tip bias.

Assuming that the EFM amplitude is proportional to the oxygen vacancy concentration, we can consider Eq. 5.3 to determine the slow diffusion coefficient at room temperature. The results for the time-dependent EFM amplitude of a thin film of STO grown on GSO are shown in Fig. 5.6 e-h). In the same figure (a-d), the whole process for the enriched $V_{\ddot{O}}$ region recorded with positive voltage is schematically represented.

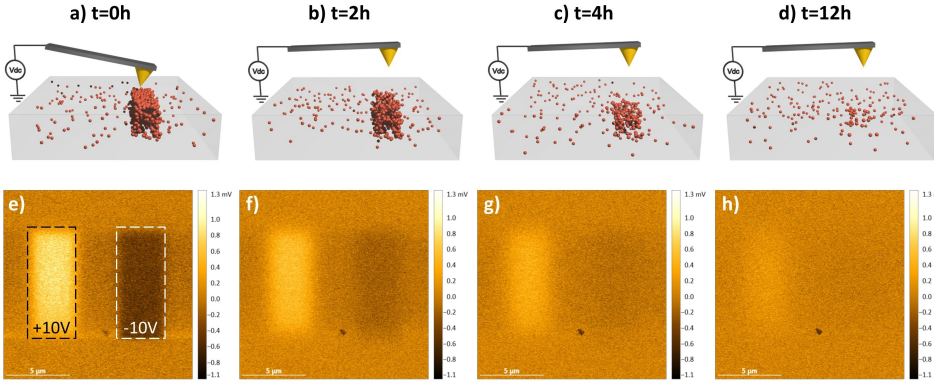

Figure 5.6: Sketch of the $V_{\ddot{O}}$ relaxation (a-d) and the corresponding evolution of the EFM amplitude over time at zero DC bias (e-f). a, e) Immediately after removing the AFM tip bias, b, f) after 2 hours, c, g) after 4 hours and d, h) after 12 hours. The results correspond to a film of STO grown on GSO.

By extracting the profiles of the EFM amplitude over the time (Fig. 5.7) and taking the average value of the positive (negative) poled region, we can obtain the decay of the EFM signal for the depletion (accumulation) of $V_{\ddot{O}}$, see Fig. 5.7 b).

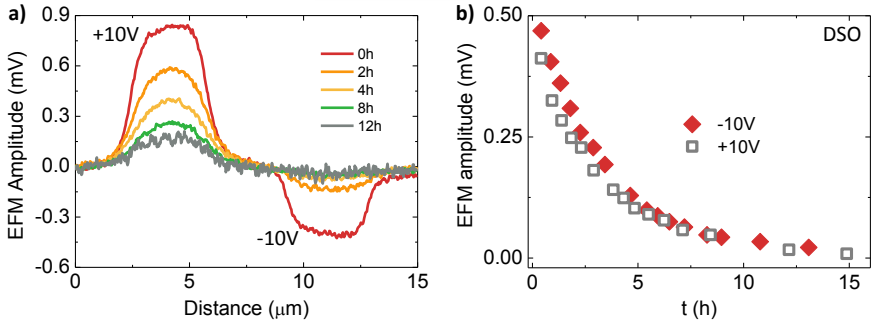

Figure 5.7: a) Profile of the EFM amplitude at zero dc bias over time extracted from Fig. 5.6. The results correspond to a film on GSO. b) Decay of the EFM signal for both accumulation (-10 V) and repulsion (+10 V) of $V_{\ddot{O}}$.

By repeating the same process for all the samples with different degrees of strain (both positive and negative), the strain dependence of diffusion coefficient of $V_{\ddot{O}}$ can be extracted using Eq. 5.3. Fittings of the experimental data for two representative cases (films grown on LSAT and GSO) are shown in Fig. 5.8 a).

The values of the diffusion coefficient are the averaged values from the initially depleted/accumulated surface regions ($\pm$V). The two values show similar results for each film, meaning that the incorporation of atmospheric oxygen to the surface is not an important contribution to the equilibration of the EFM signal (see Fig. 5.7 a). Oxidizing the initially reduced sample surface will require adsorption of oxygen from the atmosphere, dissociation, and diffusion through the lattice. On the other hand, reducing an initially oxidized region will require diffusion of the vacancies towards the surface, recombination (probably forming peroxide-ions) and formation of molecular oxygen. These processes are expected to show quite different activation energies. Therefore, the observation of a similar D after applying a positive or negative field suggests that oxygen exchange through the surface is not an important contribution to time-dependent surface voltage in our case, and that oxygen redistribution in the material is the mechanism governing this process.

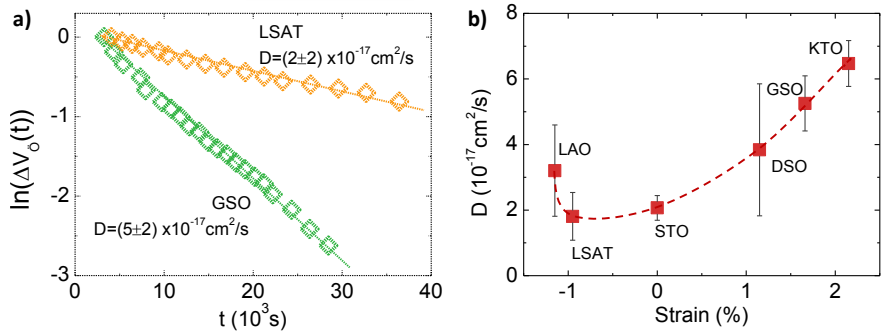

Figure 5.8: a) Fittings according to Eq. 5.3 of the EFM signal for samples grown on LSAT and GSO. b) Strain dependence of the diffusion coefficient of $V_{\ddot{O}}$ at room temperature. The dashed line is a guide to the eye.

The values of the diffusion coefficient determined from the fittings for all the thin films are shown in Fig. 5.8 b). The unstrained film grown on STO presents a value of $D \backsim 2 \times 10^{-17}$ cm^2/s, which is in very good agreement with the value reported in bulk STO, extrapolating from high temperature [144]. Also, during this Thesis. Das *et al.* [160] reported a similar experiment to ours, determining directly the room temperature D of $V_{\ddot{O}} \approx 10^{-19}$–$10^{-18}$ cm^2/s in unstrained STO thin films, in excellent agreement with our results.

Furthermore, D shows a pronounced strain-dependence, increasing an impressive $\approx$350% for 2% tensile strain, compared to unstrained films (Fig. 5.8). Meanwhile, a moderate compressive stress does not produce any appreciable effect on the diffusion coefficient of oxygen vacancies, except for the film grown on LAO, in which D raises by 50%. This film presents a higher concentration of defects formed to relax the high degree of compressive strain, which could affect the diffusion of vacancies through the film in an unpredictable way. Therefore, overall, one could say that D tends to increase as the unit cell volume becomes larger. This trend has already been reported also for other complex oxides, such as $SrCoO_3$ [172, 173].

The results shown in Fig. 5.8 b) are fully consistent with DFT calculations, which predicted a continuous increase for the $V_{\ddot{O}}$ diffusion with tensile strain [174], while a compressive strain larger than $\approx$-4% is necessary to decrease the energy barrier for diffusion [175]. Moreover, these calculations predict a significant role of complex TiO_6 rotations in the anisotropic oxygen diffusion in STO.

The strain-dependence of *D* has important implications for the design of ionic-conducting devices, like resistive switching memories: while tensile strain would favour the writing process in such devices due to its high drift mobility, it would also reduce the retention time due to the increase of the diffusion coefficient. Therefore, this type of ion-based devices will be adversely affected by tensile strain.

To study the possibility to define multiple stable neighbouring states, we poled side-by-side areas with different voltages ($\pm$5 V, $\pm$10 V), under compressive and tensile stress. The results demonstrate clear contrast boundaries between adjacent zones recorded with different sign

and magnitude of voltage, and also exhibit an excellent retention between them. However, at short times the influence of strain on diffusion becomes even more remarkable. For instance, the signal decays ≈50% after 3 hours on the sample grown on LSAT (Fig. 5.9 a)), while on GSO it decreases by ≈75% (Fig. 5.9 b)). This demonstrates again the negative effect of tensile strain in the stabilization and also in the retention of the multipotential surface states.

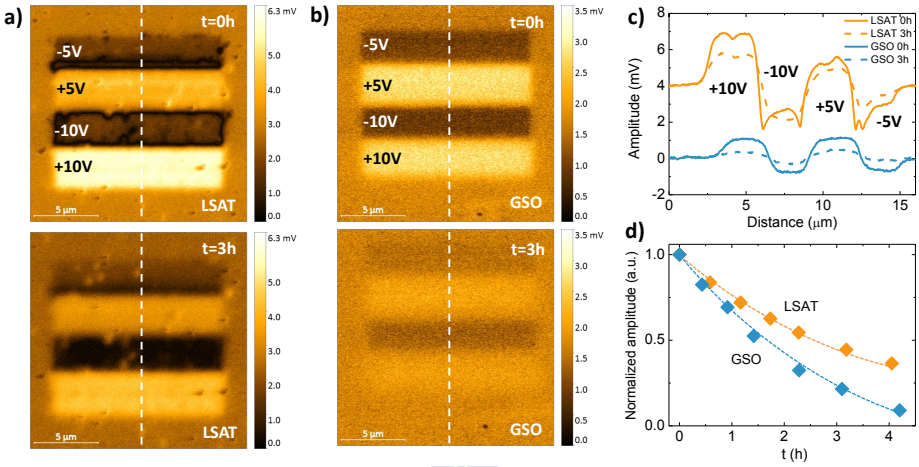

Figure 5.9: Record of the sample surfaces with variable voltages from -10 to + 10V, which generates adjacent areas with different surface potential. (a) EFM amplitude on LSAT immediately after the record and 3 h later. (b) Same record on the sample deposited on GSO. c) Profiles along the white dashed lines of the images a) and b). (d) Normalized evolution of the EFM amplitude for both samples during 4.5 h. After 3 h the EFM signal decays ≈50% from the initial value in LSAT, and ≈ 75% in GSO. Dashed lines are guides to the eye.

Other important requirements for competitive ReRAM memories imply low writing voltages, short pulse times, and high thermal stability. Normally, write operation should be in the range of a few hundred mV and present a length of pulse <100 ns to provide an advantage over current devices, and the different states should be stable up to ≈85°C [158].

To achieve more quantitative insights about the role of these parameters on $V_{\ddot{O}}$ distribution in our system, we recorded different areas at constant pulse time with different tip bias and vice versa, maintaining the tip in contact with the sample surface but without dynamic scan.

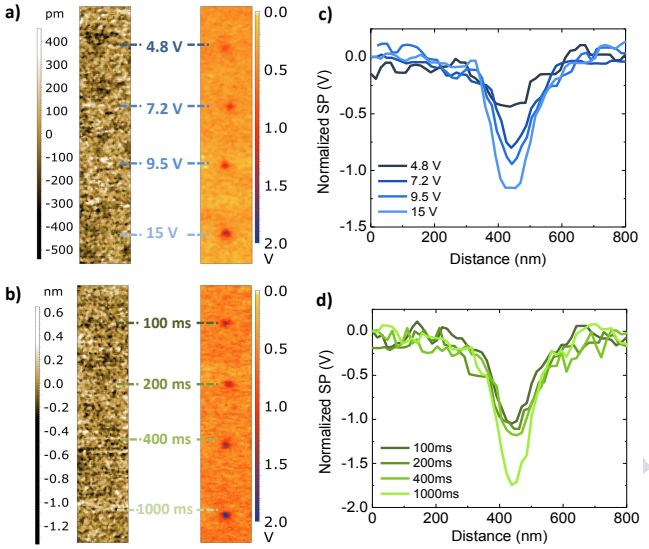

Figure 5.10: Influence of tip bias and pulse time on the $V_{\ddot{O}}$ distribution on GSO. a) Topography (left) and surface potential (right) of four-dot array, which were performed by pausing the tip for 0.4 s and varying the tip bias from 4.8 V to 15 V. b) Dots recorded while keeping the voltage constant at 15 V and varying the pulse time for 0.1 to 1 s (right). Resulting profiles of the normalized surface potential for the dots poling at constant time (c) and constant voltage (d), respectively.

The results for topography and KPFM signals are shown in Fig. 5.10. The impact of vacancies accumulation is negligible in the sample topography, independently of the tip bias or the pulse time. In Fig. 5.10 c), the profile of the KPFM image also evidences the existence of a threshold in the applied tip bias ($\approx$ 5-6 V), above which there is a sizable increase in the $V_{\ddot{O}}$ concentration, independent of the applied voltage. Similarly, short pulse times (less than 500 ms) accumulate quanti-

tatively the same amount of vacancies (see Fig. 5.10 d). However, once the pulse time is increased at 1000 ms the local concentration of vacancies increases by ≈1/3. The existence of these threshold voltages/times indicates an activation energy for ionized vacancies to detach from lattice defects, most probably cationic vacancies, which can affect the drift mobility beyond strain [75].

Regarding the temperature dependence of the $V_{\ddot{O}}$ distribution, we compared write/read voltage measurements performed at room temperature 25° and at 60°C, using different pulse times with the same tip bias of +15 V (Fig. 5.11). Poling of the sample and subsequent KPFM scans are separated by 15 minutes. The required pulse time to achieve a measurable change of the surface potential increases substantially with temperature, reflecting the rapid increase of D as the temperature rises. This result evidences the low retention of the different potential states, which can be erased at moderate temperatures.

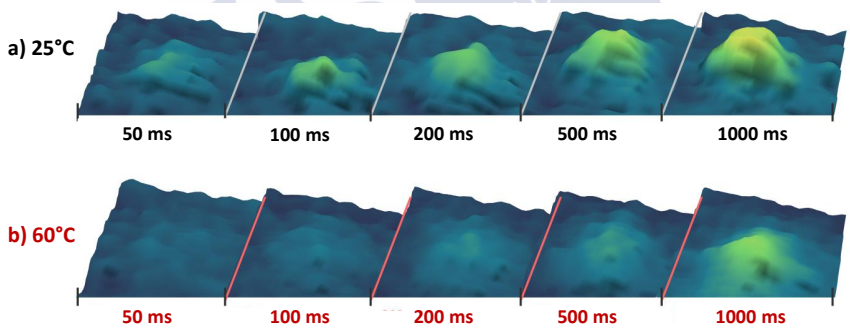

Figure 5.11: 3D representation of the surface potential, related to the $V_{\ddot{O}}$ distribution, after different pulse times (+15 V) applied at 25°C (a) and 60°C (b).

Finally, we intend to demonstrate that the oxygen vacancy manipulation using an AFM tip bias is a reversible process. Thus, we overwrote with -10 V the previously poled areas with ± voltage, moving $V_{\ddot{O}}$ closer to the sample surface. As can be observed in Fig. 5.12, the final poled region with negative voltage shows higher vacancy concentration in the

vacancy-deficient region and also in the region already previously enriched with $V_{\ddot{O}}$, demonstrating the complete reversibility of the process.

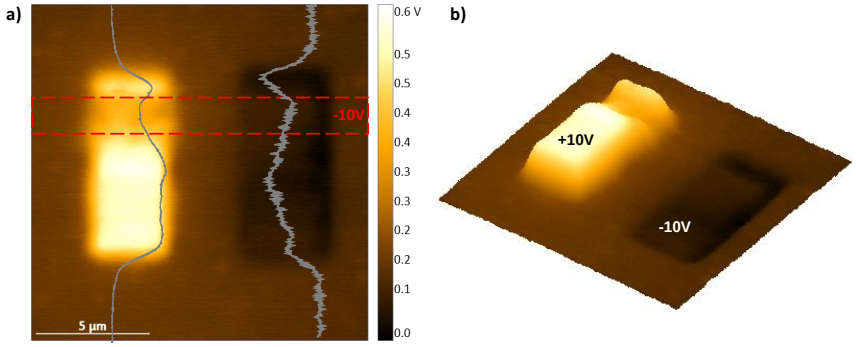

Figure 5.12: a) KPFM image of a region of the sample surface previously recorded with positive and negative voltage and afterwards, overwritten with negative voltage (red dashed line). The profile of the surface potential can be seen on the image (solid grey lines). b) 3D representation of the image a).

5.4 Summary

In this Chapter, a controlled manipulation of oxygen vacancies at room temperature by means of a biased AFM tip has been demonstrated. The effect of epitaxial strain in the $V_{\ddot{O}}$ diffusion, D, has been also investigated at room temperature. We have followed the time dependence of the local EFM signal, after the distribution of $V_{\ddot{O}}$ is locally modified by the AFM tip bias, extracting the diffusion coefficient by fitting the experimental data to the Fick's diffusion law. Tensile strain enhances considerably the vacancy diffusion coefficient by 350% for 2% strain with respect to unstrained films, while moderate compression does not show an appreciable effect.

Finally, given that $SrTiO_3$ can be proposed as a promising candidate to be used in ReRAM memories, we have explored some of the main requirements for the applicability of these devices, such as tip bias, pulse

time, reversibility and temperature over the local vacancy distribution in the films. Some factors such as thermal stress and retention need to be improved before considering the implementation of STO in ionic-based devices.

The possibility for controlling the distribution of oxygen vacancies at a nanoscale level in STO opens a route to use the movement of anionic defects in new technologies. However, a material optimization needs to be addressed to meet the requirements for competitive ReRAM memories. In this sense, considering the results, strain-engineering can play a major role to tune aspects such as mobility and diffusion of vacancies in STO. This mechanism could be extended to other transition metal compounds.

USC
UNIVERSIDADE
DE SANTIAGO
DE COMPOSTELA

6. TiO_6-Octahedral rotations and ferroelectric-like response in strained $SrTiO_3$ thin films

People who have it too easy in early life have a disadvantage for later on, because they get to thinking that everything is going to be easy.

Mildred Dresselhaus. She was the first woman Institute Professor and Professor Emerita of Physics and Electrical Engineering at the Massachusetts Institute of Technology.

Most ABO_3 perovskites undergo structural distortions associated with the tilt or rotation of the BO_6 octahedra about one or more of the crystal axes in order to increase the bonding strength and coordination number. As the metal-oxygen-metal (or in general, cation-anion-cation) bond angles can influence the electronic structure of the materials, small changes in the oxygen octahedra tilting have important implications on the electronic and magnetic properties. The A-site substitution with cations of different radii is an effective strategy to tune the degree of the BO_6 octahedra rotation, which can profoundly affect the spin in-

teraction along the crystal. Thus, the ability to control these rotations in the perovskite structure is very important to understand structure-property relationships and also to create multifunctional materials with new properties [47, 56].

Apart from the change in the cation size, epitaxial strain is an alternative tool for tuning the connectivity of the BO_6 octahedra [57, 176]. Nonetheless, it is becoming clear that the octahedral rotation mismatch between substrate and film could potentially play a more dominant role in controlling film distortions [177]. In addition to imposing epitaxial strain on the film, the substrate force the BO_6 octahedra to stay connected, transferring octahedral distortions and tiltings across the interface and imprinting them into the film. This is particularly important considering that most of the commercially available substrates used for the growth of perovskite thin films present symmetries with robust octahedral distortions, such as $a^-b^+c^-$ in orthorhombic scandates or $a^-a^-a^-$ in LAO. Thus, Liao *et al.* [178] reported the control of the magnetic and electronic properties in manganite heterostructures by transferring the octahedral rotations present in a $NdGaO_3$ substrate to the $La_{2/3}Sr_{1/3}MnO_3$ thin film. Therefore, a deterministic control over the film distortions necessarily implies the understanding of how the octahedral units in perovskites respond to the strain and to the substrate octahedral rotations [58].

In this regard, one of the emerging properties that can be induced by means of the octahedral rotations is the ferroelectricity. Octahedral rotations by themselves cannot induce ferroelectric polarizations in the perovskite structures, but combined with defects or even strain, they can do so [48, 179]. This relationship has not been extensively studied too much from the theoretical standpoint, due to the complexity of implementing the simulations [180–182] and experimentally, due to the problem to isolate the effect of the different parameters involved in the phenomena.

Recently, A. Gruverman et *al.* [183] reported a ferroelectric-like response in LAO/STO heterostructures mediated by the electric field induced by an AFM tip bias, which produces oxygen vacancy migration, similar to a previous report performed by C. B. Eom *et al.* [184].

Furthermore, although $SrTiO_3$ is an incipient ferroelectric that remains paraelectric down to 0 K, epitaxial tensile strain can modify its delicate state, turning it into a ferroelectric [82]. Given these reports, it is therefore reasonable to expect that octahedral rotations as well as strain, cationic and oxygen vacancies could play a major role in controlling the ferroelectricity in STO thin films and more generally, in perovskites.

In this Chapter, we will present the results of experiments and ab-initio simulations, focusing on the structural properties of the STO thin films. The different octahedral rotation patterns of the films will be determined experimentally as a function of strain, and by means of ab-initio calculations we will address their origin. Afterwards, the ferroelectricity in STO thin films under specific conditions will be studied, examining which parameters are the most relevant to induce it, such as strain, octahedral rotations or oxygen vacancies.

6.1 Strain-dependence of octahedral rotation pattern

In perovskites, a progressive reduction of the ionic radius at the A site is expected to induce a cooperative rotation of the BO_6 octahedra, which could reduce the symmetry from cubic (t = 1) to tetragonal ($I4/mcm$), rhombohedral ($R\bar{3}3c$, rotation along [111] axis), and orthorhombic ($Pbnm$ or $Pnma$, rotation along [110] axis) as t decreases (see Chapter 1, Eq. 1.1 for more details).

STO is cubic at room temperature having no octahedral rotations ($a^0a^0a^0$) and t≈1. Below 105K, a phase transition occurs in STO, which becomes tetragonal with an out-of-phase rotation along the c-axis ($a^0a^0c^-$) [185]; this is also true for 2%-Nb:STO.

Nevertheless, the presence of V_{Sr} could introduce a distortion similar to an average reduction of the ionic radius of the A cation, which coupled with the effect of strain (and its cooperative nature) can drastically change the configuration of octahedral rotations of the material. In addition to epitaxial strain and defects, an alternative interfacial coupling effect can also take place when an octahedral rotation mismatch

between substrate and film exists. The mismatch of atomic displacement at the heterointerface is generally accommodated by either deforming or rotating the oxygen octahedra in the film.

By determining the octahedral rotation pattern in the films, we can investigate whether such rotations are controlled by the strain, cationic vacancies or the rotation pattern of the substrate underneath. The different structures and octahedral distortions of the substrates are summarized in Fig. 6.1. Both GSO and DSO present orthorhombic structure with a distortion compatible with the space group $Pnma$, whereas LAO is rhombohedral with rotations described by the $a^-a^-a^-$ ($R3c$ space group) tilting pattern in Glazer notation [59]. LSAT, STO and KTO possess cubic structure without any rotations ($a^0b^0c^0$).

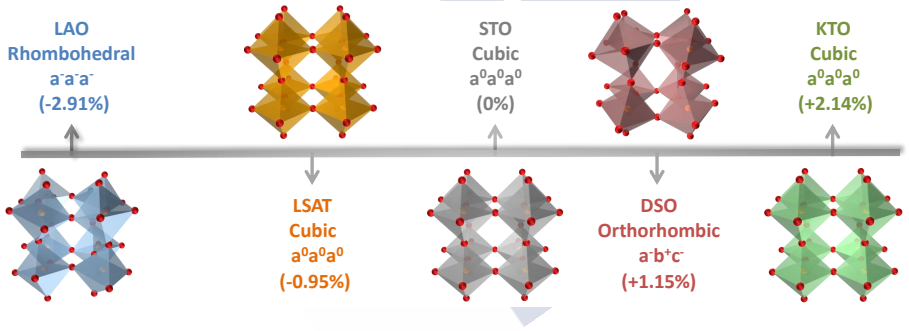

Figure 6.1: Summary of the phase and octahedral distortions of the substrates studied in this Chapter, indicating the precise octahedral rotation pattern in each case. The nominal degree of strain induced in STO thin films grown on these substrates is also indicated in each case.

The different octahedral rotation patterns can be extracted by carefully investigating the presence or absence of X-Ray half-order reflections in the thin films, as explained in Chapter 2.

On the compressive side, the films exhibit in-phase rotation along the a and b axes and lack of rotation along c axis, $a^+b^+c^0$ ($Immm$ space group), independently of the BO_6 rotation pattern of the substrate (Fig. 6.2). Consequently, we can conclude that under compressive strain the substrate does not impose its own octahedral pattern on the films.

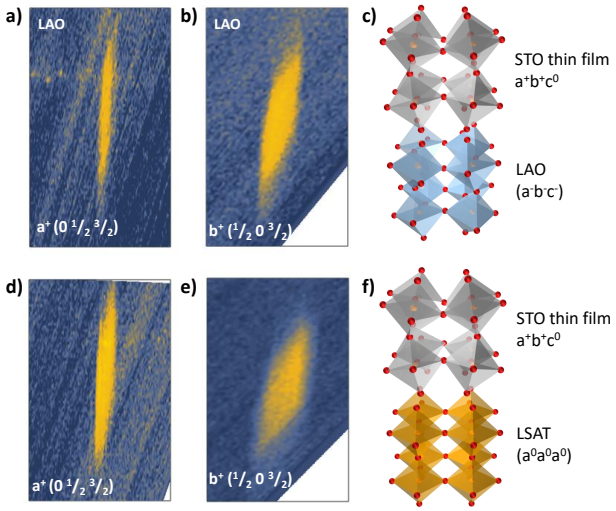

Figure 6.2: High resolution reciprocal space maps around half-order reflections for compressive Nb:STO thin films. The reflections correspond to the rotations pattern characteristic of $a^+b^+c^0$ found for samples grown on LAO (a,b) and LSAT (d,e). c,f) Sketches showing the distortions of the films and substrates.

However, the film grown under tensile strain on an orthorhombic substrate with robust distortions (DSO, $a^-b^+c^-$) exhibits the same octahedral configuration than the substrate underneath (see Fig. 6.3). Therefore, the substrate has imprinted its characteristic octahedral rotation pattern into the film.

However, the film grown on cubic KTO does not show hints of any octahedral rotations, despite of the large tensile strain applied. This indicates that the interfacial coupling could play a dominant role in controlling the octahedral rotations pattern of the film under tensile stress.

Surprisingly, the film deposited on an STO substrate, in which the lattice mismatch can be considered negligible, presents again the $a^+b^+c^0$ configuration compatible with a tetragonal distortion and described by $Immm$ space group (Fig. 6.4 a,b). Because from our experiments it is not possible to determine the precise amplitude of the octahedral rotation, which could be the same along the a and b axes,

the tilt system can also be described as $a^+a^+c^0$, corresponding to the $I4/mmm$ space group.

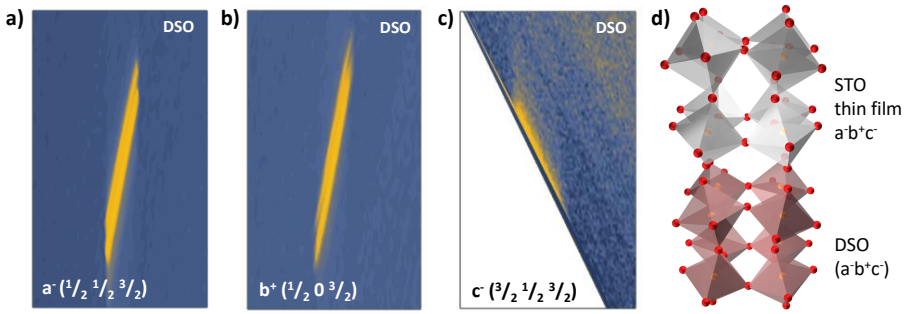

Figure 6.3: a-c) High resolution reciprocal space maps around half-order reflections for the sample grown on DSO under tensile strain. The reflections correspond to the rotation pattern $a^-b^+c^-$ characteristic of the space group $Pnma$. d) Sketch showing the distortions of the film and the substrate.

Given the negligible lattice mismatch between the Nb:STO film and the STO substrate, the distortion could be induced by the presence of V_{Sr} throughout the lattice of the film, which are introduced unintentionally during the PLD deposition process.

Note also that the clear observation of the x-ray half order reflections in all cases implies that the tilting of the TiO_6 octahedra is propagated along the whole sample, not just around a local vacancy. In addition, as can be seen in Fig. 6.4 c,d), the rotation pattern does not change in films grown at very low PO_2, i.e. with a higher concentration of oxygen vacancies. Therefore, oxygen vacancies can be ruled out as the main source of the distortion.

The presence of V_{Sr} introduces a distortion similar to an average reduction of the ionic radius of the A cation. This decreases the tolerance factor below 1 and subjects the Sr-O (Ti-O) bonds to tensile (compressive) strain, resulting in a rotation of the TiO_6 octahedra to accommodate this stress. The compressibility of Sr-O bonds is often larger than the one of Ti-O bonds [53], so that compressive stress goes in the

same direction as the reduction of the ionic radius. Consistent with this hypothesis, the same rotation pattern was observed for all the films grown under compressive stress, either on cubic LSAT or orthorhombic LAO, and also for the unstrained film on STO substrate due to the presence of Sr^{2+} vacancies.

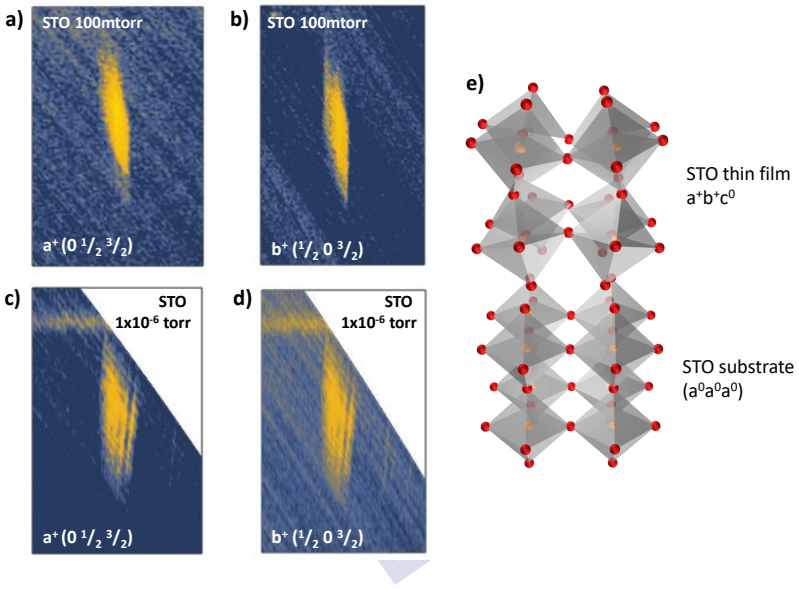

Figure 6.4: High resolution reciprocal space maps around half-order reflections for unstrained Nb:STO thin film on STO substrate. a, b) As-grown film at 100 mTorr of oxygen pressure and c,d) film after a post-annealing procedure at 1×10^{-6} Torr. The rotation pattern observed corresponds to the space group $Immm$ ($a^+b^+c^0$) or $I4/mmm$ ($a^+a^+c^0$). e) Sketch showing the distortions of the film and the substrate.

Nevertheless, positive stress dominates over the effect of V_{Sr}, imposing on the films the rotation pattern of the crystal underneath. These results demonstrate that different octahedral rotation patterns are induced in thin films prepared under similar conditions (identical composition) but subject to different degrees (and sign) of epitaxial stress (i.e., deposited on different substrates). This particular tuning of the octahe-

dral configuration by means of strain, substrate rotations and/or cationic vacancies has not been previously reported neither theoretically nor experimentally for Nb:STO thin films. The next step will be to understand the mechanism that produces it. Once the mechanism is understood, experiments can be designed in order to control it.

6.1.1 Origin of the distortions: ab-initio calculations

To determine the influence of the strain, cationic vacancies or substrate distortions on the different octahedral configuration of the STO film, we performed DFT calculations and coupled the results with the experiments.

Computational details: The calculations were carried out using the Wien2k code and the generalized gradient approximation (GGA) in the PBE scheme. The values of the atomic sphere radii (R_{mt}) were chosen as 1.87 a.u. for Ti, 2.5 a.u. for Sr and 1.69 a.u. for O. We used a plane wave cut-off described by $R_{mt}K_{max}= 6$, and the values for the k-mesh were 4×4×4 sampling of the full Brillouin zone. A pseudocubic 2×2×2 supercell consisting of 40 atoms (8 Ti, 8 Sr and 24 O) was used. Removing an oxygen in the structure to simulate the effect of an oxygen vacancy represents a concentration close to 4%, which is comparable to the experimental values (ranging from 2 to 4%) [106].

In order to find the appropriate computational parameters to describe our system in the best possible manner, we decided to relax the initial structure without rotations. Thus, we carried out a simple calculations for the supercell without any rotations or oxygen vacancies, optimizing the volume, and the results can be seen in Fig. 6.5 for GGA-PBE functional. The same calculations extracting an oxygen atom were also performed. For this case, the optimized lattice constant is also overestimated compared to the bulk parameter of the STO (a=3.905 Å). However, the disagreement between lattice constant and experimental values is less than 1% (less than 3% in volume), which is in good agreement

with the reported in the literature [186, 187]. The increase in volume for the system with the oxygen vacancy is fully consistent with the unit cell expansion due to the larger ionic radius of the Ti^{+3} (0.81 Å) compared to Ti^{+4} (0.75 Å).

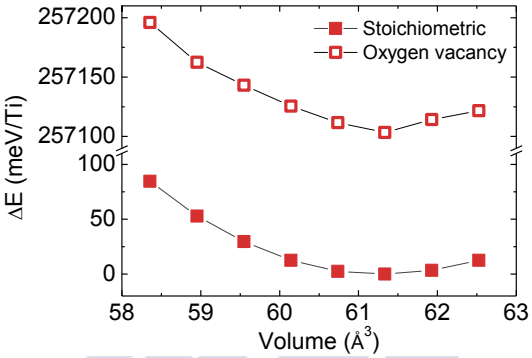

Figure 6.5: Total energy as a function of the cell volume for a 2×2×2 supercell of stoichiometric STO (solid squares) and with an oxygen vacancy (open squares). The energies were determined taking as a reference the ground state of stoichiometric STO.

As a second step, we introduced the three possible octahedral rotation patterns observed experimentally ($a^+a^+c^0$, $a^-b^+c^-$ and $a^0b^0c^0$) in the structure with 40 atoms and strain between -6% to +6%. The simulations were carried out using lattice constants very similar to those obtained experimentally in STO thin films (see Chapter 4). Consequently, a=b were set according to the degree of strain chosen in each case, taking as a reference the experimental lattice parameter of STO in bulk (a=3.905 Å), and c was determined assuming that the Poisson coefficient is conserved, i.e. ν = 0.23 (more details in Chapter 4 and Fig. 4.5). Regarding the octahedra rotation angles in the structures, given that there are no experimental data about it, a similar value (4°) to those reported in the literature has been taken [188, 189]. During the simulations, both in-plane and out-of-plane lattice constants were locked and only the internal coordinates of the ions were relaxed until the conver-

gence criteria were satisfied. The total energies are shown in Fig. 6.6 for the structures under strain without any type of defects.

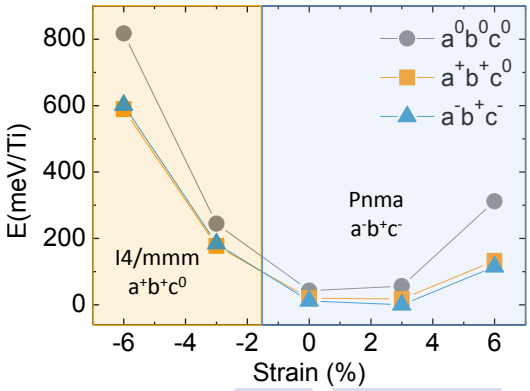

Figure 6.6: Energy versus strain for the different rotations patterns of TiO_6 octahedra in STO. The three structures observed experimentally are investigated: $Pm\bar{3}$m ($a^0b^0c^0$), $I4/mmm$ ($a^+a^+c^0$) and $Pnma$ ($a^-b^+c^-$).

For compressive strain, the $I4/mmm$ phase is the most stable with in-phase rotations around [100] and [010] axes, in completely agreement with the experimental observations. On the contrary under tensile stress, the orthorhombic $Pnma$ has the lowest energy with tilt pattern $a^-b^+c^-$, also in full agreement with the experiments(Fig. 6.3). Nevertheless, at 0% strain, the three structures are very similar in energy and our calculation cannot discriminate the most stable among them. As the stress increases, both positive or negative, the energy of the three structures becomes different, being the cubic without rotations always the less favourable. Therefore, apparently the strain explains the structures observed experimentally for both, compressive and tensile stress.

To identify the origin of the distorted structure at 0% strain, similar calculations were repeated by introducing an oxygen vacancy. Removing an O atom out of the system, reproduces a situation with ≈4% of vacancies. The results show that the $Pnma$ phase is the most stable over the entire range of strain we studied (Fig. 6.7 a)). Thus, the intro-

duction of an oxygen vacancy does not explain the rotations observed at 0% strain.

The effect of a cationic vacancy on the octahedral rotation pattern was also computed. To remove a Sr atom of the 2×2×2 supercell would imply a non-realistic concentration of 12.5%, so that a 3×3×3 supercell should be necessary to perform a more reasonable calculation. However, due to the excessive computational time demanding, the effect of a V_{Sr} can be alternatively simulated by substituting a Sr (Z=38) for a Ca (Z=20). The results are shown in Fig. 6.7 b), showing that $Pnma$ structure with ($a^-b^+c^-$) is the most stable independently of the degree and sign of strain.

Therefore, we can conclude that neither $V_{\ddot{O}}$ nor V_{Sr} alone introduce a substantial stabilization of the $a^-b^+c^-$ observed experimentally.

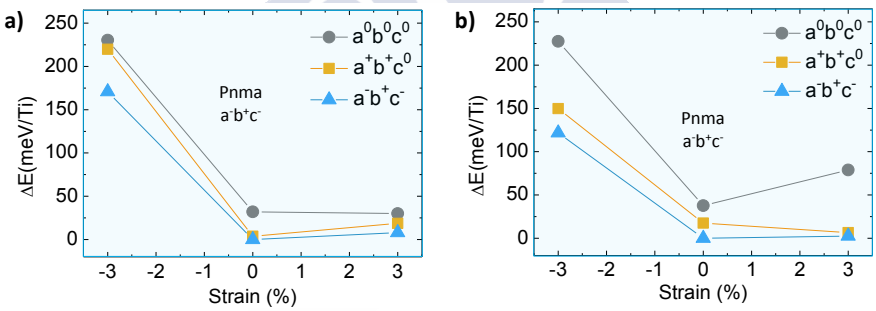

Figure 6.7: Energy versus strain for the three different phases observed experimentally. a) Simulations introducing an oxygen vacancy and b) alternatively substituting a Sr atom by a Ca.

6.2 Ferroelectric-like response

Haeni *et al.* [82] reported the emergence of ferroelectricity in strained STO thin films at room-temperature. Particularly, they expected in-plane polarization in tensile strained thin films, whereas the compressive stress would not produce a similar effect at room-temperature. Since

we have determined that epitaxial strain has such a large effect in determining the rotation pattern of the STO thin films, the influence of the different octahedral configurations on a possible ferroelectric (FE) response will be studied in this Section.

Typical signatures of a ferroelectric system include a change in the phase and also the presence of domain walls in th PFM signal, which characterize the local orientation of the polarization within the material [190–192]. In addition, the measurement of a hysteresis loop of the electromechanical response of an AFM tip as a function of applied dc bias, is often interpreted as an indicator of ferroelectricity. However, the interpretation of ferroelectric-like characteristics in local AFM probes as an evidence for the ferroelectric nature of the system has resulted in multiple controversies [193–195]. The observation of a PFM hysteresis loop can be originated from mechanisms different from ferroelectricity. For instance, electrostatic interactions between the tip and sample [196], hysteretic surface charging [197] or ionic mechanism [198] can also exhibit electromechanical hysteresis.

We have observed a FE-like response ($\sim$180° phase change and domain walls in the PFM response) in the STO films deposited on LAO, LSAT and STO. The result can be seen in Fig. 6.8, which shows a sudden change in the phase and amplitude signals in the area where a negative tip bias had previously been applied (i.e. higher oxygen vacancy concentration) for a thin film grown on LSAT. The effect is not appreciated in the zone poled with positive voltage (i.e. lower oxygen vacancy concentration). Same phenomena are also present in other films under compressive and at 0% strain (deposited on LAO and STO substrates) but not in tensile strained films, which present a completely different octahedral configuration. Furthermore, the change in the amplitude and phase disappears at short times (approximately 20 minutes), demonstrating that the oxygen vacancies and their local concentration can play a major role in the observation of the ferroelectric response. These hints suggest the existence of an interplay between certain octahedral rotation patterns and the presence of a high concentration of oxygen vacancies, which can give rise to a polar distortion and therefore to the ferroelectric response in PFM measurements.

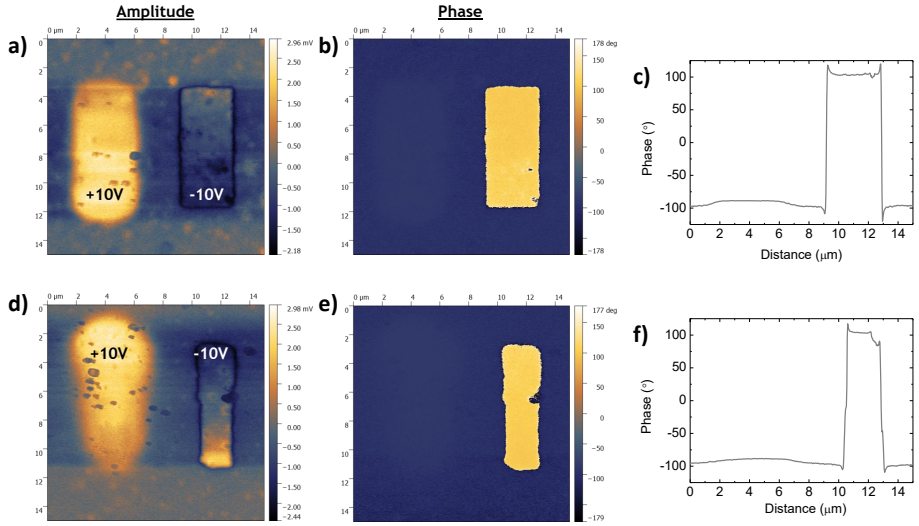

Figure 6.8: Amplitude (a,d) and phase (b,e) contrast of EFM images of a STO thin films deposited on an LSAT substrates under compressive strain. c,f) The profiles of the phase signal corresponding to b and e images, respectively. The surface of the sample was previously poled $\pm$10V, as is indicated on the images a and d.

Given the intense debate over the interpretation of the ferroelectric signatures from the PFM signals, in this Thesis we decided to address this issue from the theoretical point of view, trying to elucidate the role of the octahedral rotations and/or oxygen vacancies in the ferroelectricity of STO thin films.

6.2.1 Cooperative octahedral rotations and polarization: ab-initio calculations

Computational details: In this Section, the structural properties and ferroelectric polarization of different structures were calculated using the VASP package, based on the the projector-augmented wave method (see section 3.3 for more details). GGA-PBE [117], LDA [108] and

PBEsol [118] XC functionals are used for comparative studies. An energy cut-off of 600 eV is used to truncate the plane wave basis. Cells containing 5 atoms were used with 8×8×8 centered k-point sampling, meanwhile for the supercells of 20, 40 and 80 atoms 6×6×4, 4×4×4 and 3×3×4 centered k-points were utilized, respectively. The atomic coordinates were relaxed until the total energy is smaller than 10^{-6} eV between two ionic steps. The spontaneous polarization of the cells without defects was calculated either with the Berry phase method [126] or the method proposed by Meyer and Vanderbilt using the BEC [125].

The first step is to choose the more accurate XC functional to perform simulations in our system. For that, we determined structural properties such as lattice parameter a, cell volume and energy of the ground state for cubic STO without any rotations or distortions using the different XC functional considered. The results are showed in Table 6.1. As can be seen, the lattice parameters and the cell volumes are overestimated and underestimated by the PBE and LDA functionals, respectively. These results are consistent with the well-known underbinding (PBE) and overbinding (LDA) problems for these two functionals. Meanwhile, the lattice parameter predicted using the PBESol functional is also overestimated, but to a lesser extend than estimated by the PBE functional. However, despite of the deviation from experimental value (a=3.905 Å), the error only exceeds the 1% in the case of PBE.

	PBE	**LDA**	**PBESol**
a=b=c (Å)	3.96	3.88	3.93
Volume (Å^3)	61.89	58.58	60.60
s (%)	+1.28	-0.55	+0.58
E (eV)	-39.69	-43.82	-33.05

Table 6.1: Structural properties of $SrTiO_3$ $Pm\bar{3}m$ phase, including the lattice parameter (Å), the unit cell volume (Å^3), theoretical strain (s(%)) taking the experimental value (3.905 Å) as a reference, and the ground state energy (eV).

Additionally, we performed various tests comparing the results for the three functionals in order to compare the experimental and theoretical values, and find the functional which provides a better physical description of our system. First, we impose an out-of-plane polarization in the 5-atom cell, moving the Ti along the c-axis direction (see Fig. 6.9 a) and then relax the internal coordinates positions to see if the polarization is kept. The same calculations were also carried out by shifting the Ti in the [110] direction (in-plane polarization) as illustrated in Fig. 6.9 b).

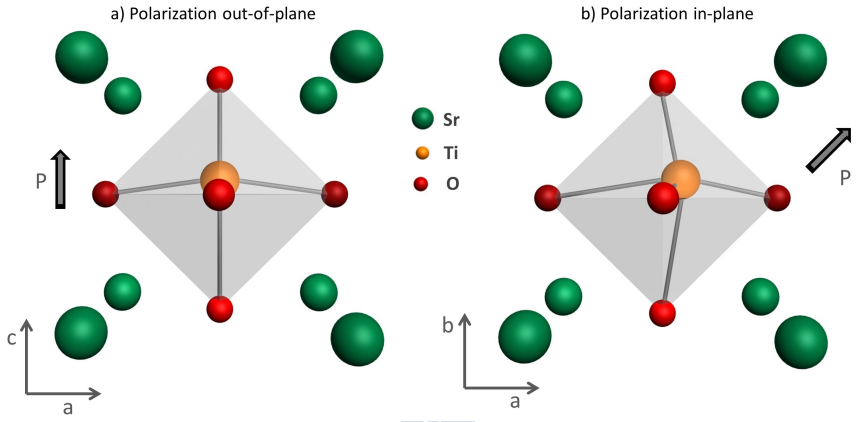

Figure 6.9: Sketch indicating the direction of the polarization. a) Out-of-plane polarization, the Ti-displacement is produced along the [001] direction. b) In-plane polarization along the [110] direction.

These calculations were performed for different degrees of strain, both positive and negative. Lattice parameters a=b were calculated for each degree of strain taking the experimental value as a reference (a=3.905Å). Then, c parameter was determined according to the Poisson's ratio (ν=0.23). This value of c is denoted as $c = 0\%$ in Figs. 6.10 and 6.11. For each value of strain, c is varied by a percentage respect to the $c = 0\%$ value and the structure is relaxed each time.

The results for out-of-plane polarization are shown in Fig. 6.10 for PBE, LDA and PBESol. The energy curves for LDA and PBESol

exhibit a clear distinguishable minimum independently of the sign and magnitude of strain. Nevertheless, the energy minimum is uncertain for PBE functional, for positive and negative strain values. For example, in Fig. 6.10 a) the energy curve corresponding to -3% of strain presents a flattening for high values of c, being difficult to determine the minimum unambiguously.

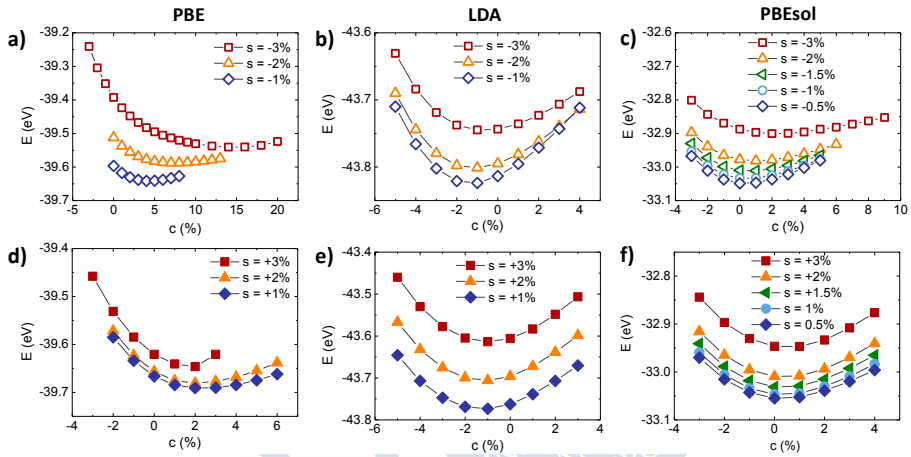

Figure 6.10: Energy versus c axis value after the relaxation setting the polarization along the out-of-plane direction. Simulations were performed for PBE (a,d), LDA (b,e) and PBESol (c, f) functionals.

Comparable calculations performed fixing the in-plane polarization do not exhibit this artifact independently of the XC functional used, as can be seen in Fig. 6.11. By plotting the optimized c-axes obtained for out-of-plane and in-plane polarizations as a function of the a-axis, a clear overestimation of c is evident by PBE functional and out-of-plane polarization, especially for compressive strain (Fig. 6.12 d). This artifact is called supertetragonality and it has been previously reported in the literature [199, 200]. The lattice distortion that we introduced is driven by the Ti off-center displacement along the respective polarization directions ([001] and [110]). This produces an imbalance between two nonequivalent Ti-O bonding interactions: shorter Ti-O has the more

covalent character, while longer Ti-O bond presents ionic character. LDA functional tends to homogenize the electron density, smearing out the differences between the shorter and longer Ti-O bonds. Therefore, the Ti off-center displacement and the distortion of the lattice parameters are underestimated.

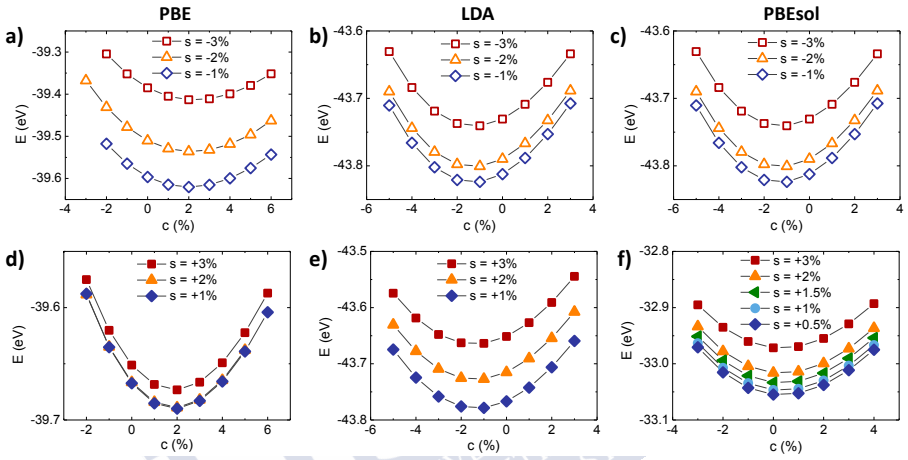

Figure 6.11: Energy versus c axis value after the relaxation setting the polarization along the in-plane direction. Simulations were performed for PBE (a,d), LDA (b,e) and PBESol (c, f) functionals.

However, PBE is designed to soften the overestimated bonding calculated by LDA, favouring stronger bondings (i.e. covalent and metallic bonds) and thus underestimates the relatively weak bonds (i.e. ionic bonds). Thus, the short Ti-O bond is energetically favoured by PBE, producing the supertetragonality artifact [199]. Similar phenomenology is also observed for PBESol, although much less pronounced and only in the case of -3% of compressive strain. It is worth noting that by comparing these results with the experimental values (Fig. 6.12 d-f), PBESol is clearly the functional that provides the best comparison with experimental values and therefore, this will be the XC functional chosen to perform the simulations from now on the rest of the Chapter.

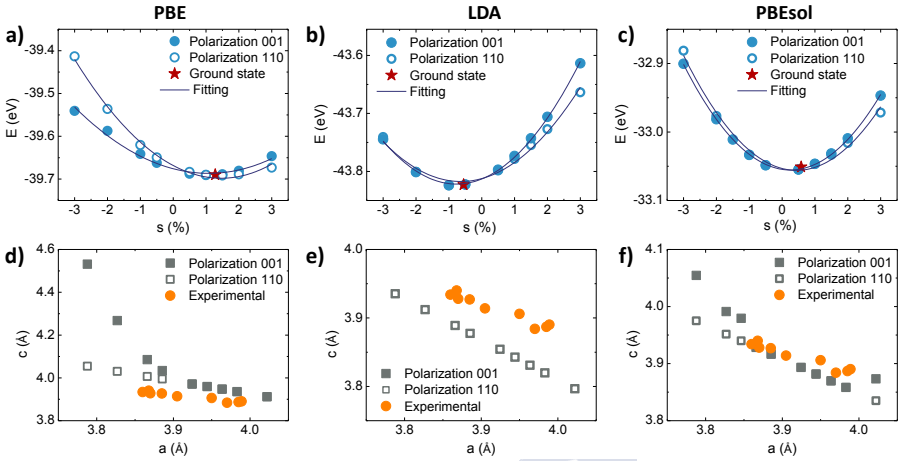

Figure 6.12: Energy versus strain for optimized values of c at each value of strain using PBE (a), LDA (b) and PBESol (c). Optimized value of c as a function of the a-lattice parameter for PBE (d), LDA (e) and PBESol (f). All simulations were performed for out-of-plane (solid symbols) and in-plane polarization (open symbols). In d-f) the experimental values are also plotted for comparison with the theoretical predictions (solid orange circles).

The atomic displacements between Ti-O, which indicates the off-centering of Ti cation, were determined in the relaxed structures using the PBESol and is shown in Fig. 6.13 a) as a function of strain. The out-of-plane polarization is favoured by compressive strain, whereas it vanishes under large tensile strain. On the contrary, in-plane polarization exhibits the opposite trend.

Moreover, Fig. 6.13 b) shows the dependence of the polarization calculated by Berry phase method on epitaxial strain. The maximum values of the polarization are close to 40 μCcm^{-2} for out-of-plane polarization under -3% of compressive strain and in-plane polarization for +3% of tensile strain. These polarization values are comparable with those estimated by Berry phase formalism for (111) epitaxially strained $BaTiO_3$ (P_s=25 μCcm^{-2}) and lower than $PbTiO_3$ (P_s=80 μCcm^{-2}).

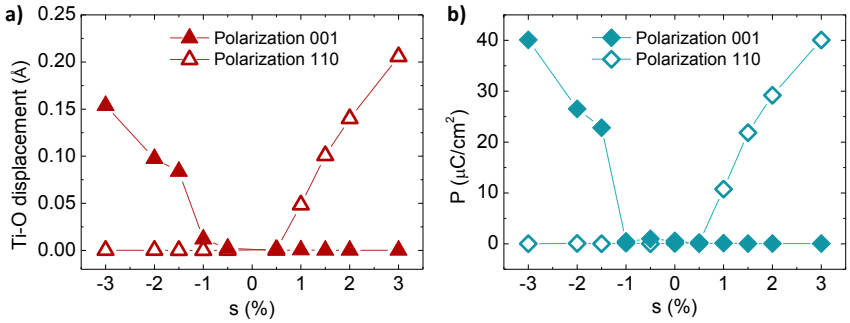

Figure 6.13: Relative Ti-O displacement (a) and polarization (b) as a function of strain determined for the relaxed structures, for the out-of-plane and in-plane polarizations. The spontaneous polarization were calculated using the Berry phase method, taking the difference between a paraelectric structure ($SrTiO_3$ unit cell without any distortions) and the ferroelectric structures after the relaxation.

The next step is considering space groups with distinct octahedral tilting and polarization direction, in search of the ground state and the complete phase diagram of the stoichiometric system. The space groups used are summarized in Table 6.2, following the notation of Stokes $et\ al$ [201]. This notation expresses in a compact way both the tilt system and the distortion caused by the displacement of the cations. The superscripts denote the octahedra tilts, while the subscripts $+$ and $-$ mean ferroelectric B-cation (Ti in this case) displacements along a given axis. The space group with the rotations observed in the STO below 105 K (i.e. $a^0a^0c^-$) is among the phases studied, considering the polarization in the [110] and [100] directions. Furthermore, the structure that represents the octahedral rotation pattern experimentally observed for compressive strain is chosen ($I4mmm$), considering in-plane polarization ($I4mm$) and out-of-plane polarization ($Fmm2(II)$). Space groups $Fmmm$ and $Ima2(II)$ with rotations out-of-phase around the in-plane axes are included for comparison.

The total energies of the superlattices with different symmetries are calculated varying the strain from -2% to +2% (Fig. 6.14). The lattice parameters used are those previously optimized using PBESol

Space group	Rotations	Polarization	System	Nº atoms
I4/mcm	$a^0a^0c^-$	000	$a_0^0a_0^0c_0^-$	20
Ima2	$a^0a^0c^-$	pp0	$a_+^0a_+^0c_0^-$	20
Fmm2	$a^0a^0c^-$	p00	$a_+^0a_0^0c_0^-$	40
Fmmm	$a^-a^0c^0$	000	$a_0^-a_0^0c_0^0$	40
Ima2(II)	$a^-a^-c^0$	pp0	$a_+^-a_+^-c_0^0$	20
I4mmm	$a^+a^+c^0$	000	$a_0^+a_0^+c_0^0$	40
I4mm	$a^+a^+c^0$	00p	$a_0^+a_0^+c_+^0$	40
Fmm2(II)	$a^+a^+c^0$	pp0	$a_+^+a_+^+c_0^0$	40

Table 6.2: Space groups considered in this Section. The principal characteristics of these phases are also indicated: octahedral rotation pattern around the pseudocubic axes, Cartesian coordinates of the polarization vector and the atoms that composed the supercell in each case.

functional (see Fig. 6.12), which are closest to the experimental results. In absence of strain, the ground state is the non-polar $I4/mcm$ phase, which represents the structure of STO at low temperatures, overlapping in energy with the polar structures with the same octahedral rotation pattern ($Ima2$ and $Fmm2$) and the space groups $Fmmm$ and $Ima2(II)$ with out-of-phase and in-plane rotations. However, the structures observed experimentally are less stable, having higher energy.

In addition, the variation of the rotation angles also shows a trend with strain. Space groups with out-of-plane tilts increase the degree of rotation for compressive stress and decrease for tensile strains. By contrast, space groups with $a^+a^+c^0$ present the opposite trend, meanwhile $Fmmm$ and $Ima2(II)$ phases do not show appreciable variations in the range of strains studied (see Fig. 6.14 b).

For compressive strain, the phase diagram splits in three branches with clearly differentiated energies, each of them containing the systems with the same rotation pattern regardless of whether they are polar or non-polar. The space groups with $a^0a^0c^-$ configuration are the most stable. Then, the symmetries with out-of-phase and in-plane rotations

($Fmmm$ and $Ima2(II)$) are higher in energy (about ≈30 meV) with respect to the first ones. And lastly, the group of the phases with $a^+a^+c^0$ are the least favourable configuration among those studied, although this is the configuration experimentally observed. Therefore, the octahedral configuration seems to play a major role, being quite difficult to stabilize a tilt system different from $a^0a^0c^-$ under compressive strain.

The situation for tensile strains is completely different. $Ima2(II)$ is the most stable phase for all the range of positive strain studied. However, the other phases are very close in energy, despite of them being less stable, and well-defined branches cannot be observed as in the case of compressive stress. This remarkable result indicates the existence of phases with very similar energy, suggesting that metastable phases could exist in the phase diagram for tensile strain. Therefore, the properties of the samples under positive stress could be very sensitive to growth conditions and also to the octahedral rotation pattern imposed by the substrate, which coincides with experimental observations.

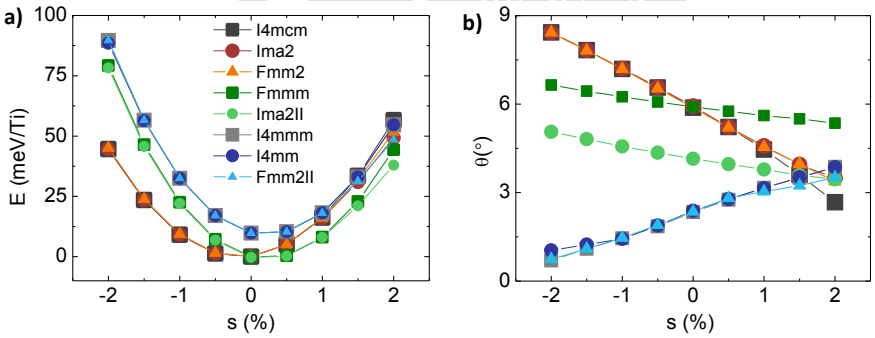

Figure 6.14: a) Free energy of the different phases considered in this Thesis and detailed in Table 6.2 as a function of strain. The energy of high-symmetry $P4/mmm$ phase is taken as reference. b) Average rotation angles determined after the relaxation for the space groups considered in this Section. The angles are determined for the axes around which octahedral rotation exists in each space group. The legend is common to both panels.

After the atomic relaxation, the total polarization was estimated by

using either BEC and Berry phase method. The results obtained with BEC are shown on Fig. 6.15. For clarity, the space groups are separated in 3 groups, which possess the same rotations although different initial polarization directions. The first group characterized by the $a^0a^0c^-$ rotation pattern exhibit in-plane polarization for tensile strain (Fig. 6.15 a)), similar result is obtained for the second group ($Fmm2$ and $Ima2II$, Fig. 6.15 b).

Nevertheless, the third group, which is composed of the symmetries with the rotations observed experimentally ($a^+a^+c^0$), shows polarization for both compressive and tensile strain. Under tensile stress, the symmetry denoted as $Fmm2(II)$ preserves the in-plane polarization, whereas the $I4mm$ ($a_0^+a_0^+c_+^0$) symmetry is the only one that can stabilize the spontaneous polarization for compressive strain (out-of-plane polarization). The latter result is completely in agreement with the experimental evidences, which point out to the appearance of a FE response only for samples with the $a^+a^+c^0$ octahedral configuration. Moreover, these results are in accordance with other studies already reported in the literature for STO [202, 203], which consider some of the space groups studied in this Thesis.

The ferroelectric instability of perovskite compounds is dependent on the volume and more generally strongly affected by strain. Since ferroelectricity is a collective phenomenon, when an atom is displaced from its position, it feels a force that tries to brings it back to its initial position. Moreover, when the volume is reduced, the ferroelectric instability is progressively suppressed. For this reason, it is very difficult to retain the polarization for compressive strain.

It is worth noting that despite of the high distortion imposed to the different space groups due to the large negative or positive strain, the symmetry after the relaxation is conserved in all the cases studied. This was verified using the free software ISOCIF [204].

Since the BEC method often fails to provide numerical values in agreement with those reported experimentally, the spontaneous polarization has also been estimated by means the Berry phase method, which is based on a more sophisticated theoretical scheme and gives more accurate results compared to experiments [205–207].

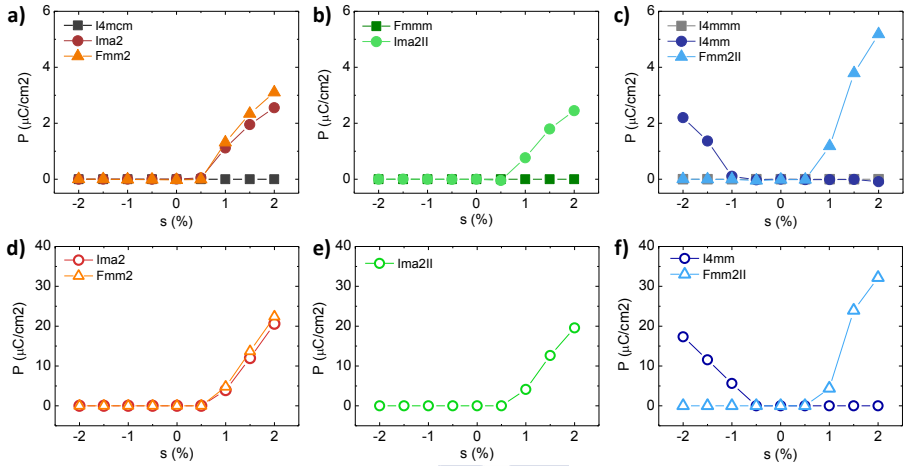

Figure 6.15: Spontaneous polarization estimated by BEC (a-c) and Berry phase approach (d-e) for the symmetries studied in this Section. The results are grouped by space groups with similar rotations but different initial polarization, a, d) $a^0a^0c^-$ octahedral configuration, b, e) $a^-a^0c^0$ or $a^-a^-c^0$ and c, f) $a^+a^+c^0$ pattern.

Despite of the problems of the BEC method to provide accurate numerical values, the trend predicted by this model is reliable, so that only symmetries and strains that already exhibited polarization by the BEC method were also studied through the Berry phase formalism. The results are shown on Fig. 6.15 d-f), the values for 2% tensile strain ranging from ≈20 to ≈33 μC/cm^2 and for compressive strain values of ≈17 μC/cm^2 for -2% of strain and ≈10 μC/cm^2 for -1% are obtained.

These values are slightly higher than other experimentally reported, for example, in $SrTiO_3$ ultrathin films deposited on Si (001) (P∼9 μC/cm^2) [208] and comparable with the value of ∼20-30 μC/cm^2 for the $BaTiO_3$ [200,209], which is the exemplary room temperature ferroelectric. However, the values of the spontaneous polarization are far from those of other typical ferroelectric materials, such as $BiFeO_3$ (P∼80-100 μC/cm^2) [210–212] or $PbTiO_3$ (P∼70-80 μC/cm^2) [200].

The results can be summarized in the phase diagram shown in Fig. 6.16, from which two main conclusions can be extracted: i) tensile strain favours in-plane polarization along the direction [110] (or [100],[010]) for several symmetries with different octahedral rotation patterns. In-plane polarization is not observed in any case under compressive strain; ii) out-of-plane polarization can only be stabilized under compressive strain and for the symmetry with $a^+a^+c^0$ octahedral configuration, which is completely in agreement with the experimental observations of the previous Section. Therefore, we can conclude that octahedral rotations could be the key factor to stabilize out-of-plane polarization in STO under compressive strain.

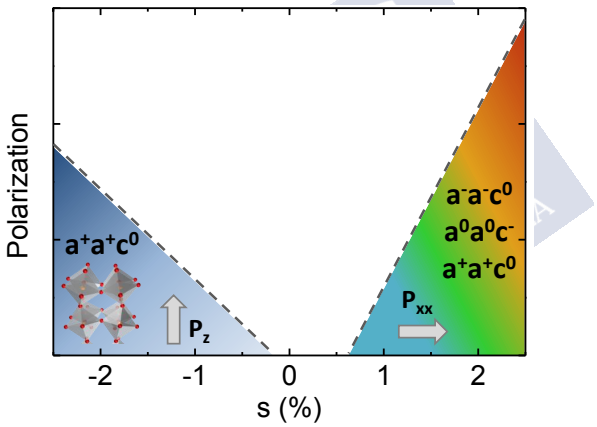

Figure 6.16: Phase diagram summarizes the results of the simulations for the different space groups considered in this Thesis. Compressive strain only stabilizes out-of-plane polarization with the $a^+a^+c^0$ rotation pattern, however several octahedral configurations can exhibit in-plane polarization for tensile stress. Arrows indicate the direction of the polarization.

6.2.2 Oxygen vacancy influence on the polarization: ab-initio calculations

Once the effect of the different rotation patterns on the ferroelectric response was examined, we introduce an oxygen vacancy in the simula-

tions to study the interplay between rotations, strain, defects and FE. In ferroelectric materials, there is a delicate balance between the short-range repulsion, which favours the non-polar structure and the long-range Coulomb interaction which favours the ferroelectric state. Free carriers, as those donated by the oxygen vacancies, can screen out the long-range Coulomb interaction, reducing the polar distortion. Unfortunately, the most oxygen-deficient systems present a metallic band structure where both the Born effective charge calculation and Berry phase method fail [213]. Nevertheless, in practical ferroelectrics, polarization still exists in spite of the inevitable presence of oxygen vacancies and the material being semiconductor or insulator.

The idea of our approach here is to demonstrate that the combination of rotations and oxygen vacancies may give rise to a polar distortion. To demonstrate this premise, the simulations in this Section were performed for all the space groups studied previously. As starting structures we took those already relaxed in the previous Section, and a new relaxation was carried out introducing a vacancy in each symmetry. Furthermore, two scenarios were considered to explore the influence of the vacancy site on the energetics: one with an apical oxygen vacancy and other with an equatorial one. In addition, the unit cells were doubled with respect to those used in the previous Section to ensure a concentration of oxygen vacancies similar to experiments and test the long-range distortions caused by the presence of an oxygen vacancy. Thus, the cells with 20 and 40 atoms were doubled until reach 40 and 80 atoms, respectively (oxygen concentration of 2% and 4%). The k-mesh was adjusted for the supercells of 40 and 80 atoms to $4\times4\times4$ and $3\times3\times4$, respectively.

In general, removing an oxygen atom from the lattice pushes the cations (Sr and Ti) away from the vacancy and attracts the anions (O), to redistribute the charge and minimize the forces. The results of the relative energies of all the space groups as a function of strain after the atomic relaxation are shown in Fig. 6.17. As a general trend, under tensile stress, the effects of an apical or an equatorial oxygen vacancy are not reflected in the total energy, presenting a very close energy for both phases or even being indistinguishable the effect of the vacancy

site in some cases.

For large compressive strains the energies of the phases with an apical or an equatorial vacancy are different in all cases. Interestingly, the structure with an equatorial oxygen vacancy is always more stable than an apical vacancy for all the space groups, with a larger difference for the space groups with $a^+a^+c^0$ rotations. These results demonstrate that an equatorial vacancy is always more favourable for compressive strain. Furthermore, it is also worth mentioning that independently of the space group (and hence of the rotations) the structure with the vacancies is always more stable for tensile stress than compressively strained one.

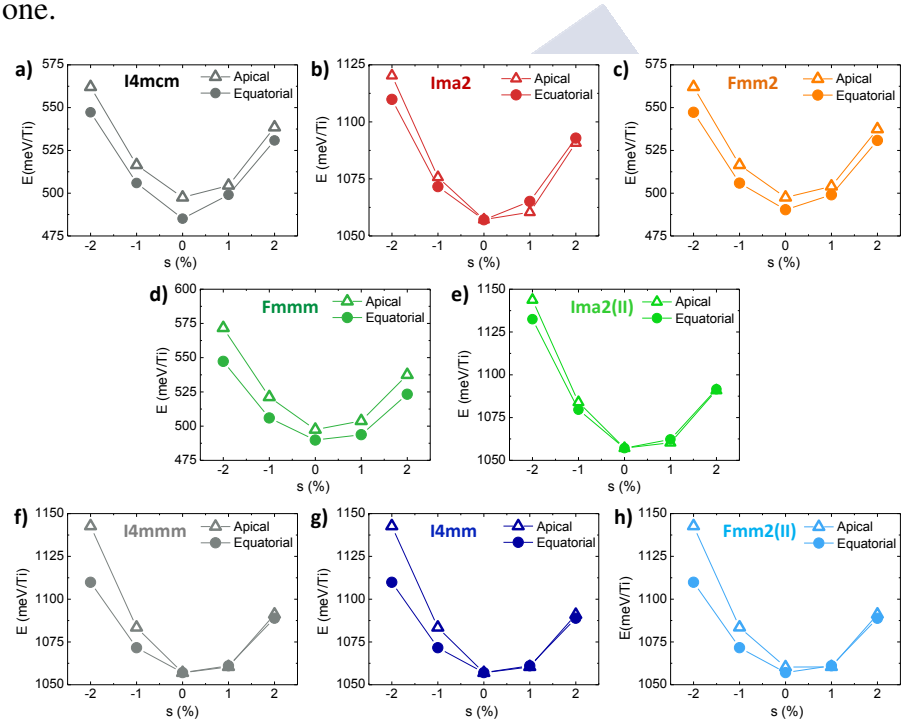

Figure 6.17: Total energy as a function of strain for the space groups considered with two distinct oxygen vacancy sites, apical and equatorial. a-c) Space groups with $a^0a^0c^-$, d) $a^-a^0c^0$, e) $a^-a^-c^0$ and f-h) $a^+a^+c^0$ rotation patterns.

As mentioned before, the presence of vacancies in the structures

turns the system conducting and both Berry phase and BEC produce unreliable results. Alternatively, a quantitative analysis of the atomic displacements based on the symmetry-modes and their relative amplitudes is equally valid to detect polar distortions [214–216]. This analysis consists in the comparative between high and low symmetry phases, determining the atomic displacements that relate them and calculating the amplitudes and polarization vectors of the distortion of different symmetry frozen in the structure.

Distorted structures are often related to their higher-symmetry structure by different phase transitions, among which ferroic phase transitions are those of interest in this study. The presence of these polar modes indicates a polar distortion in the relaxed structure that can lead to the ferroelectric-like response observed experimentally. The analysis was performed using the free software available on the Bilbao Crystallographic Server called AMPLIMODES [217]. $P4mmm$ high-symmetry structure, which does not present any rotations or distortions, was used in all the analysis as the reference structure.

The decomposition mode analysis performed to the phases with an apical or an equatorial vacancy is shown in Fig. 6.18, in which the amplitude of the polar mode ($\Gamma5^-$) is represented. This is the only polar instability obtained in the analysis. Other modes corresponding with strain ($\Gamma1^+$) and rotations (A5^+, A1^-, M3^+, etc.) are present when performing the analysis but are not considered here since they are not polar and therefore cannot be the source of the polar distortion observed experimentally. Under the light of the results, it is clear that the $\Gamma5^-$ polar instability develops in some phases by introducing oxygen vacancies in the simulations.

In the $I4/mcm$ phase no polar distortion appears independently of the presence of vacancies, and the same is true for $Ima2$ when an equatorial vacancy is introduced (Fig. 6.18 b). This phase shows polar instability for positive stress with an apical vacancy, which is a similar result to that obtained in the previous Section without the presence of oxygen vacancies. Similarly, $Fmm2$ also exhibits the same behaviour with an apical vacancy, but in addition the polar instability for an equatorial vacancy appears under compressive strain and it is suppresed as

the strain becomes positive (Fig. 6.18 c).

In the phases with $a^+a^+c^0$ rotation pattern (Fig. 6.18 f-g), the polar mode emerges independently of the vacancy site. Both $I4mmm$ and $I4mm$ present similar values and trends of the amplitude of $\Gamma 5^-$ mode as a function of strain, showing a maximum for compressive stress and decreasing as the strain becomes positive, indicating that, as seen in the previous Section, compressive strain favours the observation of polar distortion for this particular rotation pattern. Nevertheless, although $Fmm2(II)$ presents the same tendency with strain as the other phases with similar rotations, the amplitude of the $\Gamma 5^-$ instability gives the same value independently of the vacancy site.

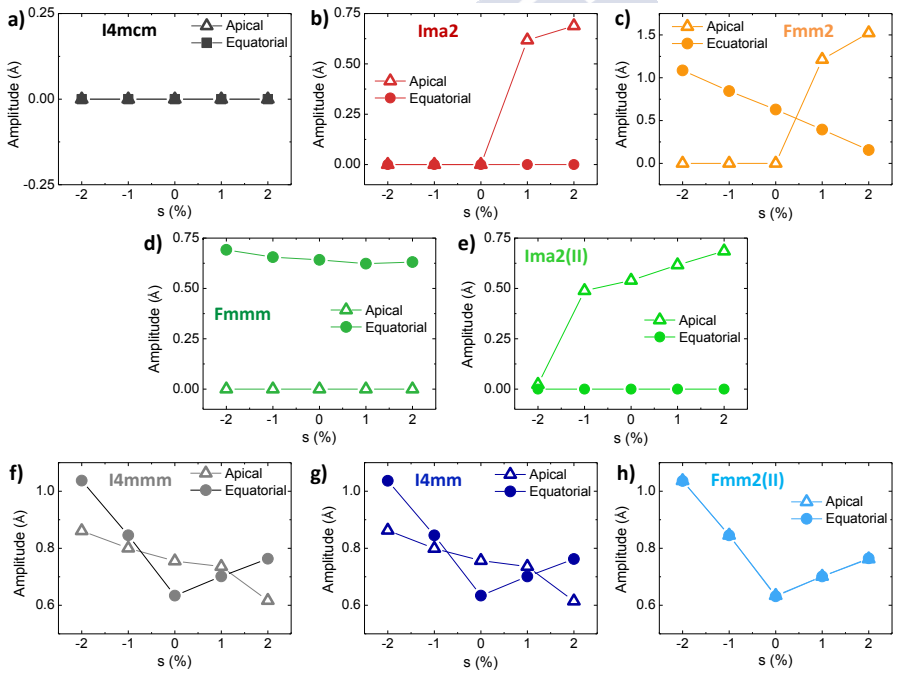

Figure 6.18: Amplitude of the $\Gamma 5^-$ polar mode as a function of strain for the space groups considered with two distinct oxygen vacancy sites, apical (open triangles) and equatorial (solid circles). a-c) Space groups with $a^0a^0c^-$, d) $a^-a^0c^-$, e) $a^-a^-c^0$ and f-h) $a^+a^+c^0$ rotation patterns.

In conclusion, the results obtained from the simulations confirm that the rotation pattern $a^+a^+c^0$ determined for thin films grown under compressive strain favours an out-of-plane polarization (see Fig. 6.15) and, in addition, the introduction of oxygen vacancies stabilizes this polar distortion, which is in agreement with the experimental observations and points out to an interplay between a particular octahedral configuration and oxygen vacancies to cause a ferroelectric response in the STO films.

6.3 Summary

We have found the films grown under the same conditions on top of different substrates (some of them with distortions) exhibit distinct configurations of the cooperative octahedral rotations depending on the strain and the rotations of the substrate underneath. Even samples without strain grown on top of cubic undistorted STO substrate present octahedral rotations compatible with $I4mmm$ ($a^+a^+c^0$) space group, which suggest a major role of the defects in producing them.

In this Chapter, we performed DFT simulations to unravel the effect of strain and defects on the octahedral rotation patterns observed experimentally. Strain is responsible of the octahedral configurations determined for positive and negative stress. Meanwhile, the cause of the rotations in the films without strain seems to be related with the presence of cationic defects, which produce an effect similar to the decrease of the tolerance factor.

On the other hand, we observed experimentally a FE-like response in thin films grown under compressive strain, and presenting a rotation pattern of the type $a^+a^+c^0$. Moreover, this local ferroelectricity only emerges when the sample possesses a high concentration of oxygen vacancies, indicating the possibility of a coupling between rotations and oxygen vacancies. In order to prove this assumption, we carried out ab-initio calculations considering several space groups with diverse distortions and polarization directions. Among the studied groups, only the space group with the $a^+a^+c^0$ rotations stabilizes a spontaneous out-

of-plane polarization under compressive strain. This demonstrates that a particular octahedral configuration could promote the stabilization of the polarization. Additionally, the effect of oxygen vacancies was added, also performing simulations that considers distinct vacancy sites, apical or equatorial. The results show the existence of a polar mode in the space groups with the $a^+a^+c^0$ pattern, whose amplitude is maximum for compressive strain and decreases when the strain becomes positive.

The results of the simulations point out in the same direction as the experimental observations, meaning that the rotations could be coupled with the oxygen vacancies to induce a polar distortion under compressive strain, which gives a response similar to a FE material. Despite the fact that our analysis has been focused on STO polarization, the coupling between rotations, strain and oxygen vacancies demonstrated here could be extended to other perovskites as a general rule to achieve controllable ferroelectricity in thin films.

7. Transport properties of strained $SrTiO_3$ thin films

Women are not going to arrive, they are here.

Margarita Salas, researcher in Biochemistry and Molecular Genetics. A pioneer woman researcher in Spain.

As discussed in the previous chapters, the presence of (a considerable amount of) ionized oxygen and cationic vacancies plays a very important role in the stabilization of epitaxial stress in $SrTiO_3$ thin films, as well as on the ionic/electronic conductivity and ferroelectric polarization of this material.

Hall effect measurements discussed in Chapter 4 showed an increasing amount of free electrons as oxygen pressure decreases, both during deposition or in post-deposition high temperature annealing. We have established that oxygen vacancies donate two electrons to the conduction band of STO, so that this increase in carrier density is undoubtedly related to an increasing amount of oxygen vacancies.

An important question is whether part of these electrons remain localized forming well defined local magnetic moments at the Ti^{3+} (d^1) sites. This is crucial, given the rich magnetotransport phenomenology observed in conducting LAO/STO interfaces [7–9] and $LnTiO_3$/STO/ $ATiO_3$ (A=Sm, Gd) magnetic quantum wells [218], including the char-

acteristic low temperature upturn in the electrical resistivity of the 2DEG at the (001) LAO/STO interface, which is commonly associated to Kondo effect [219, 220].

In this regard, Rice et $al.$ [221] observed the emergence of a net magnetic moment in oxygen-deficient STO crystals below T≈18 K, after irradiation of the crystal with polarized light (λ =405 nm). The optically induced magnetization persisted for hours below 10 K, and only occurs in crystals containing oxygen vacancies, demonstrating the coupling between magnetism and ionic defects in STO.

On the other hand, a Kondo-like phenomenology was also reported in electrolyte-gated STO crystals, which suggests that this effect (whether it is Kondo effect or not [222]) may be related to the interaction between the conduction electrons and the local Ti^{+3} moments inevitably associated to the presence of oxygen vacancies in $SrTiO_3$ [223].

Therefore, a deeper understanding of the effect of oxygen vacancies in the magnetotransport properties of STO thin films becomes very important, in particular with the aim to elucidate the role of defects on the phenomenology observed in the LAO/STO interface [5, 157, 224, 225].

In this Chapter we will describe the main results of our study of the magneto-transport properties of the STO thin films fabricated under different conditions. The resistivity and magnetoresistance of the films under different degree of epitaxial strain is discussed, as well as the possible existence of Kondo effect and other alternative possibilities to explain this interesting phenomenology.

7.1 Out-of-plane magnetoresistance

In 2010, Caviglia $et\ al.$ [226] reported the observation of Rashba effect in the 2DEG confined at the (001) LAO/STO interface. The lack of interfacial inversion symmetry of the heterostructure originates a large electric field (E) perpendicular to the plane in which the 2DEG is restricted to move. As a result, the conducting electrons will experience a magnetic field (the spin-orbit field, $B = E \times p/mc^2$) which couples to its spin (the spin-orbit coupling), and produces a splitting of the bands

at the Fermi energy (E_F) for opposite spin momentum. What is very interesting is that because the strength of the Rashba spin-orbit coupling depends on the electric field at the interface, it can be tuned through a voltage in a field-effect transistor configuration. Using this approach, Caviglia *et al.* [226] as well as Ben Shalom *et al.* [227] tuned the spin-orbit interaction in the 2DEG until it condenses into a superconducting state below ≈0.3-0.4 K. This was a remarkable discovery, and suggested an unconventional order parameter related to some type of spin fluctuations to explain superconductivity in STO, like in heavy-fermion superconductors [228, 229].

However, it must be remembered that superconductivity was already reported in oxygen deficient $SrTiO_3$ in 1964 by Schooley, Hosler, and Cohen [69]. Later on, Baratoff and Binning observed the simultaneous reduction of T_c and the contribution of the longitudinal-optical (LO) phonon modes to the resistivity of Nb:STO [230], and suggested the main role played by polar modes in the superconducting state of this oxide. Recent experiments in strained thin films of (La,Sm):$SrTiO_3$ reinforced the conclusion of a proximity between a ferroelectric and a superconducting phase in e-doped STO [231].

But more importantly, irrespective of the nature of the superconducting state, it has been demonstrated that lightly e-doped (oxygen deficient) STO shows a T_c≈0.25 K-0.6 K, very similar to the superconducting critical temperatures reported for E-gated LAO/STO interfaces.

In Chapter 5 we showed how a local electric field may modulate the local concentration of oxygen vacancies and therefore, the local electrical conductivity. The effect of an electric field applied to the interface in a field-effect transistor configuration, may therefore modify the local concentration of oxygen vacancies, which accumulate at the interface to the concentration required to form the superconducting state. The effect of the electric field in this scenario will be to change the local electron-density, moving T_c across the superconducting dome reported by other authors in oxygen deficient STO [230]. In view of this possibility, the origin of the superconducting state and the conclusions about the role of Rashba spin-orbit coupling in the transport properties of LAO/STO interfaces should be revised.

To probe this hypothesis, we measured the electrical resistance and charge density (n) as a function of temperature for a series of samples with different thicknesses deposited on LAO and LSAT ($s = -1.15\%$ and $s = -0.95\%$, respectively), as can be seen in Fig. 7.1.

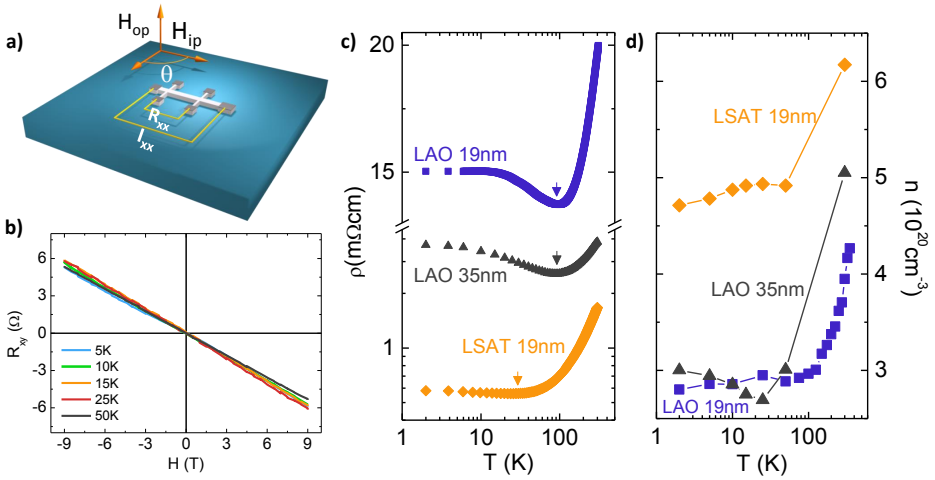

Figure 7.1: a) Sketch of the set-up used to measure the resistivity and the magnetoresistance of the samples, with the magnetic field applied in-plane (H_{ip}) or out-of-plane (H_{op}). θ indicates the angles between the in-plane magnetic field and the current that flows along the Hall bar. b) Hall resistance for the 19 nm film grown on LAO, at different temperatures. c) Temperature dependence of resistivity and d) carrier density, for thin films on LSAT and LAO. The thickness of each film is indicated in c) and d). The arrows in c) indicate the temperature of the resistivity minimum (T_{min}).

The temperature dependence of the resistivity exhibits a metallic-like behavior at high temperature ($T>T_{min}$), with an increasing number of carriers as temperature increases, which suggests a thermally activated contribution. At low temperatures ($T<T_{min}$), the resistivity shows an upturn similar to a Kondo effect, irrespectively of the substrate and/or thickness of the sample.

Since the samples were deposited side-by-side, a similar density of oxygen vacancies is expected a priori. However, the larger carrier

density and smaller rise of the resistivity in the film deposited on LSAT suggests a smaller density of defects in this sample, with respect to those grown on LAO.

In this regard, Bergmann [232, 233] showed that the resistance of two-dimensional electronic conductor shows deviations from classical conductivity (Drude formula) caused by quantum corrections. This effect due to interference of self-crossing trajectories between random scattering events, resulting in an increased resistivity, the so-called Weak Localization (WL) effect [234]. Given that the probability of these self-crossing trajectories decreases as dimensionality increases, the WL contribution is more relevant in the conductivity of thin films. Also, the disorder created by the presence of oxygen vacancies would act as random scattering sites, resulting in a diffusive rather than ballistic propagation of the electrons in the system. Inelastic electron-electron ($e-e$) or electron-phonon ($e-ph$) scattering also reduce the number of coherent scattering events, and therefore, the number of loops contributing to WL. The total change in the conductance due to WL, taking into account the inelastic scattering time τ_i is therefore [234]:

$$\frac{\Delta\sigma^{WL}}{\sigma} \propto ln\left(\frac{\tau_e}{\tau_i}\right) \tag{7.1}$$

where τ_e is the elastic scattering time. What is important for our discussion is that the time-reversed paths of WL are a consequence of preservation of the time reversal symmetry. Therefore, the application of a perpendicular magnetic field B that breaks this symmetry also reduces the probability of WL, and restores partially the conductance (positive magnetoconductance).

On the other hand, the presence of a strong spin-orbit coupling modifies completely this picture: the spin of the diffusive electron rotates and randomizes as it travels around the self-intersecting trajectories, which leads to destructive interferences. This is the so-called Weak Anti-localization (WAL) effect. In this case, a perpendicular B suppresses this positive contribution, and therefore decreases the conductance (negative magnetoconductance).

Thus, taking all these contributions to σ into account, the shape of

the magnetoconductance curves at a given temperature depends on the relative magnitude of their characteristic relaxation times, τ_i, τ_e and the spin-orbit scattering time (τ_{so}) (see Fig.7.2).

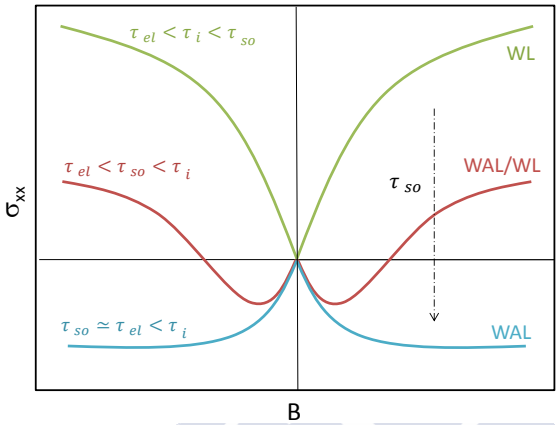

Figure 7.2: The electrical conductance for a ≈2D conductor as a function of the applied magnetic field. Three regimes can be observed depending on the relative value of the different scattering times: i) for $\tau_e<\tau_i<\tau_{so}$, WL dominates showing positive conductance (green curve); ii) for $\tau_e<\tau_{so}<\tau_i$, crossover between WL and WAL regimes, i.e. a negative conductance appears at low field followed by a positive one at higher fields (red line); and iii) for $\tau_{so}\simeq\tau_e<\tau_i$, dominating WAL results in a negative conductance in the whole range of B (blue line).

We measured the electrical resistance ($1/\sigma$) at different temperatures under the influence of an increasing perpendicular magnetic field for a series of 19 nm-thick films deposited on LSAT and LAO. The experimental results are shown in Fig. 7.3. For better comparison with the theory, we present the results of the magnetoconductance (MC), which is defined as follows:

$$MC = \frac{\delta\sigma(B)}{\sigma_0} = \frac{\delta\sigma(B)}{\frac{e^2}{\pi h}} \tag{7.2}$$

where σ_0 is the quantum of conductance and $\delta\sigma(B)$=$\sigma(B)$-$\sigma(0)$.

The sample grown on LSAT shows a completely positive MC; only small hints of negative values can be seen at the very lowest fields, which are within the error of the measurement (see Fig. 7.3 a). This is consistent with WL effect with a weak spin-orbit coupling (see also Fig. 7.2). On the other hand, the sample deposited on LAO exhibits a negative cusp at low magnetic fields (<3 T), which is a characteristic feature of WAL effect. This cusp is more pronounced at low temperatures and disappears as the temperature increases (see Fig. 7.3 b). Hence, this sample shows a crossover between WAL and WL regimes, suggesting an increasing spin-orbit coupling with respect to the film deposited on LSAT.

Rashba spin-orbit coupling produces a magnetic field perpendicular to the direction of the motion of the electrons. If the spin of the electron is not aligned with this internal magnetic field, it precesses at a given frequency, ω_L. This is the origin of the Dyakonov–Perel spin-relaxation, in which the spin relaxation time varies inversely with the elastic scattering time ($\tau_{SO} \propto 1/(\omega_L \tau_e)$ [235].

On the other hand, impurities and/or vacancies with an associated net magnetic moment can also act as spin-orbit scattering centers, leading to a spin-flip which is characterized by a relaxation time proportional to the elastic scattering ($\tau_{SO} \propto \tau_e$) [236]. This is the so-called Elliot-Yafet spin-orbit relaxation.

We obtained the different scattering times in our samples from the fitting of MC curves to the equation proposed by Hikami-Larkin-Nagaoka (HLN) for quasi 2D systems [237]:

$$\begin{aligned} \Delta\sigma = & -\frac{e^2}{2\pi h}\left[\Psi\left(\frac{B_i}{B}+\frac{1}{2}\right) - ln\left(\frac{B_i}{B}\right)\right] \\ & -\frac{e^2}{\pi h}\left[\Psi\left(\frac{B_{so}+B_e}{B}+1/2\right) - ln\left(\frac{B_{so}+B_e}{B}\right)\right] \\ & +\frac{3e^2}{2\pi h}\left[\Psi\left(\frac{(4/3)B_{so}+B_i}{B}+\frac{1}{2}\right) - ln\left(\frac{(4/3)B_{so}+B_i}{B}\right)\right] \end{aligned} \tag{7.3}$$

where B_i, B_e and B_{so} are the inelastic, elastic and spin-orbit effec-

tive fields, respectively. They are directly related to τ_i, τ_e and τ_{so} by the expressions:

$$B_n = \frac{\hbar}{4eD\tau_n} \tag{7.4}$$

where D is the diffusion constant and the indices $n = e, i, so$ have their usual meaning.

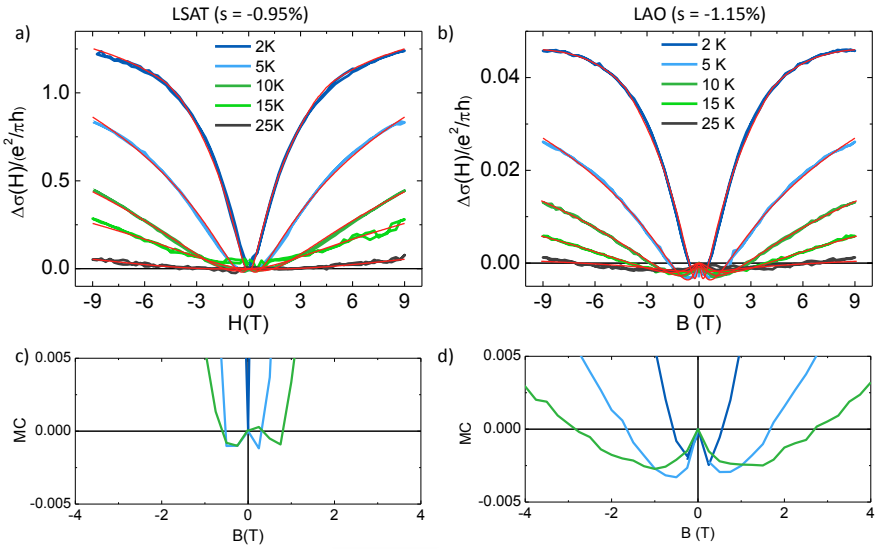

Figure 7.3: Magnetoconductance of Nb:STO epitaxial thin films on top of LSAT a) and LAO b). The magnetic field is applied perpendicular to the film plane. Figs. c) and d) show an enlargement of the curves at low magnetic fields. The thickness of the films is 19 nm in both cases. The experimental epitaxial strain is indicated in each case. Red lines represent the fittings according to Eq. 7.3.

The fitting of the experimental data to Eq. 7.3 is very satisfactory in the entire range of fields up to 9 T; see Fig. 7.3. The values of the different scattering times obtained from these fits are shown in Fig. 7.4.

The values of the scattering times confirm the conclusions extracted from the shape of the MC curves. For the film grown on LSAT (with a

lower concentration of defects), $\tau_e < \tau_i < \tau_{so}$, indicating the existence of WL effect in all the range of magnetic fields and temperatures (see Fig. 7.4 a). In this case, τ_{so} is at least one order of magnitude higher than τ_e and τ_i, which points out to a weak spin-orbit coupling in the system.

Nevertheless, the value of the different scattering rates is more similar in the case of the sample grown on LAO (see Fig. 7.4 b). In this case, τ_{so} shows the same order of magnitude as τ_i, which evidences the existence of a stronger spin-orbit interaction. These values are compatible with the observed crossover between WAL and WL regimes in the low-field magnetoconductance.

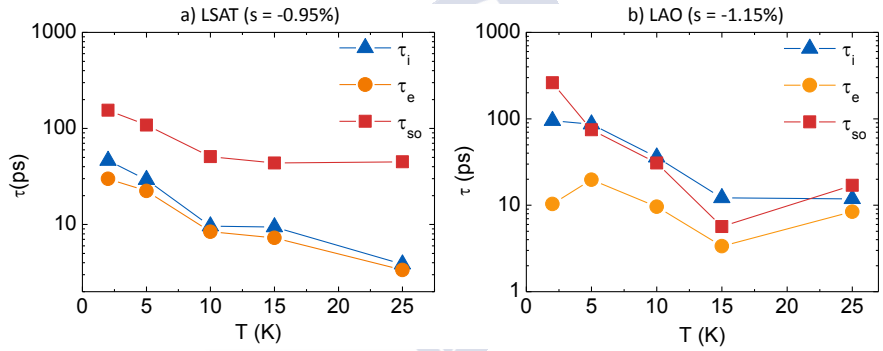

Figure 7.4: Different scattering times as a function of temperature extracted from the fitting using Eq.7.3 for the films deposited on LSAT a) and LAO b).

Moreover, plotting τ_{so} versus τ_e shows a direct proportionality relationship (Fig. 7.5), which is a strong evidence of the existence of Elliot-Yafet mechanism for spin-relaxation in the STO thin film deposited on LAO. This points out to the local magnetic moments at the Ti^{3+} as the source of the spin-orbit coupling in this system.

Therefore, the proposed tunable Rashba effect and superconductivity observed by other authors [226, 238, 239], could be a misinterpretation of the effect of the electric field over the local concentration of (highly mobile) oxygen vacancies (and the associated spin-orbit coupling effect discussed in this Section).

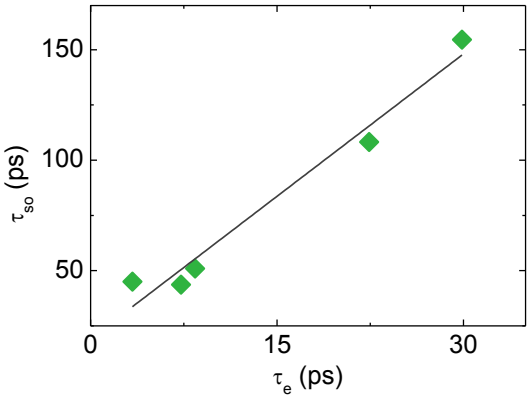

Figure 7.5: Spin relaxation time vs elastic scattering time showing linear dependence consistent with Elliot-Yafet mechanism. The grey solid line represents the linear fitting.

In the next Section, we will investigate the origin of the low temperature upturn in the resistivity. Looking at $\rho(T)$ in Fig. 7.1 c), Kondo-like behavior is more evident in the films with more vacancies and increases as the thickness decreases. Given the discussion before, the effect of vacancy scattering (precursor of Anderson localization) close to the interface or surface, must be investigated. For that we have measured the $\rho(T)$ and in-plane anisotropic magnetoresistance for different amounts of strain/disorder, and the discussion is presented below.

7.2 Temperature dependence of the electrical resistivity: effect of strain and defects

Defects have a profound effect in the transport properties of a solid, particularly on the electrical conductivity of a metal or semiconductor. According to the Bloch theory, an electron moving in the periodic potential created by a perfect ionic lattice will not experience any collision. But the presence of defects (in the form of impurities, substitutions or vacancies) introduces imperfections in this potential, leading to collisions and scattering events which contribute to the magnitude and tempera-

ture dependence of the electrical resistivity ρ (T) of the conductor. Of course, there exit other sources of deviation from the periodic potential of the lattice, such as thermal vibrations of the ions, as well as other inelastic scattering events like $e-e$ interactions [240]. The different terms that contribute to ρ (T) will be considered independently of each other (Matthiessen's rule [241]), so that in the relaxation time approximation [242]:

$$\rho = \frac{m^*}{ne^2}\frac{1}{\tau} = \frac{m^*}{ne^2}\sum_{i=1}^{n}\frac{1}{\tau^n} \tag{7.5}$$

where m* is the electron mass, n is the charge carrier density, e is the electron charge and τ represents the average time between scattering events, in which all the possible sources of scattering are included.

At low temperatures, few phonons are excited, so that the $e-e$ interaction and localized impurities are the main source of scattering, contributing with the characteristic Fermi-liquid $\sim$T^2 term [243] and a temperature independent term (ρ_0), respectively. The latter term is the so-called residual resistivity due to the scattering by impurities, defects or vacancies within the crystal lattice [234].

When temperature increases, there is an increase in the density of phonons, and, therefore, in the probability of $e-ph$ scattering. Thus, the resistivity is mainly governed by the scattering of electrons by the lattice vibrations. At high temperatures, well above the Debye temperature (Θ_D), the Bose-Einstein distribution tends to $k_BT/h\omega(q)$, so that the number of phonons (and therefore the $e-ph$ scattering probability) increases linearly with temperature. This leads to a ρ(T)$\propto$T, at T$>>$ Θ_D. However, at lower temperatures, T$<<$ Θ_D, the phonons participating in the scattering events suffer certain restrictions about the ratio between their wavelength and the Fermi wavevector (only phonons with energies around k_BT of the Fermi energy can be absorbed or emitted by electrons), resulting in a faster variation of the resistivity with temperature. So in this regime, ρ(T)$\propto$T^5 [244–246].

Given that Θ_D(STO)$\sim$690 K [247], and the considerations above, the temperature dependence of electrical resistivity is expected to vary

as:

$$\rho(T) = \rho_0 + AT^2 + BT^5 \tag{7.6}$$

where A and B are the coefficients of $e-e$ and $e-ph$ scattering terms, respectively.

The experimental results of $\rho(T)$ for $SrTiO_3$ films under different degrees of epitaxial strain are summarized in Fig. 7.6. Only unstrained films grown on STO exhibit metallic-like dρ/dT>0 in the entire range of temperatures under study (from 5 K to 300 K) (see Fig. 7.6 d).

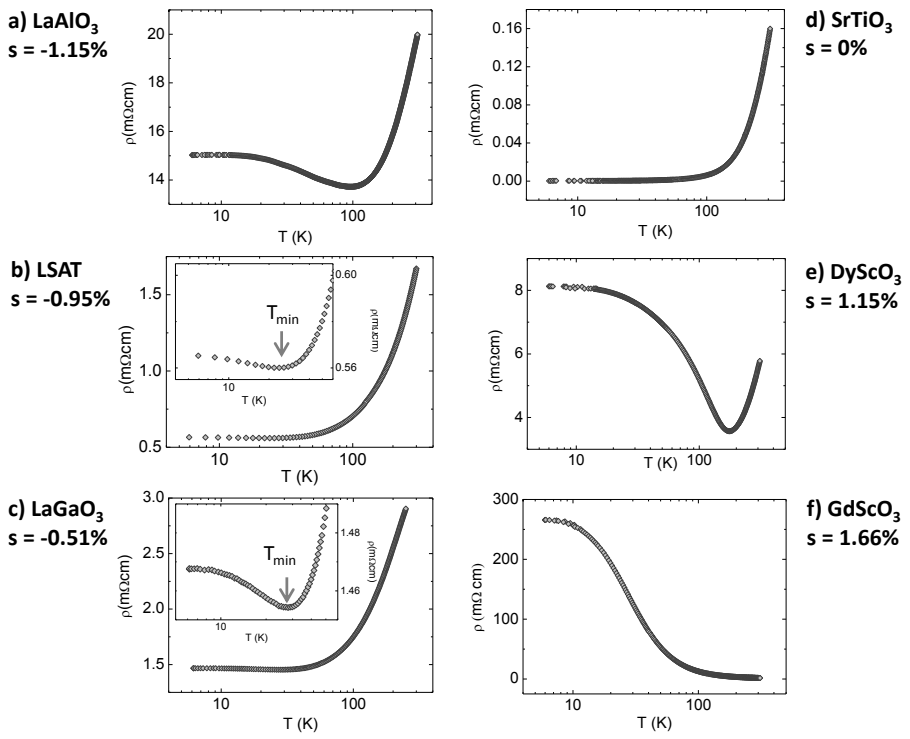

Figure 7.6: Temperature-dependent electrical resistivity of the Nb:STO films under different degrees of epitaxial strain. Films deposited on a) $LaAlO_3$, b) LSAT, c) $LaGaO_3$, d) $SrTiO_3$, e) $DyScO_3$ and f) $GdScO_3$. Not all the films are shown in this figure, for clarity.

All the other samples present an upturn with a logarithmic dependence of the ρ (T) below a certain temperature, T_{min}, which depends on strain (Fig. 7.7 a), similar to observations in LAO/STO interfaces [220, 248]. Also, the room temperature resistivity of the films increases with strain, but that can be accounted by the variation in the carrier density measured by Hall effect (see Fig. 7.7 b).

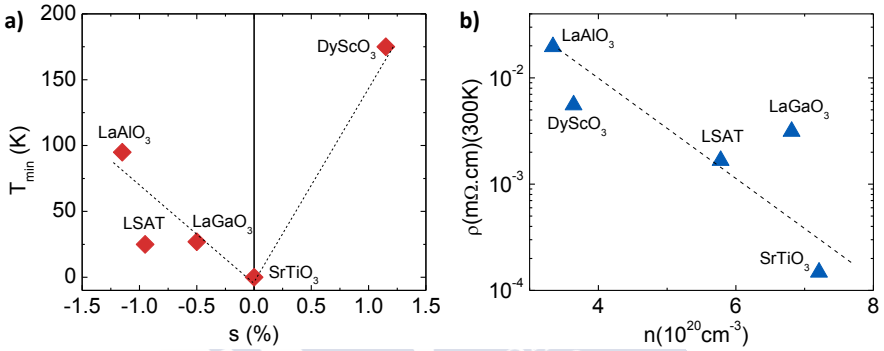

Figure 7.7: a) T_{min} versus experimental strain for the Nb:STO thin films considered in this Chapter. b) $\rho(300K)$ as a function of charge carrier density (n).

The metallic-like temperature dependence of the resistivity in n-doped $SrTiO_3$ has been treated in several papers, but there is a lack of consensus about the mechanism that governs the electronic transport in this dilute metal. Some authors reported a conventional Fermi-liquid behaviour below 100-150 K ($\rho(T) \propto AT^2$), with the pre-exponential factor A inversely proportional to the charge carrier concentration [249–251]. However, other groups reported a departure from this behaviour, with a temperature dependence of ρ closer to T^3, [252] as well as violations of the Kadowaki-Wood ratio [253].

The unstrained film shows a deviation from the AT^2 behaviour at low temperatures, as can be seen from the plot in Fig. 7.8 a). At low temperatures, the resistivity fits better to a cubic dependence, although what reveal these plots is a continuously varying exponent. With the

aim to extract the exponent that fits the resistivity in the whole range of temperatures, the $\rho(T)$ was plotted as a function of T^n using different values of n ranging approximately from 2 to 3 (see Fig. 7.8 c). From this analysis, we determined that the more appropriate scaling exponent is close to 2.78.

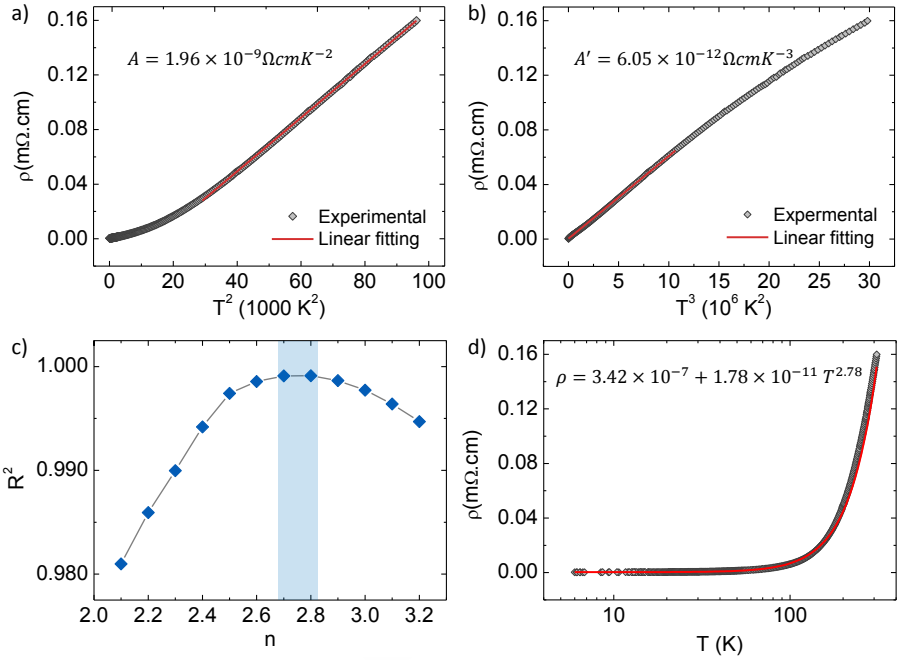

Figure 7.8: a) Resistivity of the unstrained thin film grown on an STO substrate against T^2 and b) T^3. In both representations the slope of the linear fitting is indicated. c) The coefficient R^2 as a function of different values of the n exponent. d) Fitting of the temperature dependence of the resistivity using the exponent obtained in c).

However, since the charge carrier concentration in the samples increases smoothly as the temperature increases (see Fig. 7.1), it is difficult to obtain definitive conclusions about the origin of the change in the exponent of $\rho(T)$.

Going back to the nature of the low temperature upturn of the resistivity, the logarithmic dependence below T_{min} and the saturation at very low temperatures is a characteristic signature of the presence of Kondo effect [222]. Several works pointed out this scattering process in heterostructures involving STO as a substrate, such as $PrAlO_3$/STO [254] or the LAO/STO interface [7, 223, 255].

The exchange interaction between conducting electrons and local magnetic moments introduces a scattering process in which the spin of the electrons is flipped (the Kondo effect). However, different from the case of non-magnetic impurities, a proper treatment of this effect shows the magnetic scattering cross-section diverges at low temperature, leading to an infinite resistivity [256, 257]. The thermal broadening of the electron wave vector distribution suppresses the divergence, resulting instead in an increase of $\rho(T)$ as temperature decreases. The competition between this effect and the conventional $e - ph$ scattering determines the existence of a minimum in $\rho(T)$ at a given temperature.

To fit the low temperature $\rho(T)$, we used the empirical formula proposed by Costi $et\ al.$ [258] and Lee $et\ al.$ [223] to describe the resistivity of gated-$SrTiO_3$. These authors observed a low-temperature upturn of the resistivity after application of a high electric field, and proposed a Kondo interaction between localized magnetic Ti^{3+} ions and delocalized electrons that partially filled the Ti 3-d conduction band:

$$\rho(T) = \rho_0 + AT^2 + BT^5 + \rho_k(0)\left(\frac{1}{1 + (2^{1/s} - 1)(T/T_k)^2}\right)^s \quad (7.7)$$

Here $\rho_k(0)$ is the Kondo resistance at zero temperature, s=0.225, accordingly to the theoretical result obtained by the numerical renormalization group [222, 223, 259] and T_K is the Kondo temperature. The latter is defined as the temperature below which the spins of the conduction electron screen out the spin of the localized magnetic moment.

To reduce the uncertainty of the parameters obtained from the fittings, we first fitted the ρ (T) curves above the T_{min} using Eq. 7.6 and extracted the values of A, B and ρ_0. Then, we fixed these values for the fitting at low temperatures according Eq. 7.7 in order to obtain T_K as

well as $\rho_k(0)$. As an example, in Fig. 7.9 we show the fittings for the samples grown on LSAT and LAO. The values of the different coefficients extracted from the fittings are summarized in Table 7.1.

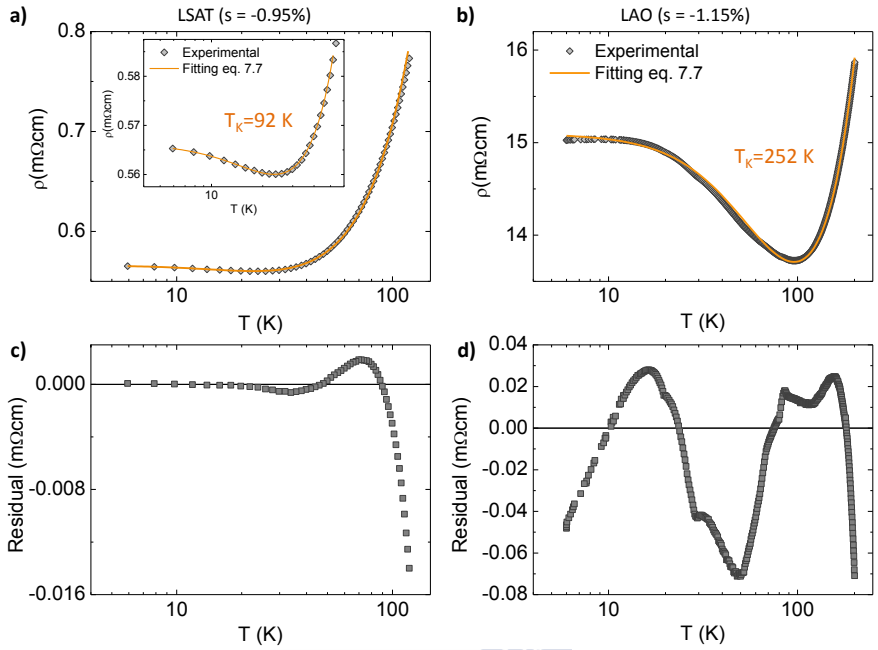

Figure 7.9: Fitting according to Eq. 7.7 of the resistivity dependence as a function of the temperature for the thin films grown on LSAT a) and LAO b). The inset in a) shows an enlargement of the data around T_{min}. Figs. c) and d) show the residual for the fittings presented on a) and b), respectively.

The values of the T^2 resistivity factor A (ranging from 10^{-7} to 10^{-9} Ωcm/K^2) are in agreement with previous reports in n-doped $SrTiO_3$ at similar carrier densities [249, 250, 260, 261]. On the other hand, from equation (7.5) and a dimensional analysis:

$$AT^2 = \frac{m^*}{ne^2}\frac{1}{\tau} = \frac{m^*}{ne^2}\Gamma(T^2) \propto \frac{m^*}{ne^2}\frac{(k_B T)^2}{\hbar E} \tag{7.8}$$

where Γ is the scattering rate function. In Fig. 7.10 we show the

Substrate	**s(%)**	**n (10^{20} cm^{-3})**	**T$_{min}$(K)**	**ρ_0 (Ωcm)**	**A (Ωcm/K^2)**	**B (Ωcm/K^5)**	**$\rho_K(0)$ (Ωcm)**	**T$_K$ (K)**
STO	0	7.21	–	0	1.96×10^{-9}	–	–	–
LGO	-0.51	6.81	27	1.32×10^{-3}	1.99×10^{-8}	4.08×10^{-17}	1.55×10^{-4}	81
LSAT	-0.95	5.78	25	4.72×10^{-4}	1.90×10^{-8}	1.03×10^{-17}	9.41×10^{-5}	92
LAO	-1.15	3.34	95	6.12×10^{-3}	1.21×10^{-7}	8.43×10^{-16}	8.94×10^{-3}	252

Table 7.1: Coefficients extracted from te fittings according to Eq. 7.7 for the films grown on $LaGaO_3$, LSAT and $LaAlO_3$ and $DyScO_3$. The value of the factor A for the film grown on a STO is the one obtained from the fitting in Fig. 7.8 a). Values of T$_{min}$ and charge carrier density (n) measured by Hall effect (at room temperature) are also shown.

dependence of A on the carrier density; in spite of the limited data, it seems that a quite accurate linear dependence can be established between A and $1/n$. According to equation 7.8, this means that Γ does not depend on the electron density which is counter intuitive with a conventional electron-electron scattering mechanism.

On the other hand, only electrons within an energy k_BT around the Fermi energy are important for electron-electron scattering, so that the relevant energy scale in this equation is $E = E_F$, and therefore $1/\tau = bk_BT^2/E_F$. A crude free electron calculation of the Fermi Energy for lightly doped STO (m*=0.7 m_e) [36] predicts a relaxation time $\approx 10^{-10}s$, similar to the values obtained from the fittings of the magnetoconductance in the preceding Section $\tau \approx 10^{-11}s$ (Fig. 7.4). Therefore, in spite of the high temperatures and the apparent independence of Γ on n, the temperature dependence of the resistivity in STO thin films above T_{min} is reasonably well described within an $e-e$ scattering mechanism, plus a phonon-T^5 contribution at higher temperatures.

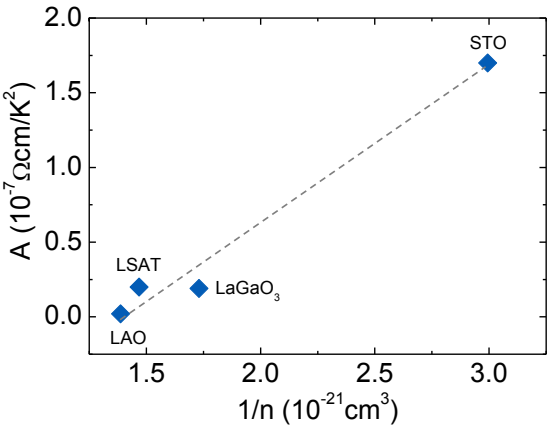

Figure 7.10: Variation of the factor A of T^2 term in the resistivity with the charge carrier concentration. The dashed line represents the linear fitting.

On the other hand, the values of $\rho(0)$ and particularly of T_K, obtained from the fitting show unrealistic/unphysical values $e.g.$ the very large $T_K \approx$200-500 K.

The Kondo resonance manifests as a narrow peak at the Fermi level with a width proportional to the Kondo temperature [262]. Since the Seebeck coefficient strongly depends on the energy dependence of the density of states at the Fermi energy, the Kondo resonance will cause a rapid increase of $S(T)$ [263–265]. Other important transport properties, such as specific heat coefficient and magnetic susceptibility, are also affected in the Kondo regime.

Furthermore, Kondo coupling is suppressed by an external magnetic field tending to promote ordering of impurity spins (suppressing spin flip), so that the anomaly of $S(T)$ at the Kondo temperature should decrease under the effect of the magnetic field.

The temperature dependent $S(T)$ for the thin film grown on LSAT is shown in Fig. 7.11 at B= 0 T and B=9 T. We have chosen this sample because according to the fittings of $\rho(T)$, T_K ≈92 K, which is well within the experimental range accessible in our setup. The details of the measurement are explained in Chapter 2 (Fig. 2.12).

The results are shown in Fig. 7.11. $S(T)$ is negative in all the range of temperatures studied, reaching its maximum absolute value at room temperature (≈-75 μV/K).

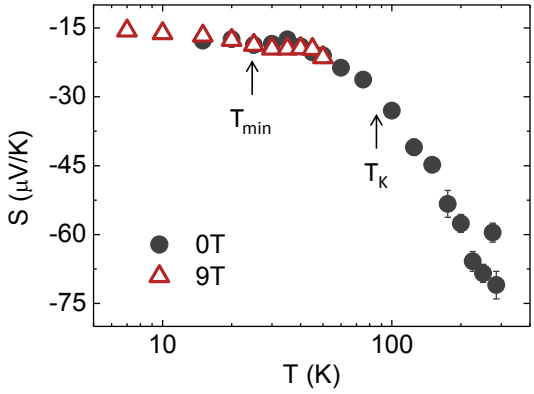

Figure 7.11: Temperature dependence of the Seebeck coefficient at 0 T and 9 T for the 19-nm thick Nb:STO thin film grown on LSAT. T_{min} and T_K are indicated in the representation.

No hints of Kondo scattering are observed on $S(T)$, which maintains a monotonic behaviour in all the range of temperatures without any observable change at T_K. Also, the negligible effect of B below T_{min} shows that the Fermi surface is not affected by the application of the magnetic field or low temperatures. Therefore, these results suggests that an alternative explanation to Kondo effect must be proposed to explain the low temperature upturn in n-doped STO (and probably in LAO/STO interfaces).

In this regard, Gor'kov [266] has already proposed the introduction of the notion of the mobility edge as a fundamental concept to understand the low temperature properties of n-doped $SrTiO_3$, particularly the superconductivity observed in this material. Likewise, other groups explained the metal-insulator transition observed in LAO/STO interfaces in terms of an Anderson localization induced by disorder [267, 268].

On the other hand, Ruderman-Kittel-Kasuya-Yosida (RKKY) interaction can also induce a resistivity minimum [269], as it happens in $RCuAs_2$ (R= Sm, Gd, Tb, and Dy) [270].

But before discussing the applicability of these scenarios to the transport properties of STO thin films, we will analyse the effect of an in-plane magnetic field on T_{min} as well as on the behaviour of the low temperature resistivity, as it will provide an important information for this discussion.

The resistance of STO thin films deposited on LSAT was measured for different magnetic fields (from 1 to 9 T) in the interval of temperatures around T_{min} (2-40K); the results are shown in Fig. 7.12 a).

As B increases, both the magnitude of the resistivity and the value of T_{min} decrease. Moreover, at the same time a change on the resistivity slope develops at low temperatures, and increases as B does. This change of slope, denoted by T_c (since it resembles the ordering of a magnetic phase, favoured by the application of B), can be observed more clearly in the representation of the resistance derivative as a function of temperature (Fig. 7.12 b). Furthermore, the evolution of T_{min} and T_c with B is shown in Fig. 7.12 c). Extrapolating them to high B, the crossing is produced at $\approx$ 15 K. This is approximately the temperature below which an optically-induced magnetic order was reported in

oxygen-deficient STO crystals [221], related to the optically polarized $V_{\ddot{O}}$ and their associated local moments. This suggests that ≈15-18 K could be a T_c for a long-range correlation between localized magnetic moments in lightly doped ($V_{\ddot{O}}$-induced) STO. Recent reports have also found direct evidence of in-plane ferromagnetism at the interface between LAO/STO [9, 26, 271].

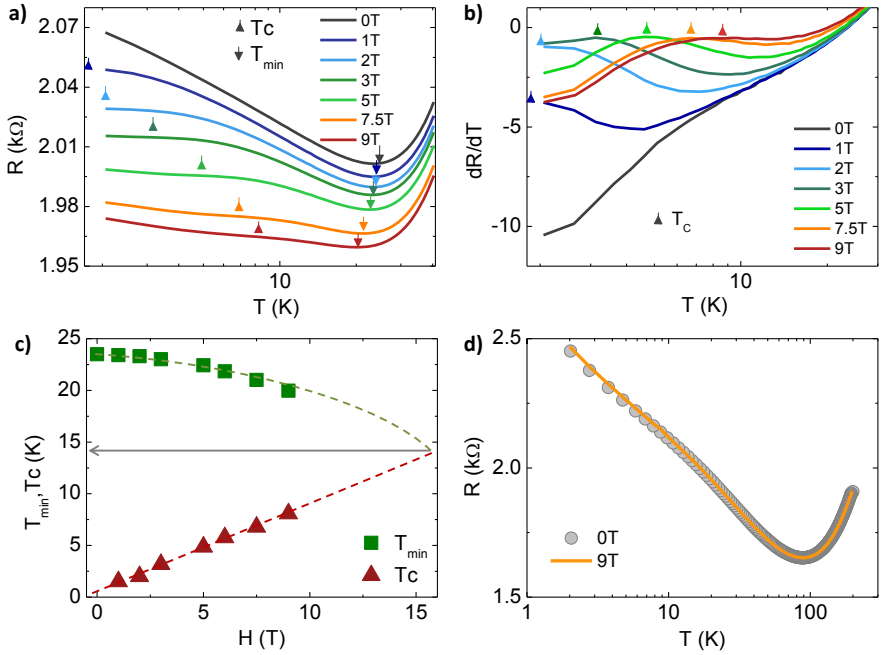

Figure 7.12: a) Temperature dependence of the resistance under different magnetic fields for a 19 nm thick film grown on LSAT. b) Derivative of the electrical resistivity corresponding to the data of figure a. The triangles mark the temperature T_c at which the change in the resistance slope occurs. c) Experimental evolution of T_{min} and T_c with the magnitude of magnetic field. Dashed lines indicate the extrapolation to high magnetic fields and the crossing at ≈15 K. d) Resistance measurement of the 35 nm thin film grown on LAO at 0 T and 9 T. The magnetic field is applied in-plane and perpendicular to the current in all the cases.

Importantly, similar measurements on thicker samples ($\approx$ 35 nm) deposited on LAO, do not show the MR effect, so that the local moments responsible for this effect seem to accumulate at the interface, and therefore its influence decreases as the thickness increases (Fig. 7.12 d).

Anisotropic magnetoresistance (AMR) can provide further information about the existence and nature of an ordered phase at low temperatures. In the ferromagnetic metals and alloys, spin-orbit coupling introduces an angular dependence of the electrical resistance on the relative orientation between the magnetization and the electric current [272, 273]. AMR can be defined as follows:

$$AMR(\%) = \frac{R(\theta) - R(0)}{R(0)} \times 100 \tag{7.9}$$

where θ represents the angle between the magnetic field and the injected current, so that R(θ) and R(0) represent the resistance at each θ and θ=0°, respectively. In the following analysis we discuss the results on 19 nm-thick films on LSAT and LAO, as well as on a 35 nm-thick sample grown on LAO. These are non-magnetic substrates that allow measurements applying high magnetic fields. Since STO substrate may present some conductivity due to the presence of oxygen vacancies, it was excluded from this analysis.

The results for the sample grown on LSAT are shown in Fig. 7.13. At the lower temperatures (2 K), AMR is positive with a maximum (minimum) value of 0.2% at π/2 (π), presenting a typical two-fold symmetry similar to LAO/STO interfaces [274–277].

The magnitude of the AMR decreases gradually as temperature increases, and changes its sign from positive to negative (maximum at π, minimum at π/2) at $\approx$15 K. This change of sign is preceded by a four-fold symmetric AMR between 15 - 18 K, with local maxima at π/2, 3π/2 and 2π (see Fig. 7.13 c and d). This is the temperature at which the crossing between T_{min} and T_c occurred when a high magnetic field was applied in the previous Section (see Fig. 7.12 c). Finally, AMR

disappears completely above ≈40 K, coincident with T_{min}.

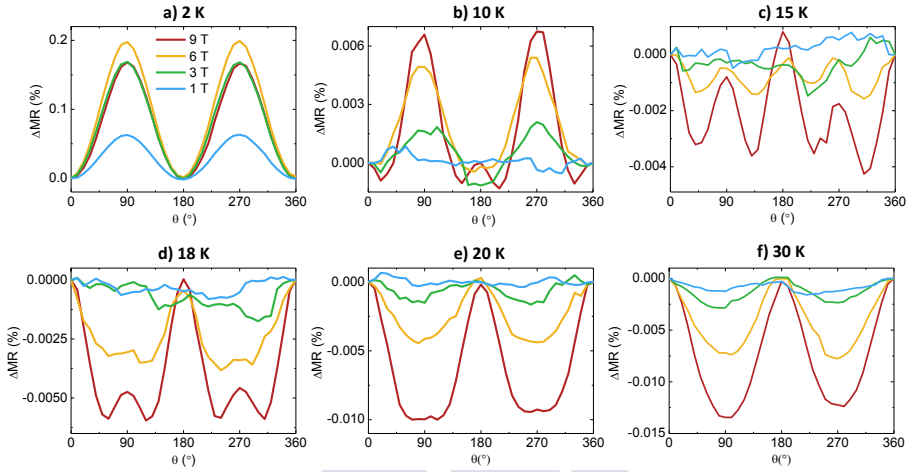

Figure 7.13: AMR for different magnetic fields (B=1, 3, 6, 9T) and temperatures, a) 2 K, b) 10 K, c) 15 K, d) 18 K, e) 20 K and f) 30 K. The legend is common to all panels.

The polar plots of the AMR at different temperatures (B= 9 T) are shown in Fig. 7.14 for the 19 nm thin films grown on LSAT (a-e) and LAO (f-j) substrates, as well as for the thicker sample (35 nm) deposited on LAO. The thinner samples exhibit similar behaviour, including the change in the AMR sign at temperatures close to 15-18 K, irrespective of the substrate. Nevertheless, AMR of the thicker sample does not show any change either in the sign or anisotropy axis as the temperature increases, remaining positive in the studied range of temperatures. This is a further indication that the possible magnetic order arises from the interface between the film and the substrate, so it disappears as the relative contribution of the interface decreases (i.e. as film thickness increases).

Flekser *et al*. [278] reported a large and positive four-fold AMR in conducting LAO/STO interfaces, while only a small and negative AMR was found in Nb:STO. From these results, they concluded that polarized magnetic scatterers and a Rashba-type spin-orbit interaction are

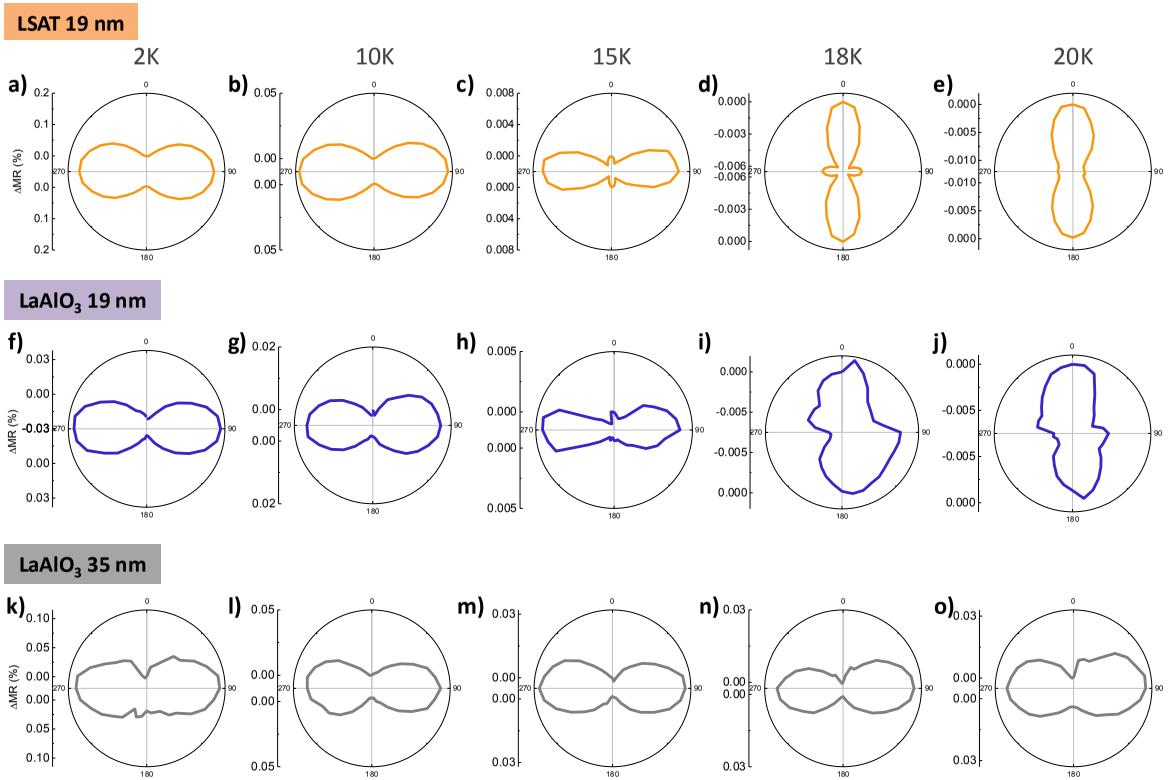

Figure 7.14: Polar plot of the AMR at 9 T for different temperatures from 2K to 20 K. a-e) Sample of 19 nm on LSAT and f-j) LAO. k-o) 35 nm thick film grown on LAO.

responsible for AMR in LAO/STO, while a conventional atomic spin-orbit interaction explains the effects observed in Nb:STO. However, we have shown that the sign and magnitude of the AMR may change considerably in thin films of n-doped STO as a function of temperature and thickness, challenging this interpretation.

As can be seen, the crossover from positive to negative AMR occurs gradually as temperature increases, suggesting the contribution of two phases that grow at the expense of each other. To understand this behaviour we propose the following empirical model:

$$\rho(\theta) = \rho_{iso} + \rho_{+} cos^2\theta - \rho_{-} sen^2 2\theta \tag{7.10}$$

where ρ_{iso} represents the isotropic contribution to the AMR, ρ_{+} and ρ_{-} are coefficients of the $\cos^2\theta$ and $\text{sen}^2 2\theta$ terms, respectively. The fitting to the experimental data shown in Fig. 7.15, exhibits a good agreement even at intermediate temperatures, at which the crossover from positive to negative AMR is produced.

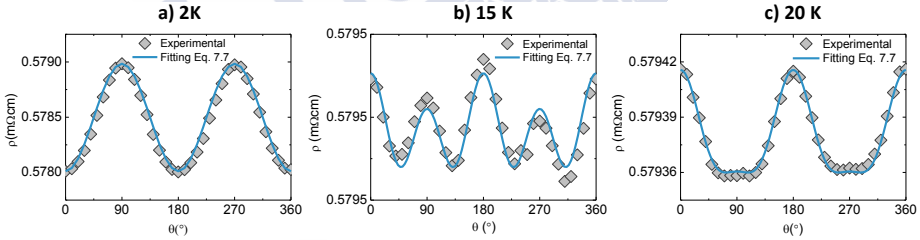

Figure 7.15: Experimental AMR for the 19 nm thick film grown on LSAT (symbols) and fittings to equation (7.10) (solid line), at different temperatures.

The values of ρ_{+} and ρ_{-} extracted from the fittings are shown in Fig. 7.16 a). The contribution of the phase responsible for ρ_{-} remains constant and small in the whole temperature range below ≈40 K. On the other hand, the ρ_{+} coefficient increases rapidly below ≈ 15 K, being two orders of magnitude higher that ρ_{-} at low temperatures.

The complete picture is presented in Fig. 7.16 b): at high temperatures (20-50 K), only a small and negative contribution to AMR exists,

but below T_{min}, the positive contribution increases rapidly and dominates completely below T_C.

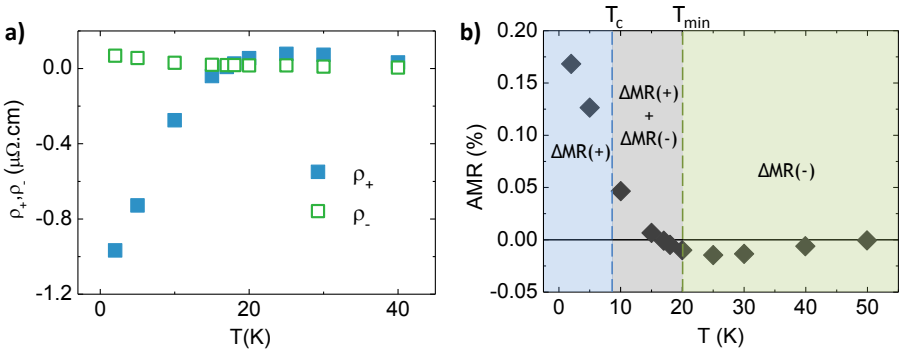

Figure 7.16: a) ρ_+ (solid blue squares) and ρ_- (open green squares) coefficients extracted from the fitting of the experimental AMR to Eq. 7.10. b) Experimental values of the AMR as a function of temperature. Vertical lines indicate the position of T_c and T_{min}.

In view of these results, the most probable picture is that local magnetic moments associated to Ti^{+3} linked to the presence of oxygen vacancies (and maybe to cationic defects also) interact strongly with the conduction electrons below T_{min}, and develop a magnetic order below T_C.

As we mentioned before, apart from the (in our opinion, less likely) Kondo effect, other mechanisms are compatible with the low temperature upturn in the resistivity, as well as with the sign and magnitude of the AMR. The firs one is the presence of a mobility edge separating localized from itinerant electron states.

In 1958, Anderson [234,279] proposed that a random potential may impede the electronic diffusion at zero temperature (*i.e.* introduce localization of the electronic wavefuntion) above a critical value of (V/W), where V is the random potential and W is the bandwidth. Atomic disorder in the form of cationic/anionic vacancies may be a source of such random potential over the crystalline ionic potential. Thus, if the system is close enough to the critical (V/W), but still in the itinerant side,

localized states appear at the tail of the bands below a critical energy, E_c, called the mobility edge [234]. In this case, conduction is by thermally activated for states below E_c, but diffusive after crossing the mobility edge. Moreover, the application of a magnetic field, strain, etc. may modify the relative position of E_c with respect to the Fermi energy (given the magnetic nature of the vacancies or their epitaxial strain-dependent distribution), therefore justifying the variations observed in different samples or under the influence of a magnetic field. However, the existence of a magnetically ordered state at low temperature is more difficult to justify. Also, a variable range hopping does not fit the temperature dependence of $\rho(T)$ in the thermally activated region, neither the low temperature saturation is predicted by this model [234].

A more appealing possibility is the existence of a ferromagnetic interaction of the RKKY type [280–282], between local moments and conduction electrons. Wang *et al.* [269] showed that some itinerant systems with large (classical) moments may develop a spin-liquid state with an enhanced resistivity at low temperatures due to RKKY interaction, under the conditions of having i) a small circular Fermi surface, and ii) magnetic frustration. Both conditions are satisfied in lightly n-doped STO [36]. In this particular case, liquid-like spin correlations produce incoherent elastic scattering, that contribute to the electrical resistivity [283].

The RKKY interaction enhances the structure factor (or the scattering cross section) for wave vectors connecting points of the Fermi surface, which for a circular surface translates into strong spin-spin correlations at $k \leq 2k_F$. This determines the temperature dependence of the resistivity, which increases below a given temperature following the temperature dependence of the scattering cross section at $k \leq 2k_F$. Note that RKKY considers a ferromagnetic interaction between the local spins and the itinerant electrons (different from the antiferromagnetic interaction characteristic of the Kondo effect). Therefore, if the system orders magnetically at low temperature, either spontaneously by the effect of exchange J or by application of a large magnetic field, the ordered spins only produce coherent electron scattering, which does not contribute to the resistivity (short-range spin fluctuations are the domi-

nant contribution to ρ) [284]. This picture is perfectly compatible with the monotonic evolution of $S(T)$ and also justifies the negative MR observed below ≈15 K at high magnetic fields.

As a complete picture, we propose that random local magnetic moments of Ti^{+3} associated to the presence of oxygen vacancies interact with the conduction electrons via RKKY coupling to develop a spin-liquid state below T_{min}. RKKY interaction enhances the elastic electron-spin scattering by increasing the magnetic structure factor, resulting in a net increase of the resistivity below that temperature. However, by further reducing the temperature or by applying a sufficiently large magnetic field, some long-range magnetic order can be emerged below Tc, which reduces its contribution to incoherent scattering and therefore, $\rho(T)$ tends to saturation, or eventually decreases ($d\rho/dT>0$ at $T<T_C$)

The effect of thickness suggests that a higher concentration of defects spontaneously accommodates at the interface with the substrate in order to relax epitaxial stress. Application of a strong electric field with the right geometry may accumulate highly mobile oxygen vacancies at/away from the interface, varying both the local density of charge carriers and localized moments associated to the presence of defects. This may be erroneously ascribed to an electric field-modulation of the Rashba spin-orbit interaction in this system. Consequently, the similarities with the phenomenology observed in the LAO/STO interfaces also suggests that the magnetotransport results on these polar interfaces should be probably revisited at the light of our results and conclusions.

7.3 Summary

In this Chapter, we have performed a careful study of the influence of strain and magnetic field on the electronic transport of n-doped STO thin films. The analysis of the out-of-plane magnetoconductance exhibits a crossover from WAL to WL at low temperatures (below T_{min}), depending on strain. The different scattering rates were determined from fittings of the experimental data to the HLN model. From these

results, we concluded that the spin-relaxation follows an Elliot-Yafet mechanism by interaction with local magnetic moments associated to vacancies, instead of a Rashba spin-orbit coupling.

At intermediate degrees of strain, the accumulation of defects close to the interface induces a minimum in the electrical resistivity, similar to that observed in LAO/STO interfaces. This effect is traditionally attributed to Kondo scattering by magnetic impurities. Nevertheless, Seebeck effect measurements do not show signatures of the existence of a Kondo resonance. Instead, we argue that a ferromagnetic interaction between random localized magnetic moments through conduction electrons (RKKY type) produces a spin-liquid state and an increase of the magnetic scattering cross-section, which in turn causes the increase of the resistivity at low temperatures. These results also suggest the existence of a weak magnetically ordered phase below 15-18 K, which could be a universal feature of n-doped STO over a wide range of doping.

It will be certainly interesting to repeat some these experiments under the influence of an static electric field, E. If, as previously hypothesized, magnetic moments (probably residing at Ti^{3+}) close to mobile $V_{\ddot{O}}$ are the cause of the spin-orbit coupling and many of the MR effects described in this Chapter, the application of E in the right geometry (field effect transistor) will modulate the concentration of these defects, creating accumulation/depletion regions of them. The removal of E would suppress such effects instantaneously if the Rashba effect were the source of the spin orbit coupling. But, if it is an effect related to the $[V_{\ddot{O}}]$, the suppression of E will not have any instantaneous effect. Instead, these processes will follow the slow relaxation of such defects at room temperature or below.

USC
UNIVERSIDADE
DE SANTIAGO
DE COMPOSTELA

Concluding remarks and outlook

The main motivation of this thesis was related to the necessity of understanding the effects of oxygen vacancies on the transport and magnetic properties of $SrTiO_3$ thin films and heterostructures based on STO, like the famous LAO/STO interfaces. Thus, among the most general contributions derived from this Thesis the following are highlighted:

- We have determined the enthalpy of formation of oxygen vacancies in STO under different degrees of epitaxial strain. Our results shows that ΔH decreases about 23% for an $\sim$1.2% of positive or negative strain. This offers a reliable information to understand the effect of vacancies on the stabilization of strain in STO thin films. In addition, we demonstrated that each $V_{\ddot{O}}$ releases two electrons to the conduction band of STO, independently of the degree or sign of strain.

- We established the conditions of pressure and temperature for the formation and annihilation of oxygen vacancies in STO films. We have concluded that the temperature is a key factor to achieve the correct stoichiometry of the samples in terms of oxygen content, which empathizes that extra care must be taken when selecting the conditions for the post-annealing protocols in general in STO-based heterostructures.

- We obtained the diffusion coefficient of oxygen vacancies at room temperature, resulting in $\sim 2\times10^{-17}$ cm^2/s for unstrained $SrTiO_3$

thin film. D is only significantly affected by tensile strain (showing an increase of 350% for 2% strain), whereas a moderate compressive strain does not show any appreciable effect on D value. The rapid increase showed by D on tensile stressed samples should be avoided for some applications such as resistive switching devices.

- Nb:STO thin films grown under different degrees of epitaxial strain exhibit distinct octahedral configuration, which is determined by a delicate coupling between strain, cationic vacancies and the octahedral rotations of the substrate underneath. In addition, we have determined through DFT calculations that samples under compressive strain can promote an out-of-plane spontaneous polarization when a particular octahedral configuration is presented. According to the simulations, the addition of oxygen vacancies promotes the stabilization of this polar distortion, which can result in a ferroelectric-like response of strained $SrTiO_3$ thin films.

- $SrTiO_3$ thin films can reproduced most of the phenomenology observed in LAO/STO interfaces, such as resistive switching effect, ferroelectricity, Kondo-like upturn in resistivity, anisotropic magnetoresistance or magnetic ordering. All this phenomenology in STO thin films comes from the creation of oxygen vacancies (and the associated Ti^3) to accommodate different degrees of epitaxial strain. In this regard, other oxygen conductors with Ti^{4+}/Ti^{3+} active redox pair (perovskites, spinels or browmillerites) could also be predisposed to show this rich phenomenology.

Probably more important than the particular results obtained in this PhD Thesis on STO thin films, the main interest of this work lies in the possibility of extending the results in a more general way to other transition metal oxides, including interfacial phenomena like those at (001) LAO/STO. This can lead to stablish general strategies to tailor certain properties of these technological interesting materials by controlling the anionic vacancies.

Considerable research efforts are still needed in both $SrTiO_3$ and other transition metal oxides, to understand in detail the mechanisms behind the effects produced by oxygen vacancies. But it is clear that ionic defects will play a crucial role in enhancing or enabling interesting technological applications in the future. For this objective, the development of growth and characterization techniques as well as first-principles calculations will be indispensable.

USC
UNIVERSIDADE
DE SANTIAGO
DE COMPOSTELA

Summary in Spanish/ Resumen en Castellano

Herbert Kroemer empezó su discurso al recibir el premio Nobel en el año 2000 afirmando que: ”Normalmente, se puede decir que la interfase es el dispositivo”. Con esta frase, se estaba refiriendo al sorprendente éxito de los dispositivos basados en películas delgadas de semiconductores para aplicaciones fotónicas y electrónicas, cuyo estudio había comenzado 40 años antes. Muchas de esas aplicaciones, tales como transistores, células solares o láseres, sacan partido actualmente de los fenómenos que ocurren en la interfase. Análogamente, la incorporación de interfases entre óxidos se espera que genere una nueva revolución tecnológica en los próximos años. De hecho, dichas interfases están actualmente en el punto de mira de una investigación intensa en el campo de la Física de la Materia Condensada. Estas interfases presentan un amplio rango de fenómenos interesantes, tales como magnetismo, superconductividad, conducción iónica o ferroelectricidad, que pueden encontrar aplicación directa en baterías, celdas de combustible, almacenamiento de información, entre otros.

Además, durante décadas anteriores se han ido desarrollado potentes técnicas de deposición como la deposición por láser pulsado o el crecimiento epitaxial por haces moleculares (PLD y MBE por sus siglas en inglés, respectivamente) que han permitido la deposición de interfases bien definidas entre óxidos complejos. Esta ingeniería a escala atómica se usa actualmente para crear interfases abruptas, lo que abre un mundo de posibilidades a la hora de explorar y hacer uso de propiedades fun-

damentales de esas interfaces, ofreciendo también el potencial para su uso futuros dispositivos.

Un buen ejemplo de esto último es la conductividad encontrada en la interfase entre el $LaAlO_3$ (LAO) y el $SrTiO_3$ (STO) por Ohtomo y Hwang en 2004. A pesar de que se trata de dos materiales fuertemente aislantes, en su interfase se forma un gas bidimensional de electrones (2DEG, por sus siglas en inglés) de unas pocas celdas unidad. Este nuevo fenómeno estimuló una intensa investigación para entender el mecanismo que lo provocaba. Al mismo tiempo, la expectación creada condujo al resurgimiento del campo de las interfases entre óxidos.

Además de la conductividad, la interfase LAO/STO presenta otras propiedades interesantes, como magnetoresistencia, superconductividad y ferromagnetismo, muchas de las cuales están presentes en los materiales que la constituyen. Para explicar la fenomenología observada en esta interfase, se han propuesto tres escenarios posibles: la catástrofe polar, vacantes de oxígeno o mezcla de cationes. Aún a día de hoy no hay un consenso claro sobre cuál de los tres mecanismos describe mejor la fenomenología vista en dicha interfase, o de si en realidad se trata de una combinación de varios de ellos. Pero un aspecto sobre el que sí que existe bastante consenso es que las vacantes de oxígeno podrían jugar un papel muy importante en sus propiedades. A esta conclusión se llega por varios motivos: la observación del 2DEG sólo es posible si la capa de $LaAlO_3$ se deposita a una baja presión de oxígeno, lo que favorece la inevitable creación de vacantes de oxígeno en el sustrato de STO; además, el 2DEG ha sido observado también en otras interfaces en las que el STO está presente. Esto lleva a pensar que las vacantes pueden inducir muchas de las propiedades funcionales reportadas tanto en la interfase de LAO/STO como en los óxidos en general.

Además de en esta famosa interfase, las vacantes de oxígeno podrían ser la clave para la ingeniería de las perovskitas basadas en óxidos. Estos materiales tienen una excelente flexibilidad para aceptar cambios en su composición, mediante la sustitución de ciertos cationes. Además, su fuerte carácter polar hace que los electrones estén fuertemente correlacionados y, por lo tanto, haya un acoplamiento entre carga, espín y grados de libertad de sus orbitales. Sin embargo, la posibilidad de mani-

pular el anión (es decir, el contenido en oxígeno) es igualmente interesante, pero mucho menos explorada. Es bien conocido que la creación de vacantes de oxígeno es una forma de relajar la tensión en las láminas delgadas, y que estas vacantes tienen efectos tanto en la estructura como en las propiedades de transporte de dichos materiales. Además, dado que las vacantes pueden llegar a ser móviles a temperatura ambiente y está positivamente cargadas, podrían ser susceptibles de ser manipuladas mediante estímulos externos (como un campo eléctrico). Está reportado también que pueden tener influencia tanto en las propiedades eléctricas como magnéticas de ciertos materiales.

Por otra parte, los defectos tanto extrínsecos como intrínsecos están siempre presentes, siendo en algunos casos deseables e incluso cruciales para inducir algunas propiedades. Muchas veces este tipo de defectos también aparecen debido al estrés aplicado a las películas delgadas.

Entre la familia de las oxoperovskitas, el STO es un ejemplo paradigmático. Se trata de un aislante paraeléctrico, cuya estabilidad química, diamagnetismo y alta constante dieléctrica le convierten en uno de los sustratos preferidos para el crecimiento de películas delgadas de otras perovskitas basadas en óxidos, tal como la ya mencionada interfase LAO/STO. Mediante dopaje, estrés o presencia de defectos se le pueden inducir multitud de propiedades funcionales con aplicaciones por ejemplo en sensores de gas o células solares. Pero quizá las vacantes de oxígeno son las más propensas a inducir nuevas propiedades en el STO. Por ejemplo, el STO con deficiencia en oxígeno es el primer óxido en el que se ha reportado superconductividad. Entre las propiedades inducidas en el STO por las vacantes de oxígeno, quizá la conmutación resistiva y la ferroelectricidad sean las más importantes, y son precisamente las que se abordarán en esta tesis.

De este modo, la **motivación general** de esta tesis es estudiar el efecto de las vacantes de oxígeno y el estrés epitaxial en las propiedades tanto estructurales como de transporte del STO en forma de películas delgadas. Las conclusiones servirán además para contribuir a la discusión sobre el papel que juegan las vacantes de oxígeno en la interfase de

LAO/STO, así como en otras heteroestructuras que involucren al STO como sustrato. Un aspecto novedoso del enfoque de esta tesis es que aúna tanto experimentos como cálculos teóricos, lo que proporciona las mejores herramientas para llevar a cabo el estudio propuesto.

Técnicas experimentales y métodos computacionales

Todas las muestras estudiadas en esta tesis han sido fabricadas mediante la técnica de deposición por láser pulsado (PLD), que es una de las técnicas más empleadas para la fabricación de películas delgadas de espesor nanométrico. El equipo de PLD utilizado está equipado con un láser KrF Excimer (λ=248 nm, duración de pulso $\approx$ 20 ns). El haz del láser entra en una cámara de alto vacío, en la cual es posible mantener una atmósfera controlada de nitrógeno o oxígeno. Dentro de dicha cámara se encuentra un blanco del material que se desea depositar sobre el cual impacta el haz del láser. El impacto produce una pluma de ablación que transfiere las especies atómicas al sustrato, manteniendo la estequiometría del blanco. El sustrato está en contacto con un calentador lo mantiene a alta temperatura para facilitar la cristalización del material depositado. En este tesis, se utilizaron sustratos de diferente parámetro de red, con el fin de modificar el estrés aplicado a las películas delgadas, que van desde a= 3.79 Å(LAO) hasta 3.98 Å(KTO). Lo que varía el estrés epitaxial entre -2.91 % y +2.15 %. Todos los sustratos utilizados fueron previamente tratatos térmica y/o químicamente para obtener una terminación superficial más plana, este paso es crucial para obtener una buena interfase entre la película delgada y el sustrato. Tanto las condiciones de deposición de las películas delgadas de STO (PO_2= 100 mtorr, T=1100°C, f=5 Hz and E$\approx$0.9 J/cm^2) como el espesor ($\sim$19 nm) se mantuvieron constantes para todas las muestras utilizadas en este trabajo.

Una vez fabricadas las películas delgadas, el siguiente paso es su

caracterización estructural mediante rayos X. Así se evalúa tanto su espesor como su estructura cristalina mediante las técnicas de reflectividad (XRR) y difracción (XRD). Mediante estas medidas se demostró que todas las muestras mantenían el mismo espesor y que la calidad cristalina de las muestras era excepcional. Además, las información sobre los parámetros de red se extrajo usando la técnica de cartografía del espacio recíproco (RSM), la cual da información sobre si las muestras están bien tensionadas siguiendo el parámetro de red impuesto por el sustrato o bien se relajan debido a la elevada tensión aplicada.

Además, las rotaciones de los octaedros TiO_6 presentes en las películas delgadas se determinaron estudiando las reflexiones de Bragg semienteras. La determinación del patrón de rotación en las películas delgadas es una paso determinante para ver su influencia en las propiedades del STO. Otra de las técnicas que da información sobre la calidad cristalina de las muestras es la microscopía electrónica de transmisión y barrido (STEM), la cual permite una visualización directa de la estructura cristalina de las muestras, así como la determinación a nivel de la nanoscala de las tensiones presentes en las películas delgadas e información de los defectos presentes.

Otra técnica con un papel muy relevante en la parte experimental de esta tesis es la microscopía de fuerza atómica, que permite caracterizar la superficie de las películas delgadas a nivel atómico. Además, se han utilizado varias variantes de este instrumento como son la microscopía de fuerzas electrostáticas y la microscopía de fuerzas de Kelvin (EFM y el KPFM por sus siglas en inglés respectivamente), las cuales permiten aplicar un campo eléctrico utilizando la punta del AFM, así como la medida de la fuerza electrostática y la potencial de superficie de las películas delgadas, respectivamente. Por último, se han caracterizado las propiedades de transporte de las muestras utilizando en la mayor parte de los casos el método de van der Pauw y en otros una barra hall litografiada sobre la superficie de la muestra.

Respecto a los métodos computacionales usados para realizar las simulaciones de esta tesis, se han utilizado dos software distintos: Wien2k y VASP. Se usaron además como funcionales de correlación de intercambio la aproximación de gradiente generalizada (GGA, por sus siglas

en inglés) con las aproximaciones de Perdew-Burke-Ernzerhof (PBE) y PBE para sólidos (PBEsol). El cálculo de los valores de polarización se llevó a cabo usando tanto el método basado en las cargas efectivas de Born como el método de Fase de Berry.

Resultados y conclusiones

Termodinámica de la formación de vacantes de oxígeno

En esta parte del trabajo se estudiaron en detalle las propiedades estructurales de las muestras, determinando el correcto crecimiento de las mismas y el hecho de si están relajadas o no debido a la tensión aplicada por el respectivo sustrato. Una vez realizada la caracterización estructural de las muestras se estudió cuál era el número de electrones que cada vacante cedía a la banda de conducción del material así como la influencia de la temperatura en la creación de vacantes y su posterior aniquilación. Para ello se realizaron sucesivos procesos de post-recocido en las muestras a distintas presiones de oxígeno y temperaturas. Así, se comprobó experimentalmente que cada vacante dona dos electrones a la banda de conducción del STO independientemente de la tensión que se le aplica a la película delgada.

Otro resultado muy llamativo es que la creación de vacantes es independiente de la temperatura si el proceso de recocido se realiza por encima de 600 ^{o}C, mientras que la aniquilación de las vacantes sólo es completa a 800^{o}C. Por debajo de esa temperatura no se consigue aniquilar las vacantes previamente creadas en el proceso a baja presión de oxígeno. Este resultado es muy importante a la hora de diseñar los protocolos para conseguir muestras totalmente estequiométricas y sus implicaciones no sólo afectan al STO en forma de película delgada, sino que también se pueden extender al STO como sustrato.

Además, se estudió el coste energético de la creación de una vacante dependiendo de la tensión epitaxial aplicada a las películas delgadas, observando que depende fuertemente de dicho parámetro. Así, la

energía de formación de una vacante (ΔH) disminuye aproximadamente un 23 % tanto para estrés compresivo como tensivo, un resultado que coincide con anteriores resultados teóricos reportados por otros grupos. El valor de ΔH para la película de STO sin tensión epitaxial es de 0.51 eV.

Movimiento controlado de las vacantes de oxígeno

En este capítulo se estudió el movimiento controlado de las vacantes de oxígeno dentro de las películas delgadas, mediante la aplicación de un campo eléctrico externo creado por la punta del AFM. Así, la aplicación de un voltaje positivo repele las vacantes de oxígeno (que están cargadas positivamente), mientras que un voltaje negativo atrae dichas vacantes. Esto demuestra la posibilidad de manipular la concentración de vacantes a nivel local en las películas delgadas. Este resultado podría tener repercusiones en aplicaciones prácticas como las memorias de tipo commutación de resistencia, debido a que las vacantes cargadas pueden cambiar a nivel local la resistencia del material, produciendo diferentes estados. Además de esto, la conductividad térmica a nivel local puede verse afectada también por la diferente concentración de vacantes.

Se determinó el coeficiente de difusión de las vacantes de oxígeno dependiendo del estrés epitaxial, obteniendo un sorprendente aumento de la difusión de oxígeno para las muestras con estrés tensivo (aproximadamente un 350 % para el 2 % de estrés positivo) en comparación con la muestra crecida sin estrés. Todas las muestras presentan un valor del coeficiente de difusión del orden de 10^{-17}cm^2/s.

Además, con la finalidad de proponer el uso del STO en memorias de tipo conmutación de resistencia, se examinaron los principales parámetros de control en la producción y estabilización de estos dispositivos tales como tiempo de pulso, voltaje aplicado, temperatura y reversibilidad.

Rotaciones de los octaedros TiO_6 y respuesta ferroeléctrica en películas delgadas de STO en función del estrés epitaxial

Este capítulo combina resultados experimentales y teóricos. En él se estudia los patrones de rotación de los octaedros dependiendo del estrés aplicado a las películas delgadas. Se observó que dicho patrón de rotación depende mucho del estrés y los defectos presentes, pero también de las rotaciones que imponga el sustrato usado para el cremiento de las películas. Así, como regla general, las muestras crecidas con estrés compresivo o sin estrés presentan un patrón de rotación tipo $a^+b^+c^0$ compatible con el grupo espacial $I4/mmm$, mientras que las muestras crecidas con estrés positivo adoptan el patrón de rotación presente en el sustrato usado en cada caso.

El mecanismo que da lugar a este curioso comportamiento del patrón de rotación se comprobó mediante simulaciones ab-initio. Los parámetros estudiados como posible origen de las distintas configuraciones octahédricas fueron: el estrés, las vacantes de oxígeno y las vacantes de estroncio. De los resultados se concluyó que el factor más determinante es el estrés epitaxial. Este resultado abre la puerta a un posible control $ad\ hoc$ del patrón de rotación de las películas delgadas mediante la aplicación de estrés.

Además, experimentalmente se observó una respuesta ferroeléctrica en las películas delgadas crecidas con estrés negativo cuando se modificaba localmente la concentración de vacantes de oxígeno. El efecto es breve (unos 20 minutos) pero sugiere que cierto patrón de rotación y concentración de vacantes puede inducir ferroelectricidad en el STO, tal que lo convierta en un "relaxor ferroelectric". Para confirmarlo se realizaron cálculos ab-initio con diferentes patrones de rotación y grados de estrés. Se determinó que el patrón de rotación observado experimentalmente para las muestras con estrés negativo podía estabilizar una polarización fuera del plano en las películas de STO. Sin embargo, otros grupos espaciales estudiados nunca llegaban a estabilizar dicha polarización para estrés negativo. El estrés positivo sin embargo, conserva la polarización para numerosos grupos espaciales con distintos patrones

de rotación y normalmente presenta polarización en el plano.

Una vez determinado esto, se introdujo adicionalmente el efecto de las vacantes de oxígeno. Se estudió tanto el efecto de una vacante ecuatorial como de una apical. La conclusión principal fue que la presencia de vacantes de oxígeno (tanto ecuatoriales como apicales) produce una distorsión polar para las rotaciones observadas en las muestras con estrés negativo, confirmando los resultados experimentales. Para este caso, se estimó mediante el método de Fase Berry que la polarización espontánea puede llegar a un valor máximo de $\sim 20 \mu C/cm^2$.

Los resultados de este capítulo abren el camino para controlar propiedades muy importantes a nivel práctico, como la ferroelectricidad, mediante la manipulación del patrón de rotación de los octaedros junto con la influencia de las vacantes de oxígeno en las películas delgadas de STO.

Propiedades de transporte en las películas delgadas de STO en función del estrés epitaxial

En este último capítulo, se estudiaron las propiedades de transporte de las películas delgadas de STO en función del estrés epitaxial. Para ello, se midió la resistividad en función de la temperatura y se determinó, mediante ajustes, los diferentes procesos de scattering que podrían explicar el comportamiento de dichas curvas de resisividad. De estos resultados está claro que el estrés epitaxial controla la temperatura a la que se produce la transición metal-aislante en las películas delgadas (T_{min}), aquellas con menos estrés presentan comportamiento metálico mientras que a medida que el estrés aumenta (tanto positivo como negativo) van adoptando un comportamiento semiconductor o incluso aislante.

Además, en algunas muestras se observa un mínimo característico en la resistividad seguido de un repunte con dependencia logarítmica. Este comportamiento es comúnmente asociado a la presencia del efecto Kondo, mecanismo que está relacionado con la existencia de momentos magnéticos localizados en la película, los cuales interaccionan de forma anti-ferromagnética con los electrones de conducción. En nuestro caso, los Ti^{3+}, que se forman cuando se crea un vacante de oxígeno, jugarían

el papel de momento magnético localizado. Sin embargo, las temperaturas de Kondo anormalmente altas obtenidas de algunos ajustes hacen pensar que esta no sea la explicación correcta del comportamiento de la resistividad. Para comprobarlo, se midió el coeficiente Seebeck en alguna de las muestras, este coeficiente se ve enormemente afectado si efectivamente estamos ante un escenario de Kondo. Sin embargo, en las medidas tanto aplicando campo magnético como sin él, no se observa ninguna pista que sugiera que nuestras muestras presenten efecto Kondo.

Adicionalmente, la resistividad puede ser modificada mediante la aplicación de un campo magnético externo. Conforme la magnitud de éste aumenta, tanto la magnitud de la resistividad como la temperatura a la que se produce el mínimo disminuyen. Además, un efecto inesperado aparece a muy bajas temperaturas, produciendo un cambio en la pendiente de la resistividad a temperaturas cada vez mayores (T^*) conforme aumente el campo magnético. Representando T_{min} y T^* frente al campo magnético se prevé que las dos temperaturas se crucen a más o menos 15 K, justo la temperatura a la que está reportada la aparición de un orden magnético en cristales de STO reducidos. Esto nos hace pensar que el campo magnético induce algún tipo de orden magnético en los Ti^{3+} presentes en la muestra, tal como la interacción Ruderman-Kittel-Kasuya-Yosida (RKKY). Esta suposición es apoyada también por el hecho que dichos efectos en la resistividad con el campo magnético no se producen en muestras con más grosor. Esto apunta además a que los Ti^{3+} están principalmente concentrados en la interfase entre la película y el sustrato, y que al aumentar la contribución relativa de la interfase el efecto no se aprecia. La competición entre estos dos efectos se puede apreciar también en la magnetoresistencia anisotrópica, la cual cambia de signo a campos magnético altos cerca de 15 K sólo en las muestras con espesores más bajos. Para explicar todos resultados se propone el modelo basado en una transición de Anderson en lugar del modelo de Kondo.

Por último, se estudió también la magnetoresistencia con el campo magnético fuera del plano, determinando mediante ajustes con el modelo de Hakami-Larkin-Nagaoka (HLN) el valor de los diferentes tiem-

pos de scattering (inelástico, elástico y espín-órbita). La presencia del acoplamiento espín-órbita es remarcable sobre todo en las muestras con mayor estrés negativo (i.e. con mayor número de defectos). De los valores se determinó que el mecanismo de Elliot-Yafet para la relajación del espín es el que tiene lugar en nuestro sistema, apuntando directamente a los defectos como origen del acoplamiento espín-orbita.

Conclusiones generales

Aparte de la importancia de los resultados particulares de esta tesis, se pueden extraer conclusiones generales con repercusiones importantes.

- El entendimiento de los mecanismos para la formación de una vacante de oxígeno así como su difusión pueden tener profundas implicaciones en aplicaciones como sensores, membranas, catálisis o celdas de combustible sólido.

- Las condiciones usadas en los procesos de recocido han demostrado ser vitales para conseguir muestras totalmente estequiométricas. Esto debe tenerse muy en cuenta para las heteroestructuras que involucren al $SrTiO_3$ como sustrato pero también para otros óxidos en general.

- El control del patrón de rotación de los octahedros en películas delgadas de STO mediante el estrés epitaxial puede habilitar propiedades funcionales como la ferroelectricidad. Así, la manipulación de estas configuraciones octahédricas junto con la presencia de vacantes de oxígeno puede representar una forma de controlar estas interesantes propiedades no sólo en el STO, sino más generalmente en otras oxoperovskitas.

- El STO puede reproducir la mayoría de los fenómenos observados en la interfase de LAO/STO, como el efecto de conmutación resistiva, ferroelectricidad, efecto Kondo, magnetoresistencia anisotrópica o orden magnético. Toda esta fenomenología en las películas de STO tiene como origen de la creación de vacantes de

oxígeno (y de los Ti^{3+} asociados) para acomodar los diferentes grados de estrés epitaxial. Así, otros conductores de oxígeno con el par redox Ti^{4+}/Ti^{3+} activado (perovskitas, espinelas o browmileritas) podrían presentar también este tipo de fenomenología.

List of publications

- L. Iglesias, Alexandros Sarantopoulos, C. Magén, F. Rivadulla, "Oxygen vacancies in strained $SrTiO_3$ thin films: formation enthalpy and manipulation", Physical Review B, vol. 95, 165138, 2017.

- Araceli Gutiérrez-Llorente, Lucía Iglesias, Benito Rodríguez-González, Francisco Rivadulla, "Epitaxial stabilization of pulsed laser deposited $Sr_{n+1}Ir_nO_{3n+1}$ thin films: Entangled effect of growth dynamics and strain", APL Materials, vol. 6, 091101, 2018.

- Lucia Iglesias, Andrés Gómez, Martí Gigh, Francisco Rivadulla, "Tuning oxygen vacancy diffusion through strain in $SrTiO_3$", ACS Applied Materials & Interfaces, vol. 10 (41), 35367, 2018.

- Elias Ferreiro-Vila, Lucia Iglesias, Irene Lucas del Pozo, Noa Varela-Dominguez, Cong Tinh Bui, Beatriz Rivas-Murias, J. M. Vila-Fungueiriño, Pilar Jimenez-Cavero, Cesar Magen, Luis Morellon, Victor Pardo, Francisco Rivadulla, "Apparent auxetic to non-auxetic crossover dri-/ven by Co^{+2} redistribution in $CoFe_2O_4$ thin films", APL Materials, vol. 7,031109, 2019.

USC
UNIVERSIDADE
DE SANTIAGO
DE COMPOSTELA

List of oral presentations

- Iglesias, A. Sarantopoulos, F. Rivadulla, "Thermodynamics of formation of oxygen vacancies in Nb:$SrTiO_3$ thin films", IX Meeting GEFES, Cuenca (Spain), 2016. Poster.

- L. Iglesias, A. Sarantopoulos, F. Rivadulla, "Thermodynamics of formation of oxygen vacancies in Nb:$SrTiO_3$ thin films", MRS Fall Meeting, Boston (EEUU), 2016. Poster.

- Iglesias, A. Sarantopoulos, F. Rivadulla, "Oxygen vacancies in strained $SrTiO_3$ thin films: formation enthalpy and manipulation", XXXVI Biennial Meeting of the Spanish Royal Physics Society (RSEF), Santiago de Compostela (Spain), 2017. Oral presentation.

- L. Iglesias, A. Sarantopoulos, F. Rivadulla, "Oxygen vacancies in strained $SrTiO_3$ thin films: formation enthalpy and manipulation", E-MRS Fall Meeting, Warsaw (Poland), 2017. Oral presentation.

- L. Iglesias, A. Gómez, M. Gigh, F. Rivadulla, "Mechanical and electrical control of oxygen vacancies in strained $SrTiO_3$ thin films", X GEFES, Valencia (Spain), 2018. Poster.

- L. Iglesias, A. Gómez, M. Gigh, F. Rivadulla, "Mechanical and electrical control of oxygen vacancies in strained $SrTiO_3$ thin films", March Meeting, Los Angeles (EE.UU), 2018. Oral presentation.

- L. Iglesias, F. Rivadulla, "Anisotropic magnetoresistance in Nb:$SrTiO_3$ thin films under epitaxial strain", March Meeting, Boston (EEUU), 2019. Oral presentation.

Bibliography

[1] C. K. Maiti. *Selected Works of Professor Herbert Kroemer*. WORLD SCIENTIFIC, 2008.

[2] J. Mannhar and A. Herrnberger. The interface is still the device. *Nature Materials*, 11:91, 2012.

[3] A. Ohtomo and H. Y. Hwang. A high-mobility electron gas at the $LaAlO_3/SrTiO_3$ heterointerface. *Nature*, 427(6973):423–426, 2004.

[4] E. Dagotto. When oxides meet face to face. *Science*, 318(5853):1076–1077, 2007.

[5] H. Y. Hwang, Y. Iwasa, M. Kawasaki, B. Keimer, N. Nagaosa, and Y. Tokura. Emergent phenomena at oxide interfaces. *Nature Materials*, 11(2):103–113, 2012.

[6] J. Mannhart and D. G. Schlom. Oxide interfaces—an opportunity for electronics. *Science*, 327(5973):1607–1611, 2010.

[7] A. Brinkman, M. Huijben, M. Van Zalk, J. Huijben, U. Zeitler, J.C. Maan, W. G. van der Wiel, G. Rijnders, D. H. A. Blank, and H. Hilgenkamp. Magnetic effects at the interface between non-magnetic oxides. *Nature Materials*, 6(7):493, 2007.

[8] N. Reyren, S. Thiel, A. D. Caviglia, L. Fitting Kourkoutis, G. Hammerl, C. Richter, C. W. Schneider, T. Kopp, A. S. Rüetschi, D. Jaccard, M. Gabay, D. A. Muller, J. M. Triscone,

and J. Mannhart. Superconducting interfaces between insulating oxides. *Science*, 317(5842):1196–1199, 2007.

[9] J. S. Lee, Y. W. Xie, H. K. Sato, C. Bell, Y. Hikita, H. Y. Hwang, and C. C. Kao. Titanium d_{xy} ferromagnetism at the $LaAlO_3/SrTiO_3$ interface. *Nature Materials*, 12(8):703–706, 2013.

[10] Z. Q. Liu, C. J. Li, W. M. Lü, X. H. Huang, Z. Huang, S. W. Zeng, X. P. Qiu, L. S. Huang, A. Annadi, J. S. Chen, et al. Origin of the two-dimensional electron gas at $LaAlO_3/SrTiO_3$ interfaces: the role of oxygen vacancies and electronic reconstruction. *Physical Review X*, 3(2):021010, 2013.

[11] A. Kalabukhov, R. Gunnarsson, J. Börjesson, E. Olsson, T. Claeson, and D. Winkler. Effect of oxygen vacancies in the $SrTiO_3$ substrate on the electrical properties of the $LaAlO_3$/ $SrTiO_3$ interface. *Physical Review B*, 75(12):121404, 2007.

[12] Z. Q. Liu, L. Sun, Z. Huang, C. J. Li, S. W. Zeng, K. Han, W. M. Lü, T. Venkatesan, and Ariando. Dominant role of oxygen vacancies in electrical properties of unannealed $LaAlO_3/SrTiO_3$ interfaces. *Journal of Applied Physics*, 115(5):054303, 2014.

[13] C. Xu, C. Bäumer, R. A. Heinen, S. Hoffmann-Eifert, F. Gunkel, and R. Dittmann. Disentanglement of growth dynamic and thermodynamic effects in $LaAlO_3/SrTiO_3$ heterostructures. *Scientific Reports*, 6:22410, 2016.

[14] N. Nakagawa, H. Y Hwang, and D. A. Muller. Why some interfaces cannot be sharp. *Nature Materials*, 5(3):204, 2006.

[15] J. Yi and S. Li. *Functional Materials and Electronics*. Apple Academic Press, 2017.

[16] Z. S. Popović, S. Satpathy, and R. M. Martin. Origin of the two-dimensional electron gas carrier density at the $LaAlO_3$ on $SrTiO_3$ interface. *Physical Review Letters*, 101(25):256801, 2008.

[17] S. Thiel, G. Hammerl, A Schmehl, C. W. Schneider, and J. Mannhart. Tunable quasi-two-dimensional electron gases in oxide heterostructures. *Science*, 313(5795):1942–1945, 2006.

[18] C. L. Jia, S. B. Mi, M. Faley, U. Poppe, J. Schubert, and K. Urban. Oxygen octahedron reconstruction in the $LaAlO_3/SrTiO_3$ heterointerfaces investigated using aberration-corrected ultrahigh-resolution transmission electron microscopy. *Physical Review B*, 79(8):081405, 2009.

[19] R. Pentcheva and W. E. Pickett. Avoiding the polarization catastrophe in $LaAlO_3$ overlayers on $SrTiO_3$ (001) through polar distortion. *Physical Review Letters*, 102(10):107602, 2009.

[20] Y. Chen, N. Pryds, J. E. Kleibeuker, G.n Koster, J. Sun, E. Stamate, B. Shen, G. Rijnders, and S. Linderoth. Metallic and insulating interfaces of amorphous $SrTiO_3$-based oxide heterostructures. *Nano Letters*, 11(9):3774–3778, 2011.

[21] C. Li, Z. Liu, W. Lü, X. R. Wang, A. Annadi, Z. Huang, S. Zeng, T. Venkatesan, et al. Tailoring the two dimensional electron gas at polar $ABO_3/SrTiO_3$ interfaces for oxide electronics. *Scientific Reports*, 5:13314, 2015.

[22] K. Janicka, J. P. Velev, and E. Y. Tsymbal. Quantum nature of two-dimensional electron gas confinement at $LaAlO_3/SrTiO_3$ interfaces. *Physical Review Letters*, 102(10):106803, 2009.

[23] M. Basletic, J. L. Maurice, C. Carrétéro, G. Herranz, O. Copie, M. Bibes, E. Jacquet, K. Bouzehouane, S. Fusil, and A. Barthélémy. Mapping the spatial distribution of charge carriers in $LaAlO_3/SrTiO_3$ heterostructures. *Nature Materials*, 7(8):621, 2008.

[24] G. Herranz, M. Basletić, M. Bibes, C. Carrétéro, E. Tafra, E. Jacquet, K. Bouzehouane, C. Deranlot, A. Hamzić, J. M. Broto, et al. High mobility in $LaAlO_3/SrTiO_3$ heterostructures:

Origin, dimensionality, and perspectives. *Physical Review Letters*, 98(21):216803, 2007.

[25] L. Li, C. Richter, J. Mannhart, and R. C. Ashoori. Coexistence of magnetic order and two-dimensional superconductivity at $LaAlO_3/SrTiO_3$ interfaces. *Nature Physics*, 7(10):762, 2011.

[26] J. A. Bert, B. Kalisky, C. Bell, M. Kim, Y. Hikita, H. Y. Hwang, and K. A. Moler. Direct imaging of the coexistence of ferromagnetism and superconductivity at the $LaAlO_3/SrTiO_3$ interface. *Nature Physics*, 7(10):767, 2011.

[27] G. Herranz, F. Sánchez, N. Dix, M. Scigaj, and J. Fontcuberta. High mobility conduction at (110) and (111) $LaAlO_3/SrTiO_3$ interfaces. *Scientific Reports*, 2:758, 2012.

[28] C. Cancellieri, N. Reyren, S. Gariglio, A. D. Caviglia, A. Fête, and J.-M. Triscone. Influence of the growth conditions on the $LaAlO_3/SrTiO_3$ interface electronic properties. *EPL (Europhysics Letters)*, 91(1):17004, 2010.

[29] Y. Li, S. Na Phattalung, S. Limpijumnong, J. Kim, and J. Yu. Formation of oxygen vacancies and charge carriers induced in the n-type interface of a $LaAlO_3$ overlayer on $SrTiO_3$ (001). *Physical Review B*, 84(24):245307, 2011.

[30] J. Shen, H. Lee, R. Valentí, and H. O. Jeschke. Ab initio study of the two-dimensional metallic state at the surface of $SrTiO_3$: importance of oxygen vacancies. *Physical Review B*, 86(19):195119, 2012.

[31] J. Biscaras, N. Bergeal, S. Hurand, C. Grossetête, A. Rastogi, R.C. Budhani, D. LeBoeuf, C. Proust, and J. Lesueur. Two-dimensional superconducting phase in $LaTiO_3/SrTiO_3$ heterostructures induced by high-mobility carrier doping. *Physical Review Letters*, 108(24):247004, 2012.

[32] P. Moetakef, T. A. Cain, D. G. Ouellette, J. Y. Zhang, D. O. Klenov, A. Janotti, C. G. Van de Walle, S. Rajan, S. J. Allen, and S. Stemmer. Electrostatic carrier doping of $GdTiO_3/SrTiO_3$ interfaces. *Applied Physics Letters*, 99(23):232116, 2011.

[33] P. Perna, D. Maccariello, M. Radovic, U. Scotti di Uccio, I. Pallecchi, M. Codda, D. Marré, C. Cantoni, J. Gazquez, M. Varela, et al. Conducting interfaces between band insulating oxides: The $LaGaO_3/SrTiO_3$ heterostructure. *Applied Physics Letters*, 97(15):152111, 2010.

[34] K. Ueno, S. Nakamura, H. Shimotani, A. Ohtomo, N. Kimura, T. Nojima, H. Aoki, Y. Iwasa, and M. Kawasaki. Electric-field-induced superconductivity in an insulator. *Nature Materials*, 7(11):855, 2008.

[35] H. Nakamura, H. Tomita, H. Akimoto, R. Matsumura, I. H. Inoue, T. Hasegawa, K. Kono, Y. Tokura, and H. Takagi. Tuning of metal–insulator transition of quasi-two-dimensional electrons at Parylene/$SrTiO_3$ interface by electric field. *Journal of the Physical Society of Japan*, 78(8):083713–083713, 2009.

[36] A. F. Santander-Syro, O. Copie, T. Kondo, F. Fortuna, S. Pailhes, R. Weht, X. G. Qiu, F. Bertran, A. Nicolaou, A. Taleb-Ibrahimi, et al. Two-dimensional electron gas with universal subbands at the surface of $SrTiO_3$. *Nature*, 469(7329):189, 2011.

[37] D. Mora-Fonz, T. Lazauskas, M. R. Farrow, C. R. A. Catlow, S. M. Woodley, and A. A. Sokol. Why are polar surfaces of ZnO stable? *Chemistry of Materials*, 29(12):5306–5320, 2017.

[38] R. Eason. *Pulsed Laser Deposition of Thin Films*. John Wiley & Sons, 2007.

[39] L. Qiao, T. C. Droubay, V. Shutthanandan, Z. Zhu, P. V. Sushko, and S. A. Chambers. Thermodynamic instability at the stoichiometric $LaAlO_3/SrTiO_3$ (001) interface. *Journal of Physics: Condensed Matter*, 22(31):312201, 2010.

[40] H. Zaid, M. H. Berger, D. Jalabert, M. Walls, R. Akrobetu, I. Fongkaew, W. R. L. Lambrecht, N. J. Goble, X. P. A. Gao, P. Berger, et al. Atomic-resolved depth profile of strain and cation intermixing around $LaAlO_3/SrTiO_3$ interfaces. *Scientific Reports*, 6:28118, 2016.

[41] F. Schoofs, M. A. Carpenter, M. E. Vickers, M. Egilmez, T. Fix, J. E. Kleibeuker, J. L. MacManus-Driscoll, and M. G. Blamire. Carrier density modulation by structural distortions at modified $LaAlO_3/SrTiO_3$ interfaces. *Journal of Physics: Condensed Matter*, 25(17):175005, 2013.

[42] P. R. Willmott, S. A. Pauli, R. Herger, C. M. Schlepütz, D. Martoccia, B. D. Patterson, B. Delley, R. Clarke, D. Kumah, C. Cionca, et al. Structural basis for the conducting interface between $LaAlO_3$ and $SrTiO_3$. *Physical Review Letters*, 99(15):155502, 2007.

[43] J. B. Goodenough. Perspective on Engineering Transition-Metal Oxides. *Chemistry of Materials*, 26(1):820–829, 2014.

[44] M. Imada, A. Fujimori, and Y. Tokura. Metal-insulator transitions. *Reviews of Modern Physics*, 70(4):1039, 1998.

[45] U. Aschauer, R. Pfenninger, S. M. Selbach, T. Grande, and N. A. Spaldin. Strain-controlled oxygen vacancy formation and ordering in $CaMnO_3$. *Physical Review B*, 88:054111, 2013.

[46] I. Cherair, E. Bousquet, M. M. Schmitt, N. Iles, and A. Kellou. First-principles study of strain-induced jahn–teller distortions in $BaFeO_3$. *Journal of Physics: Condensed Matter*, 30(25):255701, 2018.

[47] A. Herklotz, A. T. Wong, T. Meyer, M. D. Biegalski, H. N. Lee, and T. Z. Ward. Controlling octahedral rotations in a perovskite via strain doping. *Scientific Reports*, 6:26491, 2016.

[48] J. M. Rondinelli and C. J. Fennie. Octahedral rotation-induced ferroelectricity in cation ordered perovskites. *Advanced Materials*, 24(15):1961–1968, 2012.

[49] X. Zhai, L. Cheng, Y. Liu, C. M. Schlepütz, S. Dong, H. Li, X. Zhang, S. Chu, L. Zheng, J. Zhang, et al. Correlating interfacial octahedral rotations with magnetism in $(LaMnO_{3+\delta})_N/(SrTiO_3)_N$ superlattices. *Nature Communications*, 5:4283, 2014.

[50] Y. Yang Zhang, R. Mishra, T. J. Pennycook, A. Y. Borisevich, S. J. Pennycook, and S. T. Pantelides. Oxygen disorder, a way to accommodate large epitaxial strains in oxides. *Advanced Materials Interfaces*, 2(18):1500344, 2015.

[51] J. R. Petrie, C. Mitra, H. Jeen, W. S. Choi, T. L. Meyer, F. A. Reboredo, J. W. Freeland, G. Eres, and H. N. Lee. Strain Control of Oxygen Vacancies in Epitaxial Strontium Cobaltite Films. *Advanced Functional Materials*, 26(10):1564–1570, 2016.

[52] C. Becher, L. Maurel, U. Aschauer, M. Lilienblum, C. Magén, D. Meier, E. Langenberg, M. Trassin, J. Blasco, I. P. Krug, et al. Strain-induced coupling of electrical polarization and structural defects in $SrMnO_3$ films. *Nature Nanotechnology*, 10(8):661, 2015.

[53] J. B. Goodenough, J-S. Zhou, F. Rivadulla, and E. Winkler. Bond-length fluctuations in transition-metal oxoperovskites. *Journal of Solid State Chemistry*, 175(1):116–123, 2003.

[54] R. D. Shannon. Revised effective ionic radii and systematic studies of interatomic distances in halides and chalcogenides. *Acta crystallographica section A: crystal physics, diffraction, theoretical and general crystallography*, 32(5):751–767, 1976.

[55] A. Kumar, A. S. Verma, and S. R. Bhardwaj. Prediction of formability in perovskite-type oxides. *The Open Applied Physics Journal*, 1(1), 2008.

[56] N. A. Benedek, A. T. Mulder, and C. J. Fennie. Polar octahedral rotations: a path to new multifunctional materials. *Journal of Solid State Chemistry*, 195:11–20, 2012.

[57] W. Lu, W. Song, P. Yang, J. Ding, G. M. Chow, and J. Chen. Strain engineering of octahedral rotations and physical properties of $SrRuO_3$ films. *Scientific Reports*, 5:10245, 2015.

[58] J. M. Rondinelli and N. A. Spaldin. Substrate coherency driven octahedral rotations in perovskite oxide films. *Physical Review B*, 82(11):113402, 2010.

[59] A. M. Glazer. The classification of tilted octahedra in perovskites. *Acta Crystallographica Section B*, 28(11):3384–3392, 1972.

[60] S. E. Rowley, L. J. Spalek, R. P. Smith, M. P. M. Dean, M. Itoh, J. F. Scott, G. G. Lonzarich, and S. S. Saxena. Ferroelectric quantum criticality. *Nature Physics*, 10(5):367, 2014.

[61] L. Bai, F. Polo-Garzon, Z. Bao, S. Luo, B. M. Moskowitz, H. Tian, and Z. Wu. Impact of surface composition of $SrTiO_3$ catalysts for oxidative coupling of methane. *ChemCatChem*, 11(8):2107–2117, 2019.

[62] Y. C. Lin, D. K. Wang, J. Y. Liu, A. Niaei, and H. H. Tseng. Low band-gap energy photocatalytic membrane based on $SrTiO_3$–Cr and PVDF substrate: BSA protein degradation and separation application. *Journal of Membrane Science*, 2019.

[63] Y. Tian, C. Adamo, D. G. Schlom, and K. S. Burch. Optical properties of $SrTiO_3$ on Silicon (100). *Applied Physics Letters*, 102(4):041906, 2013.

[64] Y. Yamada and Y. Kanemitsu. Band-to-band photoluminescence in $SrTiO_3$. *Physical Review B*, 82(12):121103, 2010.

[65] S. K. Hodak, T. Supasai, A. Wisitsoraat, and J. H. Hodak. Design of Low Cost Gas Sensor Based on $SrTiO_3$ and $BaTiO_3$ Films. *Journal of Nanoscience and Nanotechnology*, 10(11):7236–7238, 2010.

[66] B. R. Sudireddy and K. Agersted. Sintering and electrical characterization of La and Nb Co-doped $SrTiO_3$ electrode materials for solid oxide cell applications. *Fuel Cells*, 14(6):961–965, 2014.

[67] D. Fuchs, C. W. Schneider, R. Schneider, and H. Rietschel. High dielectric constant and tunability of epitaxial $SrTiO_3$ thin film capacitors. *Journal of Applied Physics*, 85(10):7362–7369, 1999.

[68] T. Yamada, K. F. Astafiev, V. O. Sherman, A. K. Tagantsev, D. Su, P. Muralt, and N. Setter. Structural and dielectric properties of strain-controlled epitaxial $SrTiO_3$ thin films by two-step growth technique. *Journal of Applied Physics*, 98(5):054105, 2005.

[69] J. F. Schooley, W. R. Hosler, and Marvin L. Cohen. Superconductivity in semiconducting $SrTiO_3$. *Physical Review Letters*, 12:474–475, 1964.

[70] J. K. Li, C. Ma, K. J. Jin, C. Ge, L. Gu, X. He, W. J. Zhou, Q. H. Zhang, H. B. Lu, and G. Z. Yang. Temperature-Dependent Resistance Switching in $SrTiO_3$. *Applied Physics Letters*, 108(24):10–15, 2016.

[71] Y. Pan, X.and Shuai, C. Wu, W. Luo, X. Sun, Y. Yuan, S. Zhou, X. Ou, and W. Zhang. Resistive Switching Behavior in Single Crystal $SrTiO_3$ Annealed by Laser. *Applied Surface Science*, 389:1104–1107, 2016.

[72] S. Wu, L. Ren, J. Qing, F. Yu, K. Yang, M. Yang, Y. Wang, M. Meng, W. Zhou, X. Zhou, and S. Li. Bipolar Resistance

Switching in Transparent ITO/$LaAlO_3$/$SrTiO_3$ Memristors. *ACS Applied Materials & Interfaces*, 6(11):8575–8579, 2014.

[73] T. Moon, H. J. Jung, Y. J. Kim, M. H. Park, and H. J. Kim. Research Update: Diode Performance of the Pt/Al_2O_3 /Two-Dimensional Electron Gas/$SrTiO_3$ Structure and its Time-Dependent Resistance Evolution. *APL Materials*, 5:042301, 2017.

[74] J. Park, D.-H. Kwon, H. Park, C.U. Jung, and M. Kim. Role of oxygen vacancies in resistive switching in Pt/Nb-doped $SrTiO_3$. *Applied Physics Letters*, 105(18):183103, 2014.

[75] K. Szot, W. Speier, G. Bihlmayer, and R. Waser. Switching the Electrical Resistance of Individual Dislocations in Single-Crystalline $SrTiO_3$. *Nature Materials*, 5(4):312–320, 2006.

[76] M. Andrä, F. Gunkel, C. Bäumer, C. Xu, R. Dittmann, and R. Waser. The influence of the local oxygen vacancy concentration on the piezoresponse of strontium titanate thin films. *Nanoscale*, 7:14351–14357, 2015.

[77] P. Sharma, S. Ryu, J. D. Burton, T. R. Paudel, C. W. Bark, Z. Huang, Ariando, E. Y. Tsymbal, G. Catalan, C. B. Eom, and A. Gruverman. Mechanical Tuning of $LaAlO_3$/$SrTiO_3$ Interface Conductivity. *Nano Letters*, 15(5):3547–3551, 2015.

[78] T. Mitsui and W. B. Westphal. Dielectric and x-ray studies of $Ca_xBa_{1-x}TiO_3$ and $Ca_xSr_{1-x}TiO_3$. *Physical Review*, 124(5):1354, 1961.

[79] A. Durán, E. Martínez, J. A. Díaz, and J. M. Siqueiros. Ferroelectricity at room temperature in Pr-doped $SrTiO_3$. *Journal of Applied Physics*, 97(10):104109, 2005.

[80] P. A. Fleury and J. M. Worlock. Electric-field-induced Raman scattering in $SrTiO_3$ and $KTaO_3$. *Physical Review*, 174(2):613, 1968.

[81] M. Itoh, R. Wang, Y. Inaguma, T. Yamaguchi, Y. J. Shan, and T. Nakamura. Ferroelectricity induced by oxygen isotope exchange in strontium titanate perovskite. *Physical Review Letters*, 82(17):3540, 1999.

[82] J. H. Haeni, P. Irvin, W. Chang, R. Uecker, P. Reiche, Y. L. Li, S. Choudhury, W. Tian, M. E. Hawley, B. Craigo, et al. Room-Temperature Ferroelectricity in Strained $SrTiO_3$. *Nature*, 430(7001):758–761, 2004.

[83] H. W. Jang, A. Kumar, S. Denev, M. D. Biegalski, P. Maksymovych, C. W. Bark, C. T. Nelson, C. M. Folkman, S. H. Baek, N. Balke, C. M. Brooks, D. A. Tenne, D. G. Schlom, L. Q. Chen, X. Q. Pan, S. V. Kalinin, V. Gopalan, and C. B. Eom. Ferroelectricity in strain-free $SrTiO_3$ thin films. *Physical Review Letters*, 104:197601, 2010.

[84] D. Zou, Y. Liu, S. Xie, J. Lin, and J. Li. Effect of strain on thermoelectric properties of $SrTiO_3$: First-principles calculations. *Chemical Physics Letters*, 586:159–163, 2013.

[85] T. T. Khan, I. H. Kim, and S. C. Ur. Improvement of the thermoelectric properties of the perovskite $SrTiO_3$ by Cr-doping. *Journal of Electronic Materials*, 48(4):1864–1869, 2019.

[86] H. Ohta, S. Kim, Y. Mune, T. Mizoguchi, K. Nomura, S. Ohta, T. Nomura, Y. Nakanishi, Y. Ikuhara, M. Hirano, et al. Giant thermoelectric Seebeck coefficient of a two-dimensional electron gas in $SrTiO_3$. *Nature Materials*, 6(2):129, 2007.

[87] H. Ohta, T. Mizuno, S. Zheng, T. Kato, Y. Ikuhara, K. Abe, H. Kumomi, K. Nomura, and H. Hosono. Unusually large enhancement of thermopower in an electric field induced two-dimensional electron gas. *Advanced Materials*, 24(6):740–744, 2012.

[88] A. Biswas, C.-H. Yang, R. Ramesh, and Y. H. Jeong. Atomically flat single terminated oxide substrate surfaces. *Progress in Surface Science*, 92(2):117 – 141, 2017.

[89] G. N. Greaves, A. L. Greer, R. S. Lakes, and T. Rouxel. Poisson's ratio and modern materials. *Nature Materials*, 10(11):823, 2011.

[90] H. Ledbetter, M. Lei, and S. Kim. Elastic constants, Debye temperatures, and electron-phonon parameters of superconducting cuprates and related oxides. *Phase Transitions: A Multinational Journal*, 23(1):61–70, 1990.

[91] M. Birkholz. *Thin Film Analysis by X-Ray Scattering*. Wiley, 2006.

[92] W. Lu, P. Yang, G. M. Song, W. D.and Chow, and J. S. Chen. Control of oxygen octahedral rotations and physical properties in $SrRuO_3$ films. *Physical Review B*, 88:214115, 2013.

[93] M. Yasaka. X-Ray thin film measurement techniques. *The Rigaku Journal*, 26(2):1–9, 2010.

[94] G. Binnig, C. F. Quate, and C. Gerber. Atomic force microscope. *Physical Review Letters*, 56:930–933, 1986.

[95] Y. Seo and W. Jhe. Atomic force microscopy and spectroscopy. *Reports on Progress in Physics*, 71(1):016101, 2008.

[96] Wilhelm Melitz, Jian Shen, Andrew C. Kummel, and Sangyeob Lee. Kelvin Probe Force Microscopy and its Application. *Surface Science Reports*, 66(1):1–27, 2011.

[97] L. Collins, A. Belianinov, S. Somnath, N. Balke, S. V. Kalinin, and S. Jesse. Full Data Acquisition in Kelvin Probe Force Microscopy: Mapping Dynamic Electric Phenomena in Real Space. *Scientific Reports*, 6(1):30557, 2016.

[98] S. V. Kalinin and D. A. Bonnell. Local potential and polarization screening on ferroelectric surfaces. *Physical Review B*, 63(12):125411, 2001.

[99] L. J. van der Pauw. A method of measuring the resistivity and hall coefficient on lamellae of arbitrary shape. *Philips Technical Review*, 20:220–224, 1958.

[100] C. Kittel, P. McEuen, and P. McEuen. *Introduction to solid state physics*, volume 8. Wiley New York, 1976.

[101] N. F. Mott and H. Jones. *The theory of the properties of metals and alloys*. Courier Corporation, 1958.

[102] S. Singh and S. K. Pandey. Fabrication of a simple apparatus for the Seebeck coefficient measurement in high temperature region. *Measurement*, 102:26 – 32, 2017.

[103] Q. Fu, Y. Xiong, W. Zhang, and D. Xu. A setup for measuring the Seebeck coefficient and the electrical resistivity of bulk thermoelectric materials. *Review of Scientific Instruments*, 88(9):095111, 2017.

[104] K. A. Borup, J. De Boor, H. Wang, F. Drymiotis, F. Gascoin, X. Shi, L. Chen, M. I. Fedorov, E. Müller, B. B. Iversen, et al. Measuring thermoelectric transport properties of materials. *Energy & Environmental Science*, 8(2):423–435, 2015.

[105] C. Wang, K. Chen, F.and Sun, R. Chen, M. Li, X. Zhou, Y. Sun, D. Chen, and G. Wang. Contributed review: Instruments for measuring Seebeck coefficient of thin film thermoelectric materials: A mini-review. *Review of Scientific Instruments*, 89(10):101501, 2018.

[106] A. Sarantopoulos, E. Ferreiro-Vila, V. Pardo, C. Magén, M. H. Aguirre, and F. Rivadulla. Electronic degeneracy and intrinsic magnetic properties of epitaxial Nb:$SrTiO_3$ thin films controlled by defects. *Physical Review Letters*, 115:166801, 2015.

[107] P. Hohenberg and W. Kohn. Inhomogeneous electron gas. *Physical Review*, 136:B864–B871, 1964.

[108] W. Kohn and L. J. Sham. Self-consistent equations including exchange and correlation effects. *Physical Review*, 140(4A):A1133, 1965.

[109] M. Born and R. Oppenheimer. Zur quantentheorie der molekeln. *Annalen der Physik*, 389(20):457–484, 1927.

[110] L. H. Thomas. The calculation of atomic fields. *Mathematical Proceedings of the Cambridge Philosophical Society*, 23(5):542–548, 1927.

[111] E. Fermi. Un metodo statistico per la determinazione di alcune priopretá dell'atomo. *Accademia Nazionale dei Lincei*, 6:602–607, 1927.

[112] V. Fock. Näherungsmethode zur lösung des quantenmechanischen mehrkörperproblems. *Zeitschrift für Physik*, 61(1):126–148, 1930.

[113] R. M. Martin. *Electronic Structure: Basic Theory and Practical Methods*. Cambridge University Press, 2004.

[114] J. P. Perdew. Accurate density functional for the energy: Real-space cutoff of the gradient expansion for the exchange hole. *Physical Review Letters*, 55:1665–1668, 1985.

[115] V. I. Anisimov, J. Zaanen, and O. K. Andersen. Band theory and mott insulators: Hubbard u instead of Stoner i. *Physical Review B*, 44:943–954, 1991.

[116] A. D. Becke. A new mixing of hartree-fock and local density-functional theories. *Journal of Chemical Physics*, 98:1372–1377, 1993.

[117] J. P. Perdew, K. Burke, and M. Ernzerhof. Generalized gradient approximation made simple. *Physical Review Letters*, 77:3865–3868, 1996.

[118] J. P. Perdew, A. Ruzsinszky, G. I. Csonka, O. A. Vydrov, G. E. Scuseria, L. A. Constantin, X. Zhou, and K. Burke. Restoring the density-gradient expansion for exchange in solids and surfaces. *Physical Review Letters*, 100:136406, 2008.

[119] K. Schwarz and P. Blaha. Solid state calculations using Wien2k. *Computational Materials Science*, 28(2):259–273, 2003.

[120] G. Kresse and J. Furthmüller. Efficient iterative schemes for ab initio total-energy calculations using a plane-wave basis set. *Physical Review B*, 54:11169–11186, 1996.

[121] E. Sjöstedt, L Nordström, and D. J Singh. An alternative way of linearizing the augmented plane-wave method. *Solid State Communications*, 114(1):15 – 20, 2000.

[122] P. Blaha, K. Schwarz, G. K. H. Madsen, D. Kvasnicka, and J. Luitz. *WIEN2K, An Augmented Plane Wave + Local Orbitals Program for Calculating Crystal Properties*. Karlheinz Schwarz, Techn. Universität Wien, Austria, 2001.

[123] K. Schwarz, P. Blaha, and G. K. H. Madsen. Electronic structure calculations of solids using the Wien2k package for material sciences. *Computer Physics Communications*, 147(1):71 – 76, 2002. Proceedings of the Europhysics Conference on Computational Physics Computational Modeling and Simulation of Complex Systems.

[124] S. Cottenier. *Density Functional Theory and the family of (L)APW-methods: a step-by-step introduction*. Instituut voor Kern- en Stralingsfysica, K.U.Leuven, Belgium, 2002.

[125] R. D. King-Smith and D. Vanderbilt. Theory of polarization of crystalline solids. *Physical Review B*, 47:1651–1654, 1993.

[126] D. Vanderbilt and R. D. King-Smith. Electric polarization as a bulk quantity and its relation to surface charge. *Physical Review B*, 48:4442–4455, 1993.

[127] M. V. Berry. Quantal phase factors accompanying adiabatic changes. *Proceedings of the Royal Society of London. A. Mathematical and Physical Sciences*, 392(1802):45–57, 1984.

[128] N. A. Spaldin. A beginner's guide to the modern theory of polarization. *Journal of Solid State Chemistry*, 195:2 – 10, 2012.

[129] R. People and J. C. Bean. Calculation of critical layer thickness versus lattice mismatch for Ge_xSi_{1-x}/Si strained-layer heterostructures. *Applied Physics Letters*, 47(3):322–324, 1985.

[130] J. W. Matthews, S. Mader, and T. B. Light. Accommodation of misfit across the interface between crystals of semiconducting elements or compounds. *Journal of Applied Physics*, 41(9):3800–3804, 1970.

[131] N. Schichtel, C. Korte, D. Hesse, and J. Janek. Elastic strain at interfaces and its influence on ionic conductivity in nanoscaled solid electrolyte thin films-theoretical considerations and experimental studies. *Physical Chemistry Chemical Physics*, 11(17):3043–3048, 2009.

[132] Q. Yang, J. X. Cao, Y. C. Zhou, Y. Zhang, Y. Ma, and X. J. Lou. Tunable oxygen vacancy configuration by strain engineering in perovskite ferroelectrics from first-principles study. *Applied Physics Letters*, 103(14):142911, 2013.

[133] J. Gazquez, Shameek Bose, M. Sharma, M. A. Torija, S. J. Pennycook, C. Leighton, and M. Varela. Lattice mismatch accommodation via oxygen vacancy ordering in epitaxial $La_{0.5}Sr_{0.5}CoO_{3-\delta}$ thin films. *APL Mater.*, 1(1), 2013.

[134] J. R. Petrie, H. Jeen, S. C. Barron, T. L. Meyer, and H. N. Lee. Enhancing perovskite electrocatalysis through strain tuning of

the oxygen deficiency. *Journal of the American Chemical Society*, 138(23):7252–7255, 2016. PMID: 27232374.

[135] J. M. Rondinelli and N. A. Nicola. Structure and properties of functional oxide thin films: Insights from electronic-structure calculations. *Advanced Materials*, 23:3363–3381, 2011.

[136] W. S. Choi, C. M. Rouleau, S. S. A Seo, Z. Luo, H. Zhou, T. T. Fister, J. A. Eastman, P. H. Fuoss, D. D. Fong, J. Z. Tischler, et al. Atomic layer engineering of perovskite oxides for chemically sharp heterointerfaces. *Advanced Materials*, 24(48):6423–6428, 2012.

[137] F. V. E. Hensling, C. Xu, F. Gunkel, and R. Dittmann. Unraveling the enhanced oxygen vacancy formation in complex oxides during annealing and growth. *Scientific Reports*, 7:39953, 2017.

[138] D. Li, S. Gariglio, C. Cancellieri, A. Fête, D. Stornaiuolo, and J. M. Triscone. Fabricating superconducting interfaces between artificially grown $LaAlO_3$ and $SrTiO_3$ thin films. *APL Materials*, 2(1):012102, 2014.

[139] P. P. Balakrishnan, M. J. Veit, U. S. Alaan, M. T. Gray, and Y. Suzuki. Metallicity in $SrTiO_3$ substrates induced by pulsed laser deposition. *APL Materials*, 7(1):011102, 2019.

[140] Y. Z. Chen, M. Döbeli, E. Pomjakushina, Y. L. Gan, N. Pryds, and T. Lippert. Scavenging of oxygen vacancies at modulation-doped oxide interfaces: Evidence from oxygen isotope tracing. *Physical Review Materials*, 1(5):052002, 2017.

[141] R. F. Berger, C. J. Fennie, and J. B. Neaton. Band gap and edge engineering via ferroic distortion and anisotropic strain: The case of $SrTiO_3$. *Physical Review Letters*, 107:146804, 2011.

[142] N. Tsuda, K. Nasu, A. Yanase, and K. Siratori. *Electronic Conduction in Oxides*. Springer-Verlag, Berlin Heidelberg, 1991.

[143] J. B. Goodenough. Oxide-ion electrolytes. *Annual Review of Materials Research*, 33(1):91–128, 2003.

[144] R. A. De Souza, V. Metlenko, D. Park, and T. E. Weirich. Behavior of oxygen vacancies in single-crystal $SrTiO_3$: Equilibrium distribution and diffusion kinetics. *Physical Review B*, 85:174109, 2012.

[145] H. A. Tahini, X. Tan, U. Schwingenschlögl, and S. C. Smith. Formation and migration of oxygen vacancies in $SrCoO_3$ and their effect on oxygen evolution reactions. *ACS Catalysis*, 6(8):5565–5570, 2016.

[146] M. Kareev, S. Prosandeev, J. Liu, C. Gan, A. Kareev, J. W. Freeland, M. Xiao, and J. Chakhalian. Atomic control and characterization of surface defect states of TiO_2 terminated $SrTiO_3$ single crystals. *Applied Physics Letters*, 93(6):061909, 2008.

[147] D. S. Aidhy, B. Liu, Y. Zhang, and W. J. Weber. Chemical expansion affected oxygen vacancy stability in different oxide structures from first principles calculations. *Computational Materials Science*, 99:298–305, 2015.

[148] H. Kim, J. Y Zhang, S. Raghavan, and S. Stemmer. Direct observation of sr vacancies in $SrTiO_3$ by quantitative scanning transmission electron microscopy. *Physical Review X*, 6(4):041063, 2016.

[149] Y. Tokuda, S. Kobayashi, T. Ohnishi, T. Mizoguchi, N. Shibata, Y. Ikuhara, and T. Yamamoto. Strontium vacancy clustering in Ti-excess $SrTiO_3$ thin film. *Applied Physics Letters*, 99(3):033110, 2011.

[150] R. Moos and K. H. Hardtl. Defect chemistry of donor-doped and undoped Strontium Titanate ceramics between 1000° and 1400°C. *Journal of the American Ceramic Society*, 80(10):2549–2562, 1997.

[151] N. G. Eror and U. Balachandran. High-temperature defect structure of acceptor-doped Strontium Titanate. *Journal of the American Ceramic Society*, 65(9):426–431, 1982.

[152] S. Y. Choi, S. D. Kim, M. Choi, H. S. Lee, J. Ryu, N. Shibata, T. Mizoguchi, E. Tochigi, T. Yamamoto, S. J. L. Kang, and Y. Ikuhara. Assessment of strain-generated oxygen vacancies using $SrTiO_3$ bicrystals. *Nano Letters*, 15(6):4129–4134, 2015.

[153] R. U. Chandrasena, W. Yang, Q. Lei, M. U. Delgado-Jaime, K. D. Wijesekara, M. Golalikhani, Br. A. Davidson, E. Arenholz, K. Kobayashi, M. Kobata, F. M. F. De Groot, U. Aschauer, N. A. Spaldin, X. Xi, and A. X. Gray. Strain-Engineered Oxygen Vacancies in $CaMnO_3$ Thin Films. *Nano Letters*, 17(2):794–799, 2017.

[154] Q. Yang, J. X. Cao, Y. Ma, Y. C. Zhou, L. M. Jiang, and X. L. Zhong. Strain effects on formation and migration energies of oxygen vacancy in perovskite ferroelectrics: A first-principles study. *Journal of Applied Physics*, 113(18):184110, 2013.

[155] R. Waser and M. Aono. Nanoionics-Based Resistive Switching Memories. *Nature Materials*, 6(11):833–840, 2007.

[156] A. Sawa. Resistive Switching in Transition Metal Oxides. *Materials Today*, 11(6):28–36, 2008.

[157] S. V. Kalinin and N. A. Spaldin. Functional Ion Defects in Transition Metal Oxides. *Science*, 341(6148):858–859, 2013.

[158] R. Waser, R. Dittmann, C. Staikov, and K. Szot. Redox-Based Resistive Switching Memories Nanoionic Mechanisms, Prospects, and Challenges. *Advanced Materials*, 21(25-26):2632–2663, 2009.

[159] H. Lu, C.-W. Bark, D. E. De Los Ojos, J. Alcala, C. B. Eom, G. Catalan, and A. Gruverman. Mechanical writing of ferroelectric polarization. *Science*, 336(6077):59–61, 2012.

[160] S. Das, B. Wang, Y. Cao, M. Rae Cho, Y. Jae Shin, S. Mo Yang, L. Wang, M. Kim, S. V. Kalinin, L.-Q. Chen, and T. W. Noh. Controlled Manipulation of Oxygen Vacancies Using Nanoscale Flexoelectricity. *Nature Communications*, 8(1):615, 2017.

[161] D. C. Johnson and A. L. Prieto. Use of Strontium Titanate ($SrTiO_3$) as an Anode Material for Lithium-Ion Batteries. *Journal of Power Sources*, 196(18):7736–7741, 2011.

[162] Y. Hu, O. K. Tan, W. Cao, and W. Zhu. A low temperature nanostructured $SrTiO_3$ thick film oxygen gas sensor. *Ceramics International*, 30(7):1819–1822, 2004.

[163] A. Bera, K. Wu, A. Sheikh, E. Alarousu, O. F. Mohammed, and T. Wu. Perovskite oxide $SrTiO_3$ as an efficient electron transporter for hybrid perovskite solar cells. *The Journal of Physical Chemistry C*, 118(49):28494–28501, 2014.

[164] S. V. Kalinin and D. A. Bonnell. Surface potential at surface-interface junctions in $SrTiO_3$ bicrystals. *Physical Review B*, 62(15):10419, 2000.

[165] C. Villeneuve-Faure, K. Makasheva, L. Boudou, and G. Teyssedre. Charge Injection in Thin Dielectric Layers by Atomic Force Microscopy: Influence of Geometry and Material Work Function of the AFM Tip on the Injection Process. *Nanotechnology*, 27(24):245702, 2016.

[166] E. Rowicka, D. Kashyn, M. A. Reagan, T. Hirano, P. B. Paramonov, I. Dolog, R. R. Mallik, and S. F. Lyuksyutov. Influence of Water Condensation on Charge transport and Electric Breakdown Between an Atomic Force Microscope Tip, Polymeric, and Semiconductor CdS Surfaces. *Current Nanoscience*, 4(2):166, 2008.

[167] N. Yang, S. Doria, A. Kumar, J. H. Jang, T. M. Arruda, A. Tebano, S. Jesse, I. N. Ivanov, A. P. Baddorf, E. Strelcov,

et al. Water-mediated electrochemical nano-writing on thin Ceria films. *Nanotechnology*, 25(7):075701, 2014.

[168] P. Girard. Electrostatic force microscopy: principles and some applications to semiconductors. *Nanotechnology*, 12(4):485–490, 2001.

[169] M. Kubicek, Z. Cai, W. Ma, B. Yildiz, H. Hutter, and J. Fleig. Tensile lattice strain accelerates oxygen surface exchange and diffusion in $La_{1-x}Sr_xCoO_3$ thin films. *ACS Nano*, 7(4):3276–3286, 2013. PMID: 23527691.

[170] J. Crank. *The Mathematics of Diffusion*. Clarendon Press, 1975.

[171] R. Merkle and J. Maier. How is Oxygen Incorporated into Oxides? A Comprehensive Kinetic Study of a Simple Solid-State Reaction with $SrTiO_3$ as a Model Material. *Angewandte Chemie - International Edition*, 47(21):3874–3894, 2008.

[172] S. Hu, Y. Wang, C. Cazorla, and J. Seidel. Strain-enhanced oxygen dynamics and redox reversibility in topotactic $SrCoO_{3-\delta}$. *Chemistry of Materials*, 29(2):708–717, 2017.

[173] M. J. D. Rushton and A. Chroneos. Impact of uniaxial strain and doping on oxygen diffusion in CeO_2. *Scientific Reports*, 4:6068, 2014.

[174] R. AL-Hamadany, J. P. Goss, P. R. Briddon, S. A. Mojarad, A. G. O'Neill, and M. J. Rayson. Impact of Tensile Strain on the Oxygen Vacancy Migration in $SrTiO_3$: Density Functional Theory Calculations. *Journal of Applied Physics*, 113(22):224108, 2013.

[175] R. Al-Hamadany, J. P. Goss, P. R. Briddon, S. A. Mojarad, M. Al-Hadidi, A. G. O'Neill, and M. J. Rayson. Oxygen Vacancy Migration in Compressively Strained $SrTiO_3$. *Journal of Applied Physics*, 113(2):0–8, 2013.

[176] A. Vailionis, H. Boschker, W. Siemons, E. P. Houwman, David H. A. Blank, G. Rijnders, and G. Koster. Misfit strain accommodation in epitaxial ABO_3 perovskites: Lattice rotations and lattice modulations. *Physical Review B*, 83(6):064101, 2011.

[177] L. Qiao, J. Hyuck Jang, D. J. Singh, Z. Gai, H. Xiao, A. Mehta, R. K. Vasudevan, A. Tselev, Z. Feng, H. Zhou, et al. Dimensionality controlled octahedral symmetry-mismatch and functionalities in epitaxial $LaCoO_3$/$SrTiO_3$ heterostructures. *Nano Letters*, 15(7):4677–4684, 2015.

[178] Z. Liao, M. Huijben, Z. Zhong, N. Gauquelin, S. Macke, R. J. Green, S. Van Aert, J. Verbeeck, G. Van Tendeloo, K. Held, et al. Controlled lateral anisotropy in correlated manganite heterostructures by interface-engineered oxygen octahedral coupling. *Nature Materials*, 15(4):425, 2016.

[179] X. Z. Lu, X. G. Gong, and H. J. Xiang. Polarization enhancement in perovskite superlattices by oxygen octahedral tilts. *Computational Materials Science*, 91:310–314, 2014.

[180] A. Marthinsen, C. Faber, U. Aschauer, N. A. Spaldin, and S. M. Selbach. Coupling and competition between ferroelectricity, magnetism, strain, and oxygen vacancies in $AMnO_3$ perovskites. *MRS Communications*, 6(3):182–191, 2016.

[181] M. Choi, F. Oba, Y. Kumagai, and I. Tanaka. Anti-ferrodistortive-like oxygen-octahedron rotation induced by the oxygen vacancy in cubic $SrTiO_3$. *Advanced Materials*, 25(1):86–90, 2013.

[182] H. Sim and B. G. Kim. First-principles study of octahedral tilting and ferroelectric-like transition in metallic $LiOsO_3$. *Physical Review B*, 89(20):201107, 2014.

[183] P. Sharma, S. Ryu, Z. Viskadourakis, T. R. Paudel, H. Lee, C. Panagopoulos, E. Y. Tsymbal, C. B. Eom, and A. Gruverman. Electromechanics of ferroelectric-like behavior of $LaAlO_3$

thin films. *Advanced Functional Materials*, 25(41):6538–6544, 2015.

[184] C. W. Bark, P. Sharma, Y. Wang, S. H. Baek, S. Lee, S. Ryu, C. M. Folkman, T. R. Paudel, A. Kumar, S. V. Kalinin, et al. Switchable induced polarization in $LaAlO_3/SrTiO_3$ heterostructures. *Nano Letters*, 12(4):1765–1771, 2012.

[185] M. D'iorio, W. Berlinger, and K. A. Müller. Characterization of the 105 K phase transition in flux-grown $SrTiO_3$. *Phase Transitions*, 4(1):31–36, 1983.

[186] S. Piskunov, E. Heifets, R. I. Eglitis, and G. Borstel. Bulk properties and electronic structure of $SrTiO_3$, $BaTiO_3$, $PbTiO_3$ perovskites: an ab initio HF/DFT study. *Computational Materials Science*, 29(2):165–178, 2004.

[187] D. Ricci, G. Bano, G. Pacchioni, and F. Illas. Electronic structure of a neutral oxygen vacancy in $SrTiO_3$. *Physical Review B*, 68(22):224105, 2003.

[188] M. Moreau, A. Marthinsen, S. M. Selbach, and T. Tybell. First-principles study of the effect of (111) strain on octahedral rotations and structural phases of $LaAlO_3$. *Physical Review B*, 95(6):064109, 2017.

[189] T. T. Fister, H. Zhou, Z. Luo, S. S. A. Seo, S. O. Hruszkewycz, D. L. Proffit, J. A. Eastman, P. H. Fuoss, P. M. Baldo, H. N. Lee, et al. Octahedral rotations in strained $LaAlO_3/SrTiO_3$ (001) heterostructures. *APL Materials*, 2(2):021102, 2014.

[190] N. Balke, I. Bdikin, S. V. Kalinin, and A. L. Kholkin. Electromechanical imaging and spectroscopy of ferroelectric and piezoelectric materials: state of the art and prospects for the future. *Journal of the American Ceramic Society*, 92(8):1629–1647, 2009.

[191] A. L. Kholkin, V. V. Shvartsman, D. A. Kiselev, and I. K. Bdikin. Nanoscale characterization of ferroelectric materials for piezoelectric applications. *Ferroelectrics*, 341(1):3–19, 2006.

[192] O. Kolosov, A. Gruverman, J. Hatano, K. Takahashi, and H. Tokumoto. Nanoscale visualization and control of ferroelectric domains by atomic force microscopy. *Physical Review Letters*, 74(21):4309, 1995.

[193] N. Balke, P. Maksymovych, S. Jesse, A. Herklotz, A. Tselev, C. B. Eom, I. I. Kravchenko, P. Yu, and S. V. Kalinin. Differentiating ferroelectric and nonferroelectric electromechanical effects with scanning probe microscopy. *ACS Nano*, 9(6):6484–6492, 2015.

[194] S. V. Kalinin, S. Jesse, A. Tselev, A. P. Baddorf, and N. Balke. The role of electrochemical phenomena in scanning probe microscopy of ferroelectric thin films. *ACS Nano*, 5(7):5683–5691, 2011.

[195] D. Seol, S. Park, O. V. Varenyk, S. Lee, H. N. Lee, A. N. Morozovska, and Y. Kim. Determination of ferroelectric contributions to electromechanical response by frequency dependent piezoresponse force microscopy. *Scientific Reports*, 6:30579, 2016.

[196] S. V. Kalinin and D. A. Bonnell. Contrast mechanism maps for piezoresponse force microscopy. *Journal of Materials Research*, 17(5):936–939, 2002.

[197] N. Balke, S. Maksymovych, P.and Jesse, I. I. Kravchenko, Q. Li, and S. V. Kalinin. Exploring local electrostatic effects with scanning probe microscopy: implications for piezoresponse force microscopy and triboelectricity. *ACS Nano*, 8(10):10229–10236, 2014.

[198] N. Balke, S. Kalnaus, N. J. Dudney, C. Daniel, S. Jesse, and S. V. Kalinin. Local detection of activation energy for ionic transport in lithium cobalt oxide. *Nano Letters*, 12(7):3399–3403, 2012.

[199] Y. Zhang, J. Sun, J. P. Perdew, and X. Wu. Comparative first-principles studies of prototypical ferroelectric materials by LDA, GGA, and SCAN meta-GGA. *Physical Review B*, 96:035143, 2017.

[200] D. I. Bilc, R. Orlando, R. Shaltaf, G. M. Rignanese, J. Íñiguez, and P. Ghosez. Hybrid exchange-correlation functional for accurate prediction of the electronic and structural properties of ferroelectric oxides. *Physical Review B*, 77:165107, 2008.

[201] H. T. Stokes, E. H. Kisi, D. M. Hatch, and C. J. Howard. Group-theoretical analysis of octahedral tilting in ferroelectric perovskites. *Acta Crystallographica Section B: Structural Science*, 58(6):934–938, 2002.

[202] A. I. Lebedev. Metastability effects in strained and stressed $SrTiO_3$ films. *Journal of Advanced Dielectrics*, 6(03):1650016, 2016.

[203] C. H. Lin, C. M. Huang, and G. Y. Guo. Systematic ab initio study of the phase diagram of epitaxially strained $SrTiO_3$. *Journal of Applied Physics*, 100(8):084104, 2006.

[204] H. T. Stokes, D. M. Hatch, and B. J. Campbell. Isotropy software suite, iso. byu. edu.

[205] M. Alfredsson, K. Hermansson, and R. Dovesi. Periodic ab initio calculations of the spontaneous polarisation in ferroelectric $NaNO_2$. *Physical Chemistry Chemical Physics*, 4(17):4204–4211, 2002.

[206] T. Gohda, M. Ichikawa, T. Gustafsson, and I. Olovsson. X-ray study of deformation density and spontaneous polarization in ferroelectric $NaNO_2NaNO_2$. *Acta Crystallographica Section B: Structural Science*, 56(1):11–16, 2000.

[207] T. Yu, P. Gao, T. Wu, T. A. Tyson, and R. Lalancette. Ferroelectricity in single crystal $InMnO_3$. *Applied Physics Letters*, 102(17):172901, 2013.

[208] W. W. Peng, R. Tétot, G. Niu, E. Amzallag, B. Vilquin, J. B. Brubach, and P. Roy. Room-temperature soft mode and ferroelectric like polarization in $SrTiO_3$ ultrathin films: Infrared and ab initio study. *Scientific Reports*, 7(1):2160, 2017.

[209] M Scigaj, CH Chao, Jaume Gázquez, I Fina, Rahma Moalla, Guillaume Saint-Girons, MF Chisholm, G Herranz, J Fontcuberta, Romain Bachelet, et al. High ferroelectric polarization in c-oriented batio3 epitaxial thin films on srtio3/si (001). *Applied Physics Letters*, 109(12):122903, 2016.

[210] J. B. Neaton, C. Ederer, U. V. Waghmare, N. A. Spaldin, and K. M. Rabe. First-principles study of spontaneous polarization in multiferroic $BiFeO_3$. *Physical Review B*, 71(1):014113, 2005.

[211] B. Xu, V. Garcia, S. Fusil, M. Bibes, and L. Bellaiche. Intrinsic polarization switching mechanisms in $BiFeO_3$. *Physical Review B*, 95(10):104104, 2017.

[212] P. Baettig, C. Ederer, and N. A. Spaldin. First principles study of the multiferroics $BiFeO_3$, Bi_2FeO_6, and $BiFeCr_3$: Structure, polarization, and magnetic ordering temperature. *Physical Review B*, 72(21):214105, 2005.

[213] M. Li, J. Li, L. Q. Chen, B. L. Gu, and W. Duan. Effects of strain and oxygen vacancies on the ferroelectric and antiferrodistortive distortions in $PbTiO_3$/$SrTiO_3$ superlattice. *Physical Review B*, 92(11):115435, 2015.

[214] J. Kim, Y. M. Koo, K. S. Sohn, and N. Shin. Symmetry-mode analysis of the ferroelectric transition in $YMnO_3$. *Applied Physics Letters*, 97(9):092902, 2010.

[215] E. E. McCabe, E. Bousquet, C. P. J. Stockdale, C. A. Deacon, T. T. Tran, P. S. Halasyamani, M. C. Stennett, and N. C. Hyatt. Proper ferroelectricity in the Dion–Jacobson material $CsBi_2Ti_2NbO_{10}CsBi_2Ti_2NbO_{10}$: experiment and theory. *Chemistry of Materials*, 27(24):8298–8309, 2015.

[216] J. M. Perez-Mato, P. Blaha, K. Schwarz, M. Aroyo, D. Orobengoa, I. Etxebarria, and A. García. Multiple instabilities in $Bi_4Ti_3O_{12}$: a ferroelectric beyond the soft-mode paradigm. *Physical Review B*, 77(18):184104, 2008.

[217] D. Orobengoa, C. Capillas, M. I. Aroyo, and J. M. Perez-Mato. Amplimodes: symmetry-mode analysis on the bilbao crystallographic server. *Journal of Applied Crystallography*, 42(5):820–833, 2009.

[218] C. A. Jackson, J. Y. Zhang, C. R. Freeze, and S. Stemmer. Quantum critical behaviour in confined $SrTiO_3$ quantum wells embedded in antiferromagnetic $SmTiO_3$. *Nature Communications*, 5:4258, 2014.

[219] K. Han, N. Palina, S. W. Zeng, Z. Huang, C. J. Li, W. X. Zhou, D. Y. Wan, L. C. Zhang, X. Chi, R. Guo, et al. Controlling Kondo-like scattering at the $SrTiO_3$-based interfaces. *Scientific Reports*, 6:25455, 2016.

[220] S. Das, A. Rastogi, L. Wu, J. C. Zheng, Z. Hossain, Y. Zhu, and R. C. Budhani. Kondo scattering in δ-doped $LaAlO_3/SrTiO_3$ interfaces: Renormalization by spin-orbit interactions. *Physical Review B*, 90(8):081107, 2014.

[221] W. D. Rice, P. Ambwani, M. Bombeck, J. D. Thompson, G. Haugstad, C. Leighton, and S. A. Crooker. Persistent optically induced magnetism in oxygen-deficient strontium titanate. *Nature Materials*, 13(5):481, 2014.

[222] A. C. Hewson. *The Kondo problem to heavy fermions*, volume 2. Cambridge university press, 1997.

[223] M. Lee, J. R. Williams, S. Zhang, C. D. Frisbie, and D. Goldhaber-Gordon. Electrolyte gate-controlled Kondo effect in $SrTiO_3$. *Physical Review Letters*, 107(25):1–5, 2011.

[224] I. R. Shein and A. L. Ivanovskii. First principle prediction of vacancy-induced magnetism in non-magnetic perovskite $SrTiO_3$. *Physics Letters, Section A: General, Atomic and Solid State Physics*, 371(1-2):155–159, 2007.

[225] Z. Q. Liu, W. M. Lü, S. L. Lim, X. P. Qiu, N. N. Bao, M. Motapothula, J. B. Yi, M. Yang, S. Dhar, T. Venkatesan, et al. Reversible room-temperature ferromagnetism in Nb-doped $SrTiO_3$ single crystals. *Physical Review B*, 87(22):220405, 2013.

[226] A. D. Caviglia, M. Gabay, S. Gariglio, N. Reyren, C. Cancellieri, and J. M. Triscone. Tunable rashba spin-orbit interaction at oxide interfaces. *Physical Review Letters*, 104(12):126803, 2010.

[227] M. B. Shalom, M. Sachs, D. Rakhmilevitch, A. Palevski, and Y. Dagan. Tuning spin-orbit coupling and superconductivity at the $SrTiO_3$/$LaAlO_3$ interface: a magnetotransport study. *Physical Review Letters*, 104(12):126802, 2010.

[228] N. D. Mathur, F. M. Grosche, S. R. Julian, I. R. Walker, D. M. Freye, R. K. W. Haselwimmer, and G. G. Lonzarich. Magnetically mediated superconductivity in heavy fermion compounds. *Nature*, 394(6688):39, 1998.

[229] S. S. Saxena, P. Agarwal, K. Ahilan, F. M. Grosche, R. K. W. Haselwimmer, M. J. Steiner, E. Pugh, I. R. Walker, S. R. Julian, P. Monthoux, et al. Superconductivity on the border of itinerant-electron ferromagnetism in UGe_2. *Nature*, 406(6796):587, 2000.

[230] A. Baratoff and G. Binnig. Mechanism of superconductivity in $SrTiO_3$. *Physica B+C*, 108(1):1335 – 1336, 1981.

[231] K. Ahadi, L. Galletti, Y. Li, S. Salmani-Rezaie, W. Wu, and S. Stemmer. Enhancing superconductivity in $SrTiO_3$ films with strain. *Science Advances*, 5(4):eaaw0120, 2019.

[232] G. Bergmann. Physical interpretation of weak localization: A time-of-flight experiment with conduction electrons. *Physical Review B*, 28(6):2914, 1983.

[233] G. Bergmann. Consistent temperature and field dependence in weak localization. *Physical Review B*, 28(2):515, 1983.

[234] N. F. Mott. *Metal-Insulator Transitions*. Taylor and Francis Ltd, 1990.

[235] A. Manchon, H. C. Koo, J. Nitta, S. M. Frolov, and R. A. Duine. New perspectives for rashba spin–orbit coupling. *Nature Materials*, 14(9):871, 2015.

[236] R. J. Elliott. Theory of the effect of spin-orbit coupling on magnetic resonance in some semiconductors. *Physical Review*, 96(2):266, 1954.

[237] S. Hikami, A. I. Larkin, and Y. Nagaoka. Spin-orbit interaction and magnetoresistance in the two dimensional random system. *Progress of Theoretical Physics*, 63(2):707–710, 1980.

[238] G. Singh, A. Jouan, S. Hurand, C. Feuillet-Palma, P. Kumar, A. Dogra, R. Budhani, J. Lesueur, and N. Bergeal. Effect of disorder on superconductivity and rashba spin-orbit coupling in $LaAlO_3/SrTiO_3$ interfaces. *Physical Review B*, 96(2):024509, 2017.

[239] K. Narayanapillai, R. Go, G.and Ramaswamy, K. Gopinadhan, D. Go, H. Woo. Lee, T. Venkatesan, K. J. Lee, and H. Yang. Interfacial Rashba magnetoresistance of the two-dimensional electron gas at the $LaAlO_3/SrTiO_3$ interface. *Physical Review B*, 96(6):064401, 2017.

[240] John M Ziman. *Principles of the Theory of Solids*. Cambridge university press, 1979.

[241] A. Matthiessen. *Report of British Association*, 1862.

[242] P. Drude. Zur elektronentheorie der metalle. *Annalen der Physik*, 306(3):566–613, 1900.

[243] W. G. Baber. The contribution to the electrical resistance of metals from collisions between electrons. *Proceedings of the Royal Society of London*, 158(894):383–396, 1937.

[244] J. M. Ziman. *Electrons and Phonons: The Theory of Transport Phenomena in Solids*. International series of monographs on physics. Clarendon Press, 1960.

[245] M. J. Rice. Electron-electron scattering in transition metals. *Physical Review Letters*, 20(25):1439, 1968.

[246] M. W. Swift and C. G. Van de Walle. Conditions for T^2 resistivity from electron-electron scattering. *The European Physical Journal B*, 90(8):151, 2017.

[247] E. Langenberg, E. Ferreiro-Vila, V. Leborán, A. O. Fumega, V. Pardo, and F. Rivadulla. Analysis of the temperature dependence of the thermal conductivity of insulating single crystal oxides. *APL Materials*, 4(10):104815, 2016.

[248] X. Wang, M. Zhang, X. Tian, Y. Zhang, J. Gong, A. Rahman, R. Dai, Z. Wang, and Z. Zhang. Strain-induced conductivity accelerated recoveries in $LaAlO_3/SrTiO_3$ heterostructure with millimeter scale. *RSC Advances*, 8(66):37804–37810, 2018.

[249] X. Lin, B. Fauqué, and K. Behnia. Scalable T^2 resistivity in a small single-component Fermi surface. *Science*, 349(6251):945–948, 2015.

[250] D. van der Marel, J. L. M. van Mechelen, and I. I. Mazin. Common Fermi-liquid origin of T^2 resistivity and superconductivity in n-type $SrTiO_3$. *Physical Review B*, 84:205111, 2011.

[251] S. Stemmer and S. J. Allen. Non-fermi liquids in oxide heterostructures. *Reports on Progress in Physics*, 81(6):062502, 2018.

[252] X. Lin, C. W. Rischau, L. Buchauer, A. Jaoui, B. Fauqué, and K. Behnia. Metallicity without quasi-particles in room-temperature strontium titanate. *npj Quantum Materials*, 2(1):41, 2017.

[253] E. McCalla, M. N. Gastiasoro, G. Cassuto, R. M. Fernandes, and C. Leighton. Low-temperature specific heat of doped $SrTiO_3$: Doping dependence of the effective mass and Kadowaki-Woods scaling violation. *Physical Review Materials*, 3(2):022001, 2019.

[254] S. Mozaffari, S. Guchhait, and J. T. Markert. Spin–orbit interaction and kondo scattering at the $PrAlO_3/SrTiO_3$ interface: effects of oxygen content. *Journal of Physics: Condensed Matter*, 29(39):395002, 2017.

[255] W. N. Lin, J. F. Ding, S. X. Wu, Y. F. Li, J. Lourembam, S. Shannigrahi, S. J. Wang, and T. Wu. Electrostatic modulation of $LaAlO_3/SrTiO_3$ interface transport in an electric double-layer transistor. *Advanced Materials Interfaces*, 1(1):1300001, 2014.

[256] J. Kondo. Resistance Minimum in Dilute Magnetic Alloys. *Progress of Theoretical Physics*, 32(1):37–49, 07 1964.

[257] N. W. Ashcroft and N. D. Mermin. *Solid state physics*. 1976.

[258] T. A. Costi, A. C. Hewson, and V. Zlatic. Transport coefficients of the anderson model via the numerical renormalization group. *Journal of Physics: Condensed Matter*, 6(13):2519, 1994.

[259] T. P. Sarkar, K. Gopinadhan, M. Motapothula, S. Saha, Z. Huang, S. Dhar, A. Patra, W. M. Lu, F. Telesio, I. Pallecchi, et al. Unexpected observation of spatially separated Kondo scattering and ferromagnetism in Ta alloyed anatase TiO_2 thin films. *Scientific Reports*, 5:13011, 2015.

[260] E. Mikheev, S. Raghavan, J. Y. Zhang, P. B. Marshall, A. P. Kajdos, L. Balents, and S. Stemmer. Carrier density independent

scattering rate in $SrTiO_3$-based electron liquids. *Scientific Reports*, 6:20865, 2016.

[261] T. Okuda, K. Nakanishi, S. Miyasaka, and Y. Tokura. Large thermoelectric response of metallic perovskites: $Sr_{1-x}La_xTiO_3$ ($0<\sim x<\sim 0.1$). *Physical Review B*, 63:113104, 2001.

[262] L. Kouwenhoven and L. Glazman. Revival of the Kondo effect. *Physics World*, 14(1):33, 2001.

[263] M. Matusiak, E. M. Tunnicliffe, J. R. Cooper, Y. Matsushita, and I. R. Fisher. Evidence for a charge Kondo effect in $Pb_{1-x}Tl_xTe$ from measurements of thermoelectric power. *Physical Review B*, 80(22):220403, 2009.

[264] S. Das, P. C. Joshi, A. Rastogi, Z. Hossain, and R. C. Budhani. Magnetothermopower of δ-doped $LaTiO_3/SrTiO_3$ interfaces in the Kondo regime. *Physical Review B*, 90(7):075133, 2014.

[265] K. S. Kim and C. Pépin. Thermopower as a fingerprint of the Kondo breakdown quantum critical point. *Physical Review B*, 83(7):073104, 2011.

[266] L. P. Gor'kov. Phonon mechanism in the most dilute superconductor n-type $SrTiO_3$. *Proceedings of the National Academy of Sciences*, 113(17):4646–4651, 2016.

[267] Z. Huang, X. Renshaw Wang, Z. Q. Liu, W. M. Lü, S. W. Zeng, A. Annadi, W. L. Tan, X. P. Qiu, Y. L. Zhao, M. Salluzzo, J. M. D. Coey, T. Venkatesan, and Ariando. Conducting channel at the $LaAlO_3/SrTiO_3$ interface. *Physical Review B*, 88:161107, 2013.

[268] I. Pallecchi, F. Telesio, D. Li, A. Fête, S. Gariglio, J. M. Triscone, A. Filippetti, P. Delugas, V Fiorentini, and D. Marré. Giant oscillating thermopower at oxide interfaces. *Nature Communications*, 6:6678, 2015.

[269] Z. Wang, K. Barros, G. W. Chern, D. L. Maslov, and C. D. Batista. Resistivity minimum in highly frustrated itinerant magnets. *Physical Review Letters*, 117(20):206601, 2016.

[270] E. V. Sampathkumaran, K. Sengupta, S. Rayaprol, K. K. Iyer, Th. Doert, and J. P. F. Jemetio. Enhanced electrical resistivity before néel order in the metals $RCuAs_2$ (R=Sm, Gd, Tb, and Dy). *Physical Review Letters*, 91(3):036603, 2003.

[271] F. Bi, M. Huang, S. Ryu, H. Lee, C. W. Bark, C. B. Eom, P. Irvin, and J. Levy. Room-temperature electronically-controlled ferromagnetism at the $LaAlO_3/SrTiO_3$ interface. *Nature Communications*, 5:5019, 2014.

[272] T. McGuire and R. L. Potter. Anisotropic magnetoresistance in ferromagnetic 3d alloys. *IEEE Transactions on Magnetics*, 11(4):1018–1038, 1975.

[273] A. P. Malozemoff. Anisotropic magnetoresistance with cubic anisotropy and weak ferromagnetism: A new paradigm. *Physical Review B*, 34(3):1853, 1986.

[274] M. J. Jin, S. I. Kim, S. Y. Moon, D. Choe, J. Park, V. Modepalli, J. Jo, I. Oh, S. H. Baek, and J. W. Yoo. Study of rashba spin–orbit field at $LaAlO_3/SrTiO_3$ heterointerfaces. *Journal of Electronic Materials*, 48(3):1347–1352, 2019.

[275] K. Narayanapillai, K. Gopinadhan, X. Qiu, A. Annadi, Ariando, T. Venkatesan, and H. Yang. Current-driven spin orbit field in $LaAlO_3/SrTiO_3$ heterostructures. *Applied Physics Letters*, 105(16):162405, 2014.

[276] M.J. Jin, S. Y. Moon, J. Park, V. Modepalli, J. Jo, S. I. Kim, H. C. Koo, B. C. Min, H. W. Lee, S. H. Baek, et al. Nonlocal spin diffusion driven by giant spin hall effect at oxide heterointerfaces. *Nano Letters*, 17(1):36–43, 2016.

[277] A. Joshua, J. Ruhman, S. Pecker, E. Altman, and S. Ilani. Gate-tunable polarized phase of two-dimensional electrons at the $LaAlO_3/SrTiO_3$ interface. *Proceedings of the National Academy of Sciences*, 110(24):9633–9638, 2013.

[278] E Flekser, M Ben Shalom, M Kim, C Bell, Y Hikita, HY Hwang, and Y Dagan. Magnetotransport effects in polar versus non-polar srtio 3 based heterostructures. *Physical Review B*, 86(12):121104, 2012.

[279] P. W. Anderson. Absence of diffusion in certain random lattices. *Physical Review*, 109(5):1492, 1958.

[280] T. Kasuya. A theory of metallic ferro-and antiferromagnetism on Zener's model. *Progress of theoretical physics*, 16(1):45–57, 1956.

[281] K. Yosida. Magnetic properties of Cu-Mn alloys. *Physical Review*, 106(5):893, 1957.

[282] M. A. Ruderman and C. Kittel. Indirect exchange coupling of nuclear magnetic moments by conduction electrons. *Physical Review*, 96(1):99, 1954.

[283] S. Takada. Resistive anomalies at magnetic critical points. *Progress of Theoretical Physics*, 46(1):15–33, 1971.

[284] Michael E Fisher and JS Langer. Resistive anomalies at magnetic critical points. *Physical Review Letters*, 20(13):665, 1968.